Reduced Model for Flow Simulation in the Burner Region of Lime Shaft Kilns

Dissertation

zur Erlangung des akademischen Grades

Doktoringenieur

(Dr.-Ing.)

vorgelegt von

M.Sc. Zhiguo Xu
geb. am 04.02.1978
in Heze, Shandong, China

genehmigt durch die
Fakultät für Verfahrens- und Systemtechnik
der Otto-von-Guericke-Universität Magdeburg

Gutachter:
Prof. Dr.-Ing. E. Specht, Universität Magdeburg
Prof. Dr.-Ing. D. Thevenin, Universität Magdeburg

eingereicht am 01.03.2007

Promotionskolloquium am 19.10.2010

SCHRIFTLICHE ERKLÄRUNG

Ich erkläre hiermit, dass ich die vorliegende Arbeit ohne unzulässige Hilfe Dritter und ohne Benutzung anderer als der angegebenen Hilfsmittel angefertigt habe. Die aus fremden Quellen direkt oder indirekt übernommenen Gedanken sind als solche kenntilich gemacht.
Insbesondere habe ich nicht die Hilfe einer kommerziellen Promotionsberatung in Anspruch genommen. Dritte haben von mir weder unmittelbar noch mittelbar geldwerte Leistungen füe Arbeiten erhlten, die im Zusammenhang mit dem Inhalt der vorgelegten Dissertation stehen.
Die Arbeit wurde bisher weder im Inland noch im Ausland in gleicher oder ähnlicher Form als Dissertation eingereicht und ist als Ganzes auch noch nicht veröffentlicht.

Zhiguo Xu
Magdeburg, 19 October 2010

If three of us are walking together, at least one of the other two is good enough to be my teacher.

-Confucius (551 BC - 479 BC)

Acknowledgments

First and foremost, I would like to express my deep and sincere gratitude to my advisor Pro. Dr.-Ing. Eckehard Specht, for his constant advice, encouragement and financial support. His knowledge, experience and patience have benefited me immensely.

I am deeply grateful to my second advisor Pro. Dr.-Ing. Dominique Thevenin for his elaborated review of my thesis and constructive comments.

Further acknowledgment goes to Jun.-Prof. Dr.-Ing. Ulrike Krewer who accepted to review my thesis and took over the chair in examination committee.

I wish to thank our lovely and united research group. I have learned a great deal from them and really enjoyed the time we shared together. Special thanks to Dr. Woche, Dr. Ashok Nallathambi, Umair Alam, Ping Meng, Haido, Nadine Lorenz, Fabian Harz, and of course, our sweet and warm-hearted secretary Christin Hasemann, for their friendship, inspiring discussions and help in the past three years.

I also wish to thank the master students Esref Bastug and Maryam Sadat Dadkhah for their enormous help during the writing of this dissertation.

My deepest gratitude goes to my family, including my fiancee Zhixia Zhu, for their unflagging love and support throughout my life; this dissertation is simply impossible without them.

Last but not least, thanks be to my special friends Juergen Loztin, Heiko Menzel, and Dirk Schnieke. They made my life in Magdeburg a wonderful experience.

Abstract

The knowledge of temperature distribution and radial gas mixing plays a very important role in design of lime shaft kilns, yet is poorly understood. This is due to the geometric complexity and the movement of the lumpy processed material which make it impossible to measure the main parameters, such as temperature and gas components, as well as flow velocity. As one of the critical "enabling technologies", computational fluid dynamics (CFD) is used to study the different aspects of the internal phenomena of the kilns by means of flow visualization. Geometrical models are initially developed based on a normal lime shaft kiln. To model such a complicated system, simplifications are inevitable. For instance, the arbitrarily shaped and stacked processed material granules are simplified to be uniform spheres and packed in regular structure. Regarding the main body, the feeding and the discharging ports including the cooling air distributor are excluded in this stage.

As a rule of thumb, investigation is firstly carried out in two dimensions thanks to the great advantage in the computational time. Considering the serious deficits caused by the geometric limitations, however, the main purpose of the 2-D modeling is to obtain some general information about the jet flow in packed bed and thereby help develop the 3-D geometry. The results show that the flow structure in the jet expanding zone is independent on the height of the bed. This means that modeling of the reaction zone of shaft kiln is assumed to be sufficient to optimize the firing system. It has also been proved that the jet flow pattern is slightly influenced by the heat transfer between the solid and gas phases. In other words, heat transfer between phases can be ignored as long as the flow structures are the interest of study. Such simplifications, in a certain degree, make the 3-D modeling of an industrial shaft kiln economically and technically possible based on the present computer power.

The 3-D geometric model in this work is a 30^o segment with a bed height of about 0.8 m. Simulations based on this geometry are performed to investigate the dominant factors influencing the radial temperature distribution. The in-kiln flow structures are distinctly visualized by images of temperature contours and pathlines etc. It appears that the increase in the lance depth may prevent the refractory wall being overheated but have slight effect on the ratio of the cold and hot area, which is in agreement with 2-D simulations. Mixing between the combustion gas and the cooling air can be improved by reducing the burner diameter or by preheating the combustion air, as both of which accelerate the jet velocity and provide energy aspirating the cooling air. In the simulation of furnace with diffusion burner,

longer flame and deeper jet penetration illustrate the preference of the shaft kilns in the lime industry. In addition, simulations are also performed with defining the bed as porous media. As expected, the radial penetration of the combustion gas is underestimated relatively. This is mostly due to the over-prediction of the momentum loss caused by the inertial terms in the model. Considering its great advantages of simple geometry and short computational time, however, further study in porous medium modeling is expected.

As this study demonstrates, simulations upon the scalable segment geometric model are capable of providing the main flow features in the reaction zone of lime shaft kilns, which are nearly impossible to study in experimental setups. With further development and evaluation, CFD approach is expected to be one of the effective methods that could substantially reduce physical testing in the design of lime shaft kilns.

Zusammenfassung

Die Kenntnisse über die Temperaturverteilung und die radiale Gasmischung haben eine groß e Bedeutung bei der Gestaltung von Kalkschachtöfen. Derzeit sind diese aber wenig verstanden. Auf Grund der geometrischen Komplexität und der Bewegung des klumpigen Materials, ist es unmöglich, die wichtigsten Parameter wie Temperatur, die Gaskomponenten sowie die Strömungsgeschwindigkeit zu messen. Um die verschiedenen Aspekte der Phänomene im Ofen durch die Sichtbarmachung von Strömungen zu untersuchen, wurde als eine der entscheidenden "Grundlagentechnologien", die Computational Fluid Dynamics (CFD) verwendet. Die geometrischen Modelle wurden zunächst auf der Grundlage eines normalen Kalkschachtofens entwickelt. Zur Modellierung eines so komplizierten Systems, sind Vereinfachungen nötig. Beispielsweise wurden die unregelmäß ig geformten und gepackten Verarbeitungsgranulate vereinfacht als einheitliche Kugeln in regelmäß iger Struktur verpackt, angenommen. In Bezug auf den Hauptteil des Schachtofens wurden die Zu- und Abfuhranschlüsse sowie die Kühlluftverteilung zunächst einmal vernachlässigt.

Erwartungsgemäß, wurden vorab 2-D-Simulationen durchgeführt. Ein groß er Vorteil liegt in der Rechenzeit. Unter Beachtung der erheblichen Defizite, auf Grund der geometrischen Einschrïkungen, war dennoch der Hauptgegenstand der 2-D-Modellierung, einige allgemeine Informationen über die Jet-Strömung im Packbett zu erhalten, gegeben und somit konnte eine 3-D-Modellierung entwickelt werden. Die Ergebnisse zeigten, dass die Strömungsstruktur in der Jet-Erweiterungszone von der Höhe des gesamten Bettes unabhängig ist. Dies bedeutet, dass die Modellierung der Reaktionszone des Schachtofens eine ausreichende Optimierung des Brennersystems annimmt. Es wurde auch bewiesen, dass die Jet-Strömung leicht durch den Wärmeübergang zwischen der festen und gasförmigen Phase beeinflusst wird. Mit anderen Worten, die feste Phase kann vernachlässigt werden, wenn die Strömungsstrukturen von Interesse sind. Solche Vereinfachungen machen die 3-D-Modellierung eines industriellen Schachtofens, auf der Grundlage der vorliegenden Computerleistung, wirtschaftlich und technisch möglich.

Das 3-D geometrische Modell in dieser Arbeit ist ein 30 Abschnitt Modell, bestehend aus 9 Schichten mit Partikel. Simulationen auf Grundlage dieser Geometrie wurden durchgeführt, um die dominierenden Faktoren, die die radiale Temperaturverteilung beeinflussen, zu untersuchen. Die Strömungsstrukturen im Schachtofen wurden durch Bilder der Temperaturkonturen und Stromlinien usw. visualisiert. Es wurde gezeigt, dass eine Erhöhung der Brennerlanzentiefe eine

Überhitzung der Ofenwand verhindern kann, was aber geringe Auswirkungen auf die Verteilung der kalten und warmen Bereiche hat, die im Einvernehmen mit den 2-D-Simulationen stehen. Die Mischung zwischen dem Brenngas und der Kühlluft kann durch die Verringerung des Brennerdurchmessers oder durch eine Vorwärmung der Verbrennungsluft verbessert werden. Beides beschleunigt die Jetgeschwindigkeit und liefert Energie zur Ansaugung der Kühlluft. Bei der Simulation von Brennöfen mit Diffusionsbrenner zeigten längere Flammen und tiefere Strahleindringungen die Bevorzugung der Schachtöfen in der Kalkindustrie. Des Weiteren werden Simulationen durchgeführt, in denen das Bett als poröser Körper definiert ist. Wie erwartet, ist die radiale Durchdringung des Verbrennungsgases, drastisch unterschätzt. Dies ist hauptsächlich bedingt durch die Überschätzung des Impulsverlustes, verursacht durch den Trägheitsterm im Modell. Mit dem Ergebnis, dass das Modell für poröse Materialien nicht geeignet ist für Festbetten mit großen Partikeln, z. B. rund 100 mm Durchmesser oder größer, besonders bei der Durchströmung mit hohen Geschwindigkeiten.

Wie diese Studie zeigt, sind Simulationen mit dem skalierbaren Abschnitts Modell in der Lage, die wichtigsten Strömungskenndaten in der Reaktionszone der Kalkschachtöfen zu bestimmen, was mit experimentellen Untersuchungen nahezu unmöglich ist. Mit einer weiteren Entwicklung und Auswertung könnte der CFD Ansatz eine der effektivsten Methoden werden, um die physikalischen Tests bei der Gestaltung von Kalkschachtöfen wesentlich zu reduzieren.

Contents

SCHRIFTLICHE ERKLÄRUNG **i**

Acknowledgments **iii**

Abstract **v**

Zusammenfassung **vii**

List of Tables **xiv**

List of Figures **xix**

Abbreviations **xxi**

1 Introduction **1**

1.1 Limestone, lime and dolomite 1

1.1.1 Limestone and dolomite 1

1.1.2 Lime and lime production 2

1.2 Lime production equipment 4

1.2.1 Early kilns 5

1.2.2 Modern kilns 6

1.2.3 The normal shaft kiln 7

1.3 Common problems in normal shaft kilns 10

1.3.1 High temperature of the combustion zone 10

1.3.2 Non-uniformity of gas distribution 11

1.4 Modeling aided design 13

1.4.1 Dynamic process simulations 13

1.4.2 CFD approach 14
1.5 Objectives 14
1.6 Summary 14

2 Computational Fluid Dynamics in Packed Bed Reactors 17
2.1 Computational Fluid Dynamics 17
2.1.1 Applications of CFD 17
2.1.2 Computation of fluid motions 18
2.1.3 Discretization methods 24
2.1.4 Grid generation and near-wall treatment 25
2.1.5 The CFD process 30
2.2 CFD modeling of packed beds 31
2.2.1 CFD models: “porous medium” vs. “discrete particle” . . . 31
2.2.2 Achievements and challenges 32
2.3 Summary 36

3 Geometric Model Development 37
3.1 Geometry and process simplification 37
3.2 2-D Geometric model development 39
3.2.1 Particle arrangement 39
3.2.2 Burner 40
3.2.3 Bed height 42
3.2.4 The basic 2-D geometric model 43
3.3 3-D Geometric model development 43
3.3.1 Particle arrangement 44
3.3.2 The wall segment strategy 45
3.3.3 The basic 3-D geometric model 45
3.4 Summary 47

4 Grid Design and Grid Convergence Studies 49
4.1 Discretization error and its estimation 49
4.1.1 Discretization error 49
4.1.2 Grid convergence index (GCI) 50

4.1.3 The key variables 52
4.2 Gridding strategy and model reduction 54
4.2.1 Gridding strategy 54
4.2.2 Model reduction 55
4.3 Grid convergence study of 2-D model 56
4.3.1 *Unit model* description 56
4.3.2 material properties and solution control 57
4.3.3 Grids 57
4.3.4 Computation and analysis 59
4.4 Grid convergence study of 3-D model 63
4.4.1 *Unit model* description 63
4.4.2 Grids 65
4.4.3 Material properties and solution control 65
4.4.4 Computation and analysis 67
4.5 Summary 71

5 2-D Flow Simulations 73
5.1 Simulations of *cold flow* 73
5.1.1 Description of geometries and grid in near jet region 73
5.1.2 Definition of the simulation model and materials 74
5.1.3 Effect of bed height on jet behavior 76
5.1.4 Effect of packing near the side-nozzle on jet behavior 81
5.1.5 Effect of jet velocity on jet penetration 87
5.2 Simulations of reacting flow 91
5.2.1 Description of the geometry and computational mesh 92
5.2.2 Definition of the simulation model and materials 93
5.2.3 Special procedure for combustion simulation 93
5.2.4 Effect of jet velocity on radial gas mixing 94
5.2.5 Effect of heat transfer and transient state 100
5.3 Case study 104
5.3.1 Description of the kiln and model of the burner 104
5.3.2 Basic calculations 105

5.3.3 Description of the cases 106
5.3.4 Model definition and boundary conditions 107
5.3.5 Results and discussions 108
5.4 Summary 113

6 3-D flow Simulations of Shaft Kilns **115**
6.1 Description of the geometry and the grid 115
6.2 Definition of the simulation models and materials 120
6.3 Simulations and results 120
6.3.1 Influence of lance depth 120
6.3.2 Influence of burner diameter 125
6.3.3 Influence of preheating combustion air 128
6.3.4 Influence of burner arrangements 130
6.4 Modeling the kilns with diffusion burner 132
6.4.1 Geometry and mesh of the diffusion burner 133
6.4.2 Definition of the models and solution controls 134
6.4.3 Boundary conditions 134
6.4.4 Simulation and results 134
6.5 Porous medium model 137
6.5.1 Defining the viscous and inertial resistance 137
6.5.2 Model definition and Boundary conditions 139
6.5.3 Geometry and computational mesh 140
6.5.4 Simulation results 141
6.6 Summary and Conclusions 144
6.7 Recommendations 144

Bibliography **144**

List of Publications **151**

List of Tables

1.1 Summary of typical characteristics of common kilns 6
1.2 Fuels used in lime-burning [EuLA] 10

4.1 The properties of air and the operating conditions 57
4.2 Under-relaxation factors for the computing variables 57
4.3 Estimation of the wall distance to yield the first grid 58
4.4 The grids used for grid convergence study (2-D) 58
4.5 Computational results upon the three levels of grid 60
4.6 Calculation results based on the GCI method 63
4.7 Comparison between the upwind schemes 63
4.8 The grids used for grid convergence study (3-D) 65
4.9 Under-relaxation factors for the computing variables 67
4.10 Computational results upon the three levels of grid 67
4.11 Comparison of pressure drop 70

5.1 Under-relaxation factors for the computing variables 76
5.2 Properties of the gases 76
5.3 Boundary conditions 77
5.4 Inlet boundary conditions of the nozzle 88
5.5 Inlet/outlet boundary conditions 94
5.6 Composition, air demand and net calorific value of nature gas L . . 105
5.7 Calculations based on 26.3 t/day/m^2 lime production 106
5.8 Depth of the burner lance and its width (1-level burner system) . . 107
5.9 Depth of the burner lance and its width (2-level burner system) . . 107
5.10 Under-relaxation factors for the computing variables 108

5.11 Boundary conditions at $Inlet_{fm}$ for each case 108
5.12 Boundary conditions at $Inlet_{ca}$ and *Outlet* for all cases 108

6.1 Under-relaxation factors for the computing variables 120
6.2 Inlet and outlet boundary conditions 121
6.3 Inlet and outlet boundary conditions for Case III 125
6.4 Inlet and outlet boundary conditions for Case IV 128
6.5 Inlet and outlet boundary conditions for Case V 130
6.6 Inlet and outlet boundary conditions 134
6.7 Values for the viscous and inertial resistance coefficients 139
6.8 Inlet and outlet boundary conditions 140

List of Figures

1.1 The diagram of lime cycle [1] 4
1.2 Cross section of typical early kiln 5
1.3 A preserved lime kiln in Burgess Park, London 5
1.4 The structure of the normal shaft kiln 7
1.5 The top view of the burners in the RCE shaft kiln 8
1.6 The typical burner beams applied to the FERCALX shaft kiln . . . 8
1.7 Schematic of a premixed burner [2] 9
1.8 Schematic of a diffusion burner [3] 9
1.9 Temperature profile in a counter flow kiln [4] 11
1.10 The radial temperature distribution in burning zone 12
1.11 The structure of a RCE lime kiln 12

2.1 Some common sub-domains 25
2.2 An example of a structured multiblock grid 26
2.3 An example of an unstructured grid 27
2.4 An example of a hybrid grid (CRAFT Tech) 27
2.5 Subdivisions of the near-wall region [5] 28
2.6 Near-wall treatments in FLUENT [5] 29
2.7 Side and close-up isometric view of a geometric model 32
2.8 A full bed simulation geometry with graded surface mesh, N=4 . . 33
2.9 Sphere arrangement within a square vessel 33
2.10 3-D view of a wall segment geometry with flow path lines 34
2.11 3-D view of a wall segment geometry with cylindrical particles [6] . 34
2.12 Geometric model with gaps between particles 35
2.13 Geometric model with small overlap between particles 35

3.1 The schematic of a RCE lime shaft kiln 38
3.2 Flow through a tube bank 39
3.3 Arrangement of tubes in a bank 39
3.4 The arrangement in 2-D geometric model 40
3.5 Schematic of the diffusion burner geometry in 3-D 41
3.6 2-D geometry of the burner 41
3.7 2-D geometry schematic of the shaft kiln with horizontal burner . . 43
3.8 A hexa-based sphere cluster 44
3.9 A octa-based sphere cluster 44
3.10 A tetra-based sphere cluster 45
3.11 Schematic of a shaft kiln with 12 horizontal diffusion burners 46
3.12 The 30^o WS 3-D Geometry 46

4.1 The friction and correction factors for staggered tube banks [7] . . . 53
4.2 Computational domains and sub-domains for gridding 55
4.3 A schematic of the tube-bank geometric model 56
4.4 The unit model and the boundary definition 56
4.5 The finest mesh (Grid 1) 58
4.6 The medium mesh (Grid 2) 58
4.7 The finest mesh (Grid 3) 59
4.8 y^+ plots in each case 59
4.9 The velocity profiles along Line 1 on three sets of grid 60
4.10 The velocity contours predicted on Grid 1 61
4.11 The velocity contours predicted on Grid 2 61
4.12 The velocity contours predicted on Grid 3 62
4.13 The velocity vector plots on Grid 3 and Grid 1 62
4.14 A 4-layer scheme of the 3-D packing: (a) z view, and (b) y view. . . 64
4.15 Schematic of the 3-D unit model 64
4.16 The coarsest mesh (Grid 1) 66
4.17 The medium mesh (Grid 4) 66
4.18 The finest mesh (Grid 8) 66
4.19 Pressure drop as a function of the grid density 68

4.20 Velocity vector plot of the simulation on the Grid 1 68
4.21 Velocity vector map of the simulation on the Grid 2 69
4.22 Velocity vector plot of the simulation on the Grid 3 69
4.23 Comparison of CFD and Brauer′s equation 70
4.24 Comparison of grid quality 70
4.25 Graded mesh design on the surface of particles 71

5.1 Geometry of packed be with side-nozzle 74
5.2 Grid in the near jet region without size function 75
5.3 Grid in the near jet region with the *Meshed size function* 75
5.4 Comparison of the mass fraction contours of CO_2 78
5.5 Comparison of the mass fraction of CO_2 along the cross-section . . 79
5.6 Comparison of the mass fraction contours of CO_2(tube nozzle) . . . 79
5.7 Mass fraction of CO_2 along the cross-section at $x = 0.65$ 80
5.8 Distribution of CO_2 along different cross-sections 80
5.9 The structure of packing near the side-nozzle (Model A) 81
5.10 The structure of packing near the side-nozzle (Model B) 82
5.11 Comparison of CO_2 contours ($v_{CO_2} = 4\ m/s$) 83
5.12 Comparison of mass fraction of CO_2 ($v_{CO_2} = 4\ m/s$) 83
5.13 Comparison of CO_2 contours ($v_{CO_2} = 10\ m/s$) 84
5.14 Comparison of mass fraction of CO_2 ($v_{CO_2} = 10\ m/s$) 84
5.15 Comparison of CO_2 contours ($v_{CO_2} = 22\ m/s$) 85
5.16 Comparison of mass fraction of CO_2 ($v_{CO_2} = 22\ m/s$) 85
5.17 Comparison of pathlines of the main stream ($v_{CO_2} = 22\ m/s$) . . . 86
5.18 Comparison of CO_2 contours (Horizontal jet) 89
5.19 Comparison of CO_2 contours (Vertical jet) 89
5.20 Comparison of the pathlines of the main stream ($\dot{r} = 1.6$) 90
5.21 Close views of velocity vectors around the jets ($\dot{r} = 1.6$) 91
5.22 Schematics of a normal nozzle 91
5.23 2-D geometry for simulations of reacting flow 92
5.24 2-D geometries and computational meshes 93
5.25 Temperature contours on each geometry (unreacting flow) 95

5.26 Temperature contours on each geometry (reacting flow simulation) . 95
5.27 Comparison of the main stream pathlines in reacting flow 96
5.28 Close view of the velocity vectors near the burner (Cold flow) . . . 97
5.29 Close view of the velocity vectors near the burner (Combustion) . . 97
5.30 Close view of the velocity vectors (Case I and Case II) 98
5.31 Close view of the mass fraction contours of CH_4 99
5.32 Concentration of CH_4 along Line 1 99
5.33 Geometry and mesh with solid domain 100
5.34 Temperature contours at 1 min and 5 min 102
5.35 Temperature contours at 30 min and steady state 102
5.36 Velocity distributions along Line 1 with time 103
5.37 Comparison of temperature contours 103
5.38 Geometry of the burner lance 104
5.39 2-D geometries with 1/2 burner lances 106
5.40 Temperature contours (Case I, lance depth = 0.1 m) 109
5.41 Temperature contours (Case II, lance depth = 0.32 m) 109
5.42 Temperature contours (Case III, lance depth = 0.5 m) 110
5.43 Comparison of temperature profile along $x = 1.15m$ 110
5.44 Temperature contours for Case IV, $\dot{V}_{fm1}/\dot{V}_{fm2} = 5.5\ m$ 111
5.45 Temperature contours for Case V, $\dot{V}_{fm1}/\dot{V}_{fm2} = 4.0\ m$ 112
5.46 Temperature contours for Case VI, $\dot{V}_{fm1}/\dot{V}_{fm2} = 3.0\ m$ 112
5.47 Comparison of temperature profile along $x = 1.15m$ 113

6.1 Isometric view of the 3-D geometric model 116
6.2 Top view of burner lances 116
6.3 Views of the burner in the case of one-level arrangement 117
6.4 view of the burner in the case of two-level arrangement 118
6.5 Prism grid for inlet and outlet domain 119
6.6 Unstructured grid pattern on the face of particles 119
6.7 Temperature contours of Case I 122
6.8 Temperature contours of Case II 122
6.9 Top views of the temperature contours with different lance depths . 123

6.10 Comparison of the mean temperature profile between Case I and II 124
6.11 Pathlines released from the inlet of the cooling air (Case I) 124
6.12 Temperature contours of Case III 126
6.13 Pathlines released from the inlet of the cooling air (Case III) 127
6.14 Temperature contours on the surface of particles of Case IV 129
6.15 Temperature contours on the surface of particles of Case V 131
6.16 Comparison of the mean temperature profiles 132
6.17 The geometry and the dimensions of the diffusion burner 133
6.18 The hybrid mesh of the diffusion burner 133
6.19 Temperature contours in the case of diffusion burner used 135
6.20 Top view of the temperature contours 135
6.21 Pathlines released from the inlet of combustion air 136
6.22 Pathlines released from the inlet of cooling air 136
6.23 Geometry and computational mesh for the simulation 140
6.24 Comparison of the temperature contours by using PMM and DPM . 142
6.25 Comparison of the pathlines between PMM and DPM 143
6.26 Comparison of the x-velocity contours between PMM and DPM . . 143

Abbreviations

Variables

A	area, m^2
C_2	inertial resistance coefficient, m^{-1}
d	diameter, mm
D	diameter of packed bed, mm
D_h	hydraulic diameter, mm
D_p	affective average particle diameter, mm
f	friction factor
H	height of packed bed, m
$h(D_p)$	density function for the distribution of diameters D_p
h_u	net calorific value, MJ/m^3
I	turbulence intensity, %
J	momentum flux ratio
K_L	loss factor
K'_L	adjusted loss factor
L	unit length, m
$\tilde{L}$	air demand, m^3_{air}/m^3_{fuel}
$\dot{m}$	mass flow rate, kg/s
n	number of burner
N	number of tube rows
p	order of accuracy
P	pressure, Pa
Q	energy consumption per kg lime production, MJ
r	distance from the tip of the burner to the centerline of the kiln, m
$\dot{r}$	volumetric flow ratio
R	radius of shaft kilns, m
S	center-to-center distance of bank tubes, mm
T	temperature, K
U	superficial velocity, m/s
v	velocity, m/s
$\dot{V}$	volumetric flow rate, m^3/s
α	viscous resistance coefficient, m^{-2}
χ	correction factor
ϵ	turbulence dissipation rate
κ	turbulence kinetic energy
λ	air excess number

ϕ	relative error
μ	dynamic viscosity, $kg/m/s$
ρ	density, kg/m^3
φ	void fraction
γ	grid refinement ratio
Ω	mass flow ratio

Subscripts

a	air
b	burner
ca	cooling air
f	fuel
fa	combustion air
fm	mixture of fuel and combution air
j	jet
L	longitudinal
m	main stream
p	particle
T	transverse

Chapter 1

Introduction

Lining fire pits and rocks, ancient man discovered that the heat turned limestone into a new and different material. The rocks, now soft and white, reacted with water to give off heat. The new material is calcium oxide (CaO), also called lime, quicklime, or caustic lime. As one of the man's oldest chemicals, lime, which was being used for paving roads by the ancient Romans, is now being widely used in many fields and applications. The building material of ancient world has become to be "the most versatile material" of our time.

Production of lime is a simple chemical process, calciation or burning of limestone and dolomite in lime kilns. However, the process is characterized by heavy energy consumption as well. Due to the general trend of market globalization, environmental actions, higher client expectations for quality, and increased profit revenue for manufacturing companies, optimizing the efficiency in its production is going to be considerably important. In this chapter, an introduction to lime and lime production is presented, followed by the problems that this thesis focuses to tackle.

The term lime as used throughout this thesis refers primarily to "high calcium lime" derived from calcined limestone, or "dolomitic lime" from burnt dolomite where necessary.

1.1 Limestone, lime and dolomite

1.1.1 Limestone and dolomite

Limestone is the most important and abundant sedimentary rock and is formed by the compaction of the remains of coral animals and plants on the bottoms of oceans around the world. It can be a soft white substance (chalk) through to a very hard substance (marble). Limestone is composed of the mineral calcite ($CaCO_3$) and/or the mineral dolomite ($CaCO_3$ and $MgCO_3$) along with small amounts of other minerals. There are three distinct types of limestone which are defined by their magnesium carbonate ($MgCO_3$) concentrations:

(1) Dolomitic limestone consists of 35 to 46% magnesium carbonate;

(2) Magnesian limestone consists of 5 to 35% magnesium carbonate;

(3) High calcium limestone contains less than 5% magnesium carbonate.

Limestone is quarried or mined then crushed and screened to serve a wide variety of applications including:

a. pH adjustment (Ag-Lime, water treatment);

b. Formulated product filler (masonry cements, ready mix concrete, asphalt, and joint compounds);

c. Flue gas desulfurization;

d. Production of stone blocks; and

e. Lime production.

1.1.2 Lime and lime production

As being mentioned, lime is produced by the thermal decomposition of limestone or dolomite. Its quality depends on many factors, including physical properties, degree of sintering, and chemical composition. As the most readily available and cost effective alkaline chemical, lime plays an essential part in a wide variety of industrial processes. The most important fields of application for lime and dolomitic lime are:

- Agriculture: Lime increases fertilizer efficiency. Liming an acid soil raises the soil pH, the levels of calcium and magnesium, accelerates micro-biological activity and increases the rate of release from the soil of organic matter and nutrient elements.

- Aluminum Industry: Lime helps remove silica from bauxite ore during the manufacture of alumina.

- Agriculture: Lime increases fertilizer efficiency. Liming an acid soil raises the soil pH, the levels of calcium and magnesium, accelerates micro-biological activity and increases the rate of release from the soil of organic matter and nutrient elements.

- Aluminum Industry: Lime helps remove silica from bauxite ore during the manufacture of alumina.

- Building industry: Lime is used in the manufacture of lime silica bricks, insulation and building board materials. It is used in the mortar to lay bricks and the render of walls. Lime is also added to concrete and plaster to improve their performance.

- Food industry: Lime is reacted with crude sugar juice for the production of both cane and beet sugars. Lime is an ingredient in baking soda and helps keep fruit and vegetables fresh.

- Industrial Waste Water Treatment: Lime neutralizes acid wastes generated in industry thereby impeding corrosion and protecting the natural environment. Lime also removes silica, manganese, fluorides, iron and other impurities from water.

- Metals Extraction Industries: Lime serves as a "flotation" vehicle in the recovery of copper, mercury, zinc, nickel, lead, gold and silver.

- Paper manufacture: Pulp and paper manufacturers use lime to recover caustic soda during the conversion of wood chips to pulp. Lime bleaches the pulp and also dissolves non-cellulose components of straw and disintegrates it's fibers during the manufacture of strawboard and pasteboard.

- Pollution control: Lime is used to absorb sulphur dioxide from exhaust gases in smelters and power generation plants.

- Road construction: Lime converts unstable clay sub-grades by breaking down clod formations. It creates soil that will not swell or shrink. It can provide a cementing action that stabilizes soil into a steadfast layer impervious to water penetration.

- Sewage treatment: Lime reduces pollution by removing organic matter, phosphates and nitrogen from waste water. It prevents over vegetation in streams and lakes, controls odors from waste ponds and precipitates heavy metals.

- Soil stabilization: Lime can be used to stabilize soil in wet, boggy conditions to allow earthworks to continue.

- Steel Industry: Lime is used for removal of phosphorous, sulphur and silicon impurities and therefore lowing the melting temperature of slag. Lime lubricates steel rods as they are drawn through dies to form wire. As a whitewash coating, lime prevents ingots sticking to the molds during pig iron casting. A bath of lime neutralizes traces of pickling acid adhering to steel products.

- Tanneries: Lime removes hair and plump hides preparatory to leather tanning.

- Water Treatment: Lime treats potable and industrial water supplies, including drinking water for cities and process water used in industry. It softens water by removing bicarbonate hardness and disinfects against bacteria.

In many countries, the largest use is for the production of iron and steel, followed by building and construction, environmental protection, and the chemical industry [8].

Production of lime is carried out in lime kilns. When heated the carbonate, the following chemical reactions take place with limestone and dolomite respectively:

$$CaCO_3 + \text{approx. } 3180 \text{ kJ}(760\text{kcal}) = CaO + CO_2$$
$$CaMg(CO_3)_2 + \text{approx. } 3050\text{kJ}(725\text{kcal}) = CaO + MgO + 2CO_2$$

High quality limestone contains 97 to 99% $CaCO_3$. High qualitiy dolomite contains 40 to 43% $MgCO_3$ and 57 to 60% $CaCO_3$. It requires approximately 1.75 tons of limestone to produce one ton of lime and approximately 2 tons of dolomite to produce one ton of dolomitic lime.

It's interesting to mention that,after processing, lime derived from limestone have the unique ability to return to their original chemical form. In the Fig. 1.1, carbon dioxide in the atmosphere or from industrial combustion processes react with hydrated lime to convert it back to limestone. This cycle of sustainability is called the lime cycle. Global production of lime is estimated to be approximately

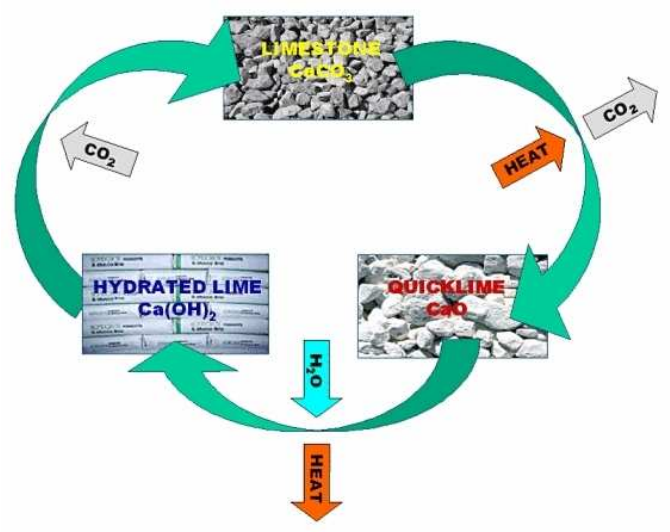

Figure 1.1: The diagram of lime cycle [1]

300 million tons per year, whereof the sales-relevant portion amounts to 120 million tons per year. In industrialized countries the yearly per capita consumption of lime products amounts to ∼ 80 kg. Detailed worldwide production of lime was reviewed by A. Bes [9]. According to the information collected from 1994 to 2003, the United States and China, each accounting for about 20 million tons, or ∼18% of world output, were followed by Germany and Japan with about 7% of world output.

1.2 Lime production equipment

Lime is one of man's oldest chemicals. There is evidence of the widespread use of quicklime and hydrated lime for building by many civilizations by about 1000 B.C., including the Greeks, Egyptians, Romans, Incas, Mayas, Chinese, and Mogul Indians. As its production equipment, lime kilns must have experienced a long-term evolution.

1.2.1 Early kilns

The common feature of early kilns was an egg-cup shaped burning chamber, with an air inlet at the base (the “eye”), constructed of brick, as shown in Fig. 1.2and Fig. 1.3. Limestone was crushed (often by hand) to fairly uniform 20-60 mm (1 to 2.5 in) lumps. Successive dome-shaped layers of wood/coal and limestone were built up in the kiln on grate bars across the eye. When loading was complete, the kiln was kindled at the bottom, and the fire gradually spread upwards through the charge for a few days. When burnt through, the lime was cooled and raked out by hand through the base.

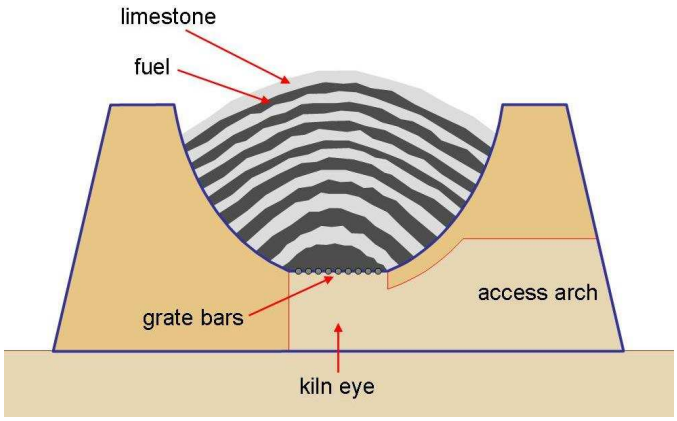

Figure 1.2: Cross section of typical early kiln [10]

Figure 1.3: A preserved lime kiln in Burgess Park, London [10]

Only lump stone could be used, because the charge needed to ”breathe” during firing. This also limited the size of kilns and explains why kilns were all much the same size. Above a certain diameter, the half-burned charge would be likely to collapse under its own weight, extinguishing the fire. So kilns always made 25-30 tonnes of lime in a batch. Typically the kiln took a day to load, three days to fire, two days to cool and a day to unload, so a one-week turnaround was normal [10]. The degree of burning was controlled by trial and error from batch to batch by

varying the amount of fuel used. Because there were large temperature differences between the center of the charge and the material close to the wall, the product often contained substantial amounts of both over- and under-burned lumps, and the thermal efficiencies were very low.

1.2.2 Modern kilns

A large variety of techniques and kiln designs have been used over the centuries and around the world. The concept of the lime kiln has been modernized in a number of designs, however, two types of kilns are primarily used in today's lime industry:

- Rotary kilns, and
- Shaft kilns.

The characteristics of few of them are summarized in Table1.1 [9, 11].

Table 1.1: Summary of typical characteristics of common kilns

Kiln type	Fuels	Output range [T/d]	Feed size [mm]	Energy usage MJ/kg lime
Shaft:				
Mixed-feed	S	60-200	20-200	4.0-6.0
Double-inclined	G,L,S	10-160	20-100	4.0
Multi-chamber	G,L,S	40-225	20-150	4.2
Annular	G,L,S	80-600	10-250	4.0-4.6
PFR-standard	G,L,S	100-600	25-200	3.6-4.2
PFR-fine lime	G,S	100-300	10-30	3.6-4.2
Rotary:				
Long	G,L,S	160-1500	dust-60	4.2-5.2
preheater	G,L,S	150-1500	0-60	-

G-gaseous, L-liquid, S-solid

Rotary kilns, with or without pre-heater, usually process grain size between 6 and 50 mm. The heat balance of this type of kilns is characterized by rather high losses with the off-gases and through the kiln shell. Therefore, heat usages for rotary kilns are generally much higher than those of shaft kilns. However, many lime producers have found that rotary kilns complement shaft kilns, because they use a smaller feedstone and produce quicklimes with different characteristics, which meet the requirements of certain customers.

For shaft kilns, two main types exist. The single shaft counter flow heating kiln and the multiple shaft parallel flow heating kiln, i.e. the parallel flow regenerative (PFR) lime shaft kiln. To improve the heat efficiency and produce high reactive lime, several designs has been developed for the single-shaft kilns [9, 8]. In this work, however, all simulations will be carried out based on the structure of the normal shaft kilns, which is described below.

1.2.3 The normal shaft kiln

•The basic process description

The normal shaft kilns, as shown in Fig. 1.4, are basically packed bed reactors and work on a very simple principle. The raw material is charged at the top of the kiln and the product is withdrawn from the bottom, causing the material to move slowly downwards through the kiln. Heat to calcine the material is introduced roughly in the middle of the kiln by radially arranged firing system, and therefore, any material above is preheated by rising hot exhaust gases and any below is cooled by incoming air from the bottom. In this way, the kiln is regarded as incorporating three operating sections: the preheating, the calcination (burning) and the cooling zone.

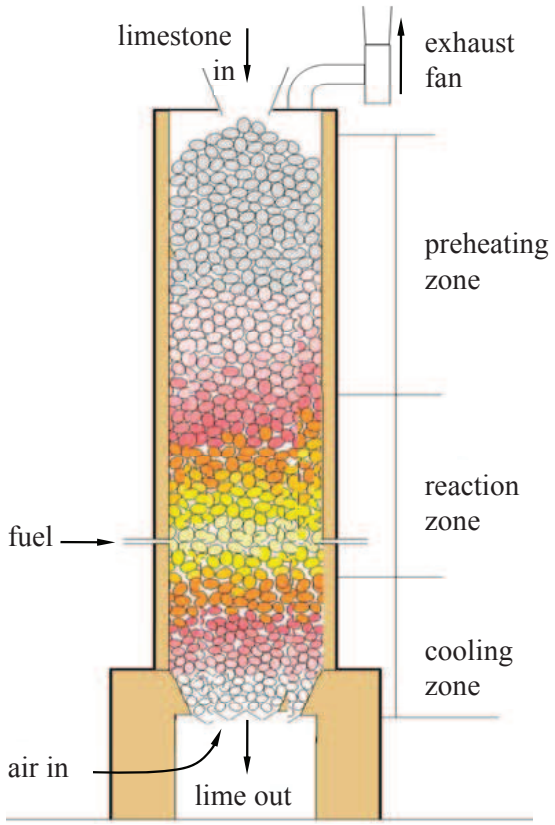

Figure 1.4: The structure of the normal shaft kiln

Dissociation of $CaCO_3$ occurs in the calcination zone in a temperature range between 870 and 1250 ^oC. In the cooling zone the main part of the sensible heat of

lime is transferred to the cooling airflow, which enters the calcination zone at the temperature of about 700-800 ^oC to react with the fuel. The sensible heat of gases leaving the calcination zone is transferred to the limestone in the preheating zone. The temperature of limestone at the bottom of the preheating zone reaches the temperature of calcination. The off-gas from the preheating zone has a temperature of about 150-300 ^oC. It is not possible to utilize the off-gas heat content completely, since the heat capacity of the gases in the preheating zone is higher than the heat capacity of the charge material.

•Firing system and fuel types

Of all the parts of a furnace, the firing system is the most essential. In a normal shaft kiln, the firing system generally consists of many burner lances or burner beams and other accessories. Fig. 1.5 and Fig. 1.6 display the burner lances in a RCE kiln and the typical burner beams implemented in the FERCALX kiln, respectively.

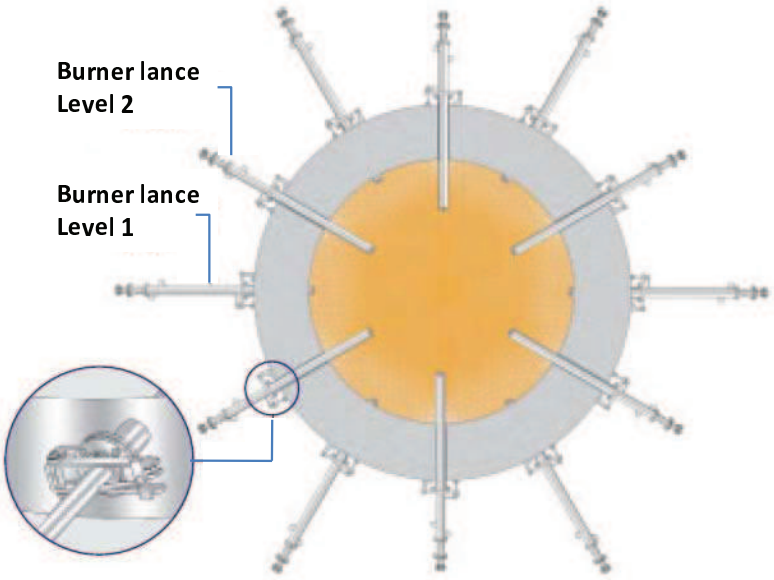

Figure 1.5: The top view of the burners in the RCE shaft kiln

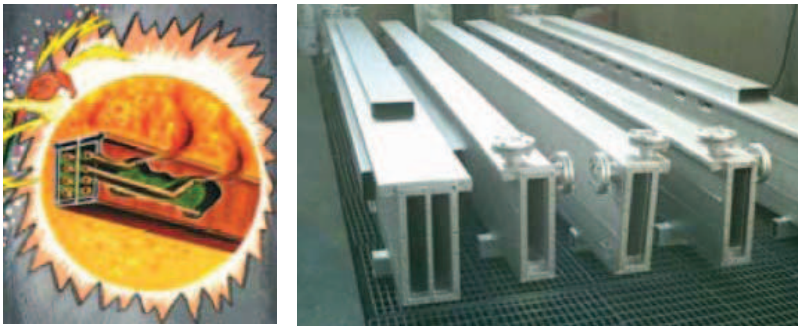

Figure 1.6: The typical burner beams applied to the FERCALX shaft kiln [12]

For a single burner, there are several different types in use for various proposes. Based on the types of fuel supplied, the typical burners are gas burner, oil burner,

coal burner, and wood burner. The gas burner usually classified according to how oxidizer-fuel mixture takes place. The most commons are premixed, diffusion and partially premixed burner [13].

In premixed burner, fuel and oxidizer are perfectly mixed before ignition starts. In this case, the flame is short and compact. This type of burner typically is applied in cracking and reforming furnaces, or furnaces with low available draft at the burners. Fig. 1.7 shows such a burner. It comprises a venturi section, whereby the fuel pressure aspirates combustion air and provides the mixing energy.

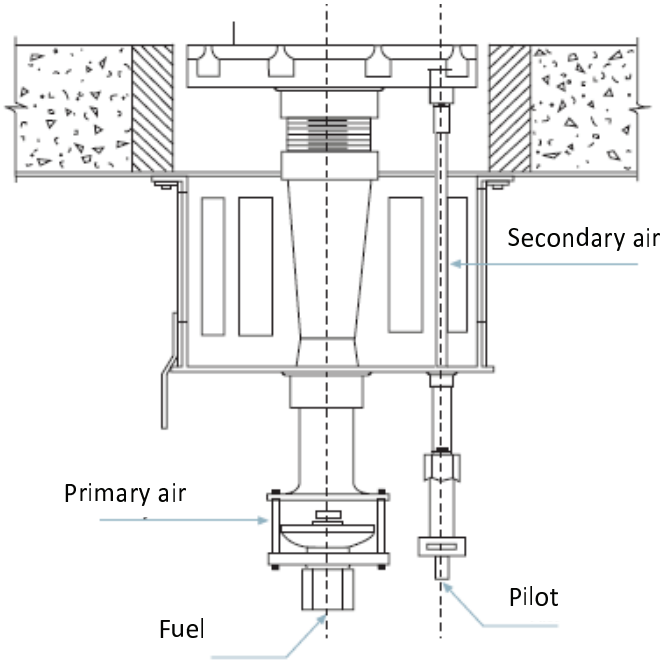

Figure 1.7: Schematic of a premixed burner [2]

Figure 1.8: Schematic of a diffusion burner [3]

On the other hand, in a diffusion burner the fuel and oxidizer are in separate streams prior to combustion (Fig. 1.8). Combustion only takes place at the the surface of diffusion flame, where the fuel meets oxygen in the right concentration. As a result, the flames tend to burn slower and have lower temperature. To produce soft-burnt lime, the diffusion burner has its advantages on temperature and radial fuel distribution.

Many different fuels are used in lime kilns. The most common in the EU is natural gas, but coal, coke and fuel oil are also widely used. Fuels markedly affect the heat usage, output and product quality. Some fuels require a special refractory kiln lining. Table 1.2 shows fuels used in lime shaft kilns.

In this work, only natural gas is used for simulation.

Table 1.2: Fuels used in lime-burning [EuLA]

Type of fuel	Widely used	Sometimes used	Rarely used
Solid	Bituminous coal Coke	Anthracite Lignite Pet coke	Peat Oil shales
Liquid	Heavy fuel oil	Medium fuel oil	Light fuel oil
Gaseous	Natural gas	Butane/propane	Town gas
Producer gas		Unconventional wood Used tyres Paper,Plastic etc.	Biomass Waste of liquid and solid fuels

1.3 Common problems in normal shaft kilns

Working as ideal counter-current flow heat exchangers, the normal shaft kilns have quite efficient heat transfer in preheating and cooling zone. In calcination zone, however, these furnaces have many heating problems, such as "hot spots" or cool channels, refractory over-heating, and surplus heat available etc. Most of them ascribe to two major problems. The first is related to the high temperature of the calcination zone during complete fuel combustion. The second is the poor radial gas mixing in the furnace working volume.

1.3.1 High temperature of the combustion zone

The decomposition temperature depends on the partial pressure of the carbon dioxide present in the process atmosphere. In a combustion gas atmosphere of normal pressure and 25% CO_2, the dissociation of limestone commences at 810 ^oC. In an atmosphere of 100% CO_2, the initial dissociation temperature would be 900 ^oC. In order to fully calcine the stone and have no residual core, a temperature of 900 ^oC has to be reached in the core at least for a short period of time since the atmosphere inside the material is pure CO_2. Therefore, the stone surface must be heated to greater than 900 ^oC to maintain the required temperature gradient so that the heat can penetrate the insulating effect of the calcined material via conductive heat transfer. In light of this, temperature in the calcination zone ranging from 900 to 1200 ^oC is preferable. However, the thermo-chemical processes, occurring in the shaft kilns are much more complicated, and normally the heat provided for calcining in the calcination zone is locally over-supplied due to the counter-current flow of material and gases.

The calcination process is practically complete at the bottom segment of the calcination zone. The reaction front is located in the lump core close to the center of the lump. In this case, the heat resistance of the lump calcined shell limits the heat transfer from the surface of the lump to the reacting core. At the same time fuel injection and combustion occur at this level of the calcination zone. The

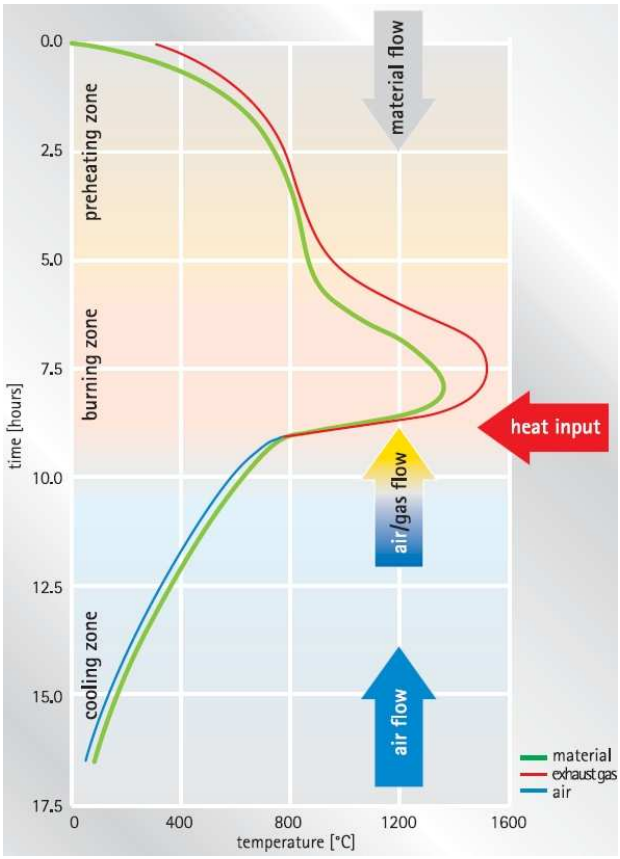

Figure 1.9: Temperature profile in a counter flow kiln [4]

temperature of the gases formed during complete fuel combustion can reach 1800-2000 ^oC. The temperature of the material surface can exceed 1500-1600 ^oC, and even with a very high excess air number, e.g. 1.7-1.8, the surface temperature can still reach 1300-1350 ^oC, as illustrated in Fig. 1.9. This disadvantage will reduce lime activity and thereby limits the application of the products, and even result in the formation of thermal NO_x.

1.3.2 Non-uniformity of gas distribution

Uniform gas distribution is another problem in shaft kilns. In normal shaft kilns, when the fuel is injected at the wall of a kiln, it usually does not penetrate more than 1 meter into the burden due to the high aerodynamic resistance of the packed material. Regarding that the modern shaft kilns for limestone calcination may have an internal diameter up to 7 meters, it is practically impossible to obtain uniform operation of the furnace cross-section with the combination of peripheral gas distribution tuyeres and water or oil-cooled gas distribution beam burners. This leads to the formation of high temperature zones (hot spots), resulting in decreased quality of products, reduced productivity, and low thermal efficiency [14]. The radial temperature distribution is illustrated by a diagram shown as Fig. 1.10. The schematic of the burning zone is not to scale and the temperature profile is not exactly representative to the real case.

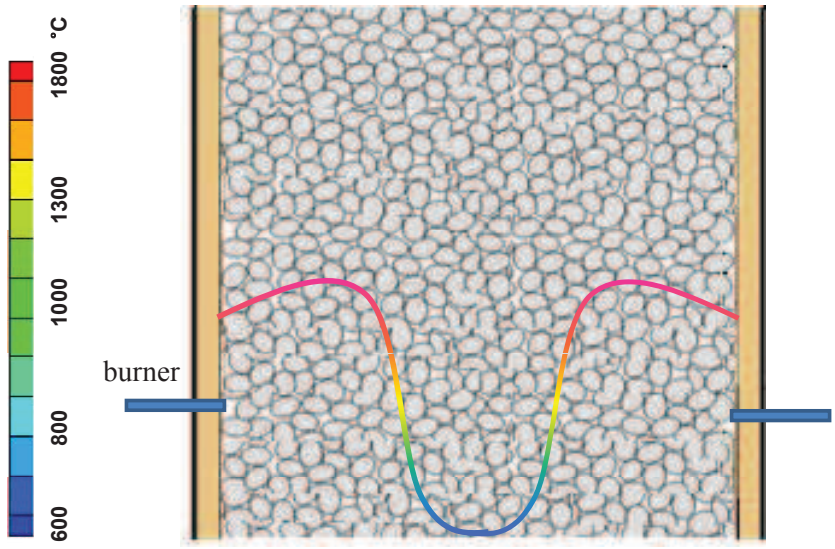

Figure 1.10: The radial temperature distribution in burning zone

To uniformly mix the fuel and the secondary air from the cooling zone, homogeneous distribution of the fuel over the entire shaft cross section should be achieved. This requires a firing system of good design. The normal firing system generally consists of a number of burner lances, which are situated at one or more levels.

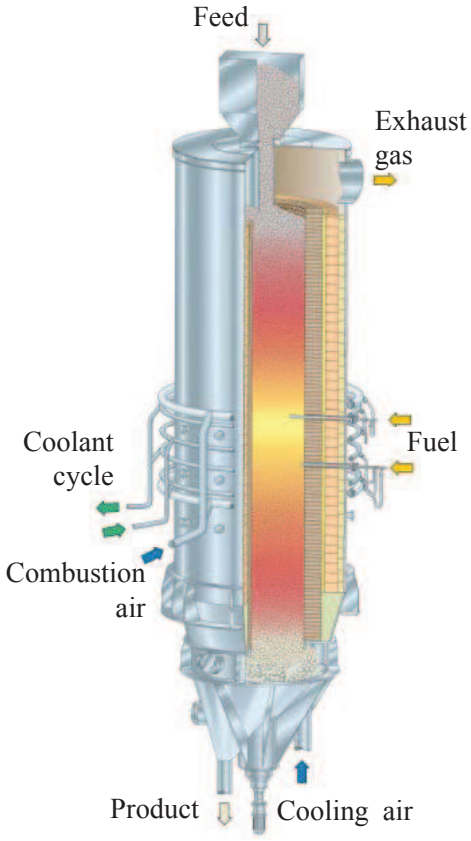

Figure 1.11: The structure of a RCE lime kiln

In the modern design, the distance of the burner tips from the center of the kiln can be adjusted to enable an optimum fuel distribution over the whole cross section of the kiln. Fig. 1.11 depicts such a kiln developed by RCE GmbH. With little knowledge of the in-kiln phenomena, however, it's not an easy task to handle with big-diameter kilns.

1.4 Modeling aided design

Shaft kilns have been developed a lot in the past decades. Most of the design variations are attempts to address these problems described above. However, the optimization is usually very empirical and costly because the industrial shaft kilns are large and complicated systems, and there are no measurements of temperature and concentration profiles are possible due to the movement of the high temperature solid. Response to the change of any of the operating parameters is noticeable only after a couple of days. Reproducing of the process in a laboratory scale furnace is very expensive either. In this case, the process modeling seems to be an interesting and efficient alternative comparing with investigation in experimental manner.

1.4.1 Dynamic process simulations

In fact, mathematical modeling has aided the design and operation of shaft kilns over the years. Many works have appeared in the literature [9, 15, 16, 17]. Most of these studies are based on thermal and material balance of the kilns with pressure drop calculated by Ergun equation. There are also some works in which calcination kinetics of limestone, geometric impacts, and the motion of the material and gases was concerned [18, 19, 20]. These models indeed have played an important role in the development of the modern shaft kilns, especially on optimization of the following aspects:

- Parameters of fuel combustion with respect to lime quality, fuel consumption, and ecological situation;
- Ratio of the preheating and calcination zone heights;
- Size of the limestone.

However, being lack of resolution of the detailed fluid phenomena in the kilns, these sorts of models have limited application on proving the firing system. As demands on the system performance increase, model needs to be able to give the insight into the physical mechanisms in order to acquire thorough knowledge of the problems, for instance, to localize regions of deficient or overheating. Computational fluid dynamics (CFD) is one of the critical "enabling technologies" to complement experimental findings in flow studies and has great potential to improve the available modeling strategies.

1.4.2 CFD approach

Computational fluid dynamics (CFD) is a state-of-the-art numerical technique for solving fluid flow problems. In a computational simulation the flow structure is computed by solving the mathematical equations that govern the flow dynamics. The result can be a complete description of the three-dimensional flow in the entire flow domain in terms of the velocity field and pressure distribution, including profiles of temperature variations, density and other related physical quantities. With the help offered by CFD engineers can easily predict, manipulate, and design the desired fluid dynamics in process equipment. More concepts on CFD are going to be specified in Chapter 2. With improvements in computer hardware, computational speed and memory size, as well as the development in software capabilities, CFD nowadays has a wide range of applications even to solve industrial flow problems. On shaft kilns, however, no CFD flow studies have been presented so far due to the extremely complex geometry definition as well as the limitation in computational power. In view of that a normal shaft kiln is basically a packed bed reactor, CFD modeling in packed beds is reviewed in the next Chapter.

1.5 Objectives

The objectives of this study are:

(1) Developing less expensive geometric models which can be applied to simulate the flow in the industrial-scale shaft kilns using CFD. This task is to be accomplished in two steps. In the first, two-dimensional (2-D) geometries are created and properly meshed to study some important parameters of interest. And then, three-dimensional (3-D) geometric models are developed;

(2) Performing grid independence study. Try to find the proper grids for 2-D and 3-D simulation

(3) Carrying out simulations with a commercial CFD code FLUENT 6.2. The key design factors shaft kilns, like lance depth, lance diameter, lance arrangement, as well as preheating of combustion air, are going to be investigated via CFD modeling in this part, and the flow pattern in the burner region of the shaft kilns will be visualized. The viability of the geometric models for discrete particle model is expected to be demonstrated.

(4) In the last, simulations based on porous media will be performed and compared with discrete particle modeling to show the advantages and limitations of defining the kiln as a porous medium body.

1.6 Summary

The general information on lime and lime production was presented at the beginning of this chapter. It is followed by the common problems encountered

in the industrial production equipment, and a short review of the known mathematical models and the new approach, computational fluid dynamics, with which engineers attempt to address the problems. Finally, the objectives of this work were enumerated.

Chapter 2

Computational Fluid Dynamics in Packed Bed Reactors

2.1 Computational Fluid Dynamics

Applying the fundamental laws of mechanics to a fluid gives the governing equations for a fluid, including the conservation of mass equation and the conservation of momentum equation. These equations along with the conservation of energy equation form a set of coupled, non-linear partial differential equations, which are not able to be solved analytically for most engineering problems.However, it is possible to obtain approximately computer-based solutions. This is the subject matter of Computational Fluid Dynamics.

2.1.1 Applications of CFD

Early users of CFD were mainly found in the automotive, aerospace, and nuclear industries, and CFD was confined to large organizations capable of developing and supporting their own codes using experts in CFD. With the enhancement of computing power and efficiency, the availability of affordable CFD packages, and low-cost but powerful computers, applications of CFD have extended into a huge number of areas, including:

- Aerodynamics (aircraft; automobiles);
- Hydrodynamics (ships; submersibles);
- Engine flows (internal-combustion and jet engines);
- Turbomachinery;
- Combustion and heat transfer;
- Process engineering (Chemical industry);
- Wind and wave power;

- Wind loading (forces and dynamic response of structures);
- Ventilation;
- Fire and explosion hazards;
- Environmental engineering (transport of pollutants and effluent);
- Hydraulics (pipe networks and channels; hydraulics structures);
- Oceanography (tidal flows; ocean currents);
- High-energy physics (plasmas; magnetohydrodynamics);
- Biomedical Engineering (heart and blood vessels; lungs and air passages);
- Electronics (heat dissipation).

This range of applications is broad and encompasses many different fluid phenomena and CFD techniques. Just as Jean Thilmany, the associate editor of ASME, said "Thirty years ago, CFD was academic; now doctors and engineers wonder how they lived without it".

2.1.2 Computation of fluid motions

Each CFD software package has to produce a prediction of the way in which a fluid will flow for a given situation. To do this the package must calculate numerical solutions to the equations that govern the flow of fluids. The generalize equations that are used by FLUENT, one of the ANSYS commercial CFD packages, are the Navier Stokes equations for conservation of mass and momentum, when it is set to calculate laminar flow without heat transfer. Additional equations are solved for heat transfer, species mixing or reaction or turbulent cases. The basic equations and background of theses equations are stated in the FLUENT 6.2 User's Guide.

Navier Stokes equations

The general equation for conservation of mass, or the continuity equation, is defined as follows:

$$\frac{\partial \rho}{\partial t} + \nabla \cdot (\rho \vec{u}) = S_m \tag{2.1}$$

where the source S_m is the mass added to the continuous phase from the dispersed second phase (e.g., due to vaporization of liquid droplets) and any user-define sources.

Conservation of momentum in an inertial (non-accelerating) reference frame is described by

$$\frac{\partial}{\partial t}(\rho\vec{u}) + \nabla \cdot (\rho\vec{u}\vec{u}) = -\nabla p + \nabla \cdot \bar{\bar{\tau}} + \rho\vec{g} + \vec{F} \tag{2.2}$$

where p is the static pressure, $\bar{\bar{\tau}}$ is the stress tensor (described below), and $\rho\vec{g}$ and $\vec{F}$ are the gravitational body force and external body forces (e.g., that arise from interaction with the dispersed phase), respectively. $\vec{F}$ also contains other model-dependent source terms such as porous-media and user-defined sources.

The stress tensor $\bar{\bar{\tau}}$ is given by

$$\bar{\bar{\tau}} = \mu\left[\left(\nabla\vec{u} + \nabla\vec{u}^T\right) - \frac{2}{3}\nabla \cdot \vec{u}I\right] \tag{2.3}$$

where μ is the molecular viscosity, I is the unit tensor, and the second term on the right hand side is the effect of volume dilation.

Turbulence models

Turbulent flows are characterized by fluctuating velocity fields. These fluctuations mix transported quantities such as momentum, energy, and species concentrations, and cause the transported quantities to fluctuate as well. Since these fluctuations can be of small scale and high frequency, they are too computationally expensive to simulate directly in practical engineering calculations. Turbulence models have been developed to meet this requirement.

Turbulence models are generally classified according to which governing equations they apply to (e.g. Reynolds-Averaged Navier-Stokes (RANS) or Large Eddy Simulation (LES) equations). Basically there are three possible approaches:

- **Reynolds-Averaged Navier Stokes (RANS)** This is the predominant approach applied in engineering CFD packages. RANS-based models solve all quantities for the mean values and therefore greatly reduce the required computational effort and resources, and is widely adopted for practical engineering applications.

- **Large Eddy Simulation (LES)** In this approach, the turbulent large scales are explicitly calculated whereas the effects of smaller ones are modeled using subgrid closure rules. LES is particularly appealing for IC applications, which is attracting more research efforts.

- **Direct Numerical Simulations (DNS)** DNS solve the full instantaneous Navier-Stokes equations without any model for turbulent motions.

Choosing an appropriate turbulence model is important but tough as no single model is universally accepted as being superior for classes of problems. The choice of turbulence model depends on considerations such as the physics encompassed in the flow, the established practice for a specific class of problem, the level of accuracy required, the available computational resources, and the amount of time available for the simulation.

Detailed descriptions on turbulent models are available on many works [21, 22, 23], including the FLUENT User's Guide. M. Nijemeisland et al. intensively studied the influence of turbulence models on modeling packed bed reactors, and found that there were no significant differences in the results [24]. The same result was obtained by H.P.A. Calis et al in modeling structured catalytic reactor packing [25]. In this research, a RANS-based Two-Equation model, the standard κ-ϵ model was used for CFD simulation because of its cost-effectiveness and reasonable accuracy for a wide class of flows and the extremely complicated geometry of shaft kilns.

The standard κ-ϵ model is by far the most popular and most widely used turbulence model especially for industrial applications. It is a semi-empirical model, and consists of two transport equations, one for the specific turbulence kinetic energy (κ) and one for the turbulence dissipation rate (ϵ). The transport equations for this model are

$$\frac{\partial}{\partial t}(\rho\kappa) + \frac{\partial}{\partial x_i}(\rho\kappa u_i) = \frac{\partial}{\partial x_j}\left[\left(\mu + \frac{\mu_t}{\sigma_\kappa}\right)\frac{\partial \kappa}{\partial x_j}\right] + G_\kappa + G_b - \rho\epsilon + S_\kappa \tag{2.4}$$

$$\frac{\partial}{\partial t}(\rho\epsilon) + \frac{\partial}{\partial x_i}(\rho\epsilon u_i) = \frac{\partial}{\partial x_j}\left[\left(\mu + \frac{\mu_t}{\sigma_\epsilon}\right)\frac{\partial \epsilon}{\partial x_j}\right] + C_{1\epsilon}\frac{\epsilon}{\kappa}(G_\kappa + C_{3\epsilon}G_b) - C_{2\epsilon}\rho\frac{\epsilon^2}{\kappa} + S_\epsilon \tag{2.5}$$

In the equations, G_κ represents the generation of turbulence kinetic energy due to the mean velocity gradients, defined as

$$G_\kappa = -\rho\overline{u_i' u_j'}\frac{\partial u_j}{\partial x_i} \tag{2.6}$$

G_b is the generation of turbulence kinetic energy due to buoyancy, and can be obtained by

$$G_b = \beta g_i \frac{\mu_t}{Pr_t}\frac{\partial T}{\partial x_i} \tag{2.7}$$

where Pr_t is the turbulent Prandtl number for energy and g_i is the component of

the gravitational vector in the ith direction, while β is the coefficient of thermal expansion, defined by

$$\beta = -\frac{1}{\rho}\left(\frac{\partial \rho}{\partial T}\right)_p \tag{2.8}$$

With known κ and ϵ, the turbulent (or eddy) viscosity, μ_t, is calculated as

$$\mu_t = \rho C_\mu \frac{\kappa^2}{\epsilon} \tag{2.9}$$

The model constants are,

$C_{1\epsilon}$=1.44, $C_{2\epsilon}$=1.92, C_μ=0.09, σ_κ=1.0, σ_ϵ=1.3

These default values have been determined from experiments with air and water for fundamental turbulent shear flows including homogeneous shear flows and decaying isotropic grid turbulence. They have been found to work fairly well for a wide range of wall-bounded and free shear flows [26]. In this study, all simulations were carried out based on the default settings.

Energy equations

The energy equation can be written in many different forms. FLUENT solve the equation in the following form,

$$\frac{\partial \rho E}{\partial t} + \nabla \cdot \left(\vec{u}\left(\rho E + p\right)\right) = \nabla \cdot \left(\left(k + k_t\right)\nabla T - \sum_j h_j \vec{J}_j + \left(\overline{\overline{\tau}} \cdot \vec{u}\right)\right) + S_h \tag{2.10}$$

where k_t is the turbulent thermal conductivity, defined according to the turbulence model being used, and $\vec{J}_j$ is the diffusion flux of species j. The first three terms on the right-hand side represent energy transfer due to conduction, species diffusion, and viscous dissipation, respectively. S_h includes the heat of chemical reaction, and any other volumetric heat sources defined by user.

In Eq.2.10,

$$E = h - \frac{p}{\rho} + \frac{u^2}{2} \tag{2.11}$$

where sensible enthalpy h is defined for ideal gases as

$$h = \sum_j Y_j h_j \tag{2.12}$$

and for incompressible flows as

$$h = \sum_j Y_j h_j + \frac{p}{\rho} \tag{2.13}$$

In Eq.2.12and 2.13, Y_j is the mass fraction of species j and

$$h_j = \int_{T_{ref}}^{T} c_{p,j} dT \tag{2.14}$$

where T_{ref} is 298.15 K.

Modeling reacting flows

The term 'reacting flows' applies to a broad range of physical phenomena. For gas-phase reacting flows, a set of coupled partial differential equations describe the motion of the fluid, species reactions, transport processes like conduction of heat molecular diffusion and thermal radiation. The set of PDEs needed to be solved for reacting flow simulation are described by Oran and Boris [27]. FLUENT predicts the local mass fraction of each species, Y_i, through the solution of a convection-diffusion equation for the ith species. The conservation equation takes the following general form:

$$\frac{\partial}{\partial t}(\rho Y_i) + \nabla \cdot (\rho \vec{u} Y_i) = -\nabla \cdot \vec{J}_i + R_i + S_i \tag{2.15}$$

where R_i is the net rate of production of species i by chemical reaction and S_i is the rate of creation by addition from the dispersed phase plus any user-defined sources.

In Eq.2.15, J_i is the diffusion flux of species i, which arises due to concentration gradients. In turbulent flows, FLUENT computes the mass diffusion by

$$\vec{J}_i = -\left(\rho D_{i,m} + \frac{\mu_t}{Sc_t}\right) \nabla Y_i \tag{2.16}$$

where $D_{i,m}$ is the diffusion coefficient for species i in the mixture, and Sc_t is the turbulent Schmidt number (defined as Eq.2.17). The default Sc_t is 0.7.

$$Sc_t = \frac{\mu_t}{\rho D_t} \tag{2.17}$$

where μ_t is the turbulent viscosity and D_t is the turbulent diffusivity.

To model reacting flows, FLUENT provides four approaches which are briefly described below:

- **Generalized Finite-Rate Model** This approach is based on the solution of transport equations for species mass fraction, with the chemical reaction mechanism defined by the users. The reaction rates that appear as source terms in the species transport equations are computed from Arrhenius rate expressions, from the eddy dissipation model or from the EDC model. Models of this type are suitable for a wide range of applications including premixed, partially premixed, and non-premixed combustion. According to the guidelines given by the FLUENT6 User's Guide, this model is used for cases involving the mixing, transport, or reaction of chemical species, or reactions on the surface of a wall or partical.

- **Non-Premixed Combustion Model** In this approach individual species transport equations are not solved. Instead, transport equations for one or two conserved scalars (the mixture fractions) are solved and individual component concentrations are derived from the predicted mixture fraction distribution. This approach has been specifically developed for the simulation of turbulent diffusion flames and offers many benefits over the finite-rate formulation. In the conserved scalar approach, turbulence effects are accounted for with the help of a probability density function (PDF). Reaction mechanisms are not defined by users; instead the reacting system is treated using a flame sheet (mixed-is-burned) approach or chemical equilibrium calculations. For reacting systems involving turbulent diffusion flames that are near chemical equilibrium where the fuel and oxidizer enter the domain in two or three distinct streams, use this model.

- **Premixed Combustion Model** This model has been specifically developed for combustion systems that are of the purely premixed type. In these problems perfectly mixed reactants and burnt products are separated by a "flame front". The "reaction progress variable" is solved to predict the position of the front. The influence of turbulence is accounted for by means of a turbulent flame speed. Consequently, this model can be used for cases with a single, perfectly premixed reactant stream.

- **Partially Premixed Combustion Model** Just as the name implies, the partially premixed combustion model has been developed for systems that have a combination of non-premixed and perfectly premixed combustion. The mixture fraction equations and the reaction progress variable are solved to determine the species concentrations and position of the flame front, respectively.

For a firing system of shaft kilns, the oxidant, air, is injected into the kiln by two separate streams. One is introduced form the bottom of the kiln as cooling air, and the other is blown in with fuel but without premixed. In view of this, the Generalized Finite-Rate model was used.

In Generalized Finite-Rate approach, the reaction rates that appear as source terms in Eq.2.15 are computed in FLUENT by one of three models:

- Laminar finite-rate model: The effect of turbulent fluctuations are ignored, and reaction rates are determined by Arrhenius expressions.
- Eddy-dissipation model: Reaction rates are assumed to be controlled by the turbulence and therefore expensive Arrhenius chemical kinetic calculations can be avoided. The model is computationally cheap, but, for realistic results, only one or two step heat-release mechanisms should be used.
- Eddy-dissipation-concept model: This is an extension of the eddy-dissipation model to include detailed Arrhenius chemical kinetics in turbulent flows. However, typical mechanisms are invariably stiff and their numerical integration is computationally costly. Hence, the model should be used only when the assumption of fast chemistry is invalid, such as modeling the slow CO burnout in rapidly quenched flames.

Considering the reacting flows in shaft kilns are turbulent, the eddy-dissipation model was applied.

2.1.3 Discretization methods

As being described above, the equations governing the motion of fluids are partial differential equations. These equations can not be solved directly by digital computers unless they are numerically discretized. A variety of techniques can be used to perform this numerical discretization, and among them there are three major techniques: the finite difference method, the finite element method, and the finite volume method.

- **Finite difference method** This method is based upon the use of so-called Taylor series to build a library of equations that describe the derivatives of a variable as the difference between values of the variable at various points in space or time. A comprehensive reference to the finite difference method is Smith [28]. This method has historical importance and is currently used in few specialized codes.
- **Finite element method (FEM)** In this method the domain over which the partial differential equations apply is split into a finite number of sub-domains known as elements. Over each element a simple variation of the dependent variables is assumed and this piecewise description is used to build up a picture of how the variables vary over the whole domain. A good introductory text to FEM is Reddy [29]. This method is popular for structural analysis of solids, but is also applicable to fluid. Commercial CFD code ANSYS uses FEM.
- **Finite volume method (FVM)** FVM has been developed specifically to solve the equations of heat transfer and fluid flow, and is probably the most popular numerical discretization method used in CFD. This method is similar in some ways to the finite difference method, but some implementations of it also draw on features taken from the FEM. A good reference is Patankar

[30]. FLUENT uses this method, and ANSYS CFX uses a hybrid finite element/finite volume approach.

2.1.4 Grid generation and near-wall treatment

Grid types

In order to analyze fluid flows, flow domains must be split into smaller sub-domains (made up of geometric primitives like hexahedra, prisms, and tetrahedra in 3D, and quadrilaterals and triangles in 2D, as shown in Fig. 2.1) and then discretized governing equations are solved inside each of these portions of the domain. Each of these portions of the domain are known as elements or cells, and the collection of all elements is known as mesh or grid.

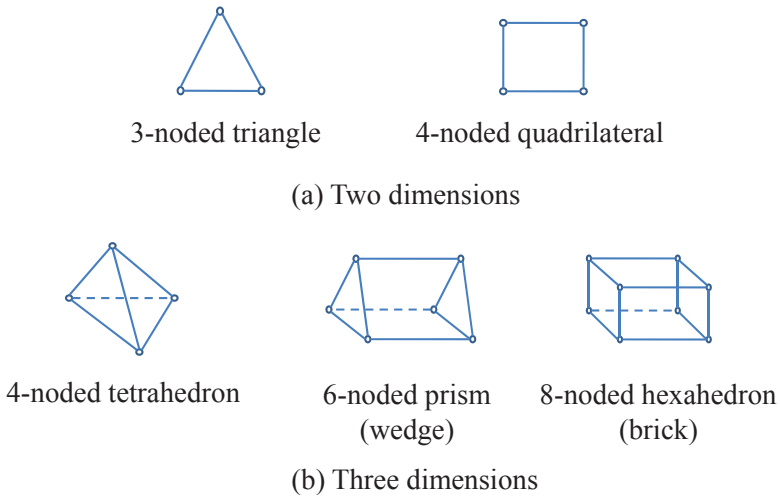

Figure 2.1: Some common sub-domains

Grid generation is often considered as the most important and most time consuming part of CFD simulation. The quality of the grid plays a direct role on the quality of the analysis, regardless of the flow solver used. Additionally, the solver will be more robust and efficient when using a well structured mesh. Typically, three types of grids are in widespread use.

- **Structured grids** Structured grids take their name from the fact that the grids are laid out in a regular repeating pattern called a block. The type of grids utilize quadrilateral elements in 2D and hexahedral elements in 3D in a computationally rectangular array. Although the element topology is fixed, the grid can be shaped to be body fitted through stretching and twisting of the block, and the meshes can consist of several blocks to be connected together, an example shown in Fig.2.2.

  Structured grids enjoy a considerable advantage over other grid methods in that they allow the user a high degree of control. In addition, structured block flow solvers typically require the lowest amount of memory for a given size and execute faster because they are optimized for the structured layout

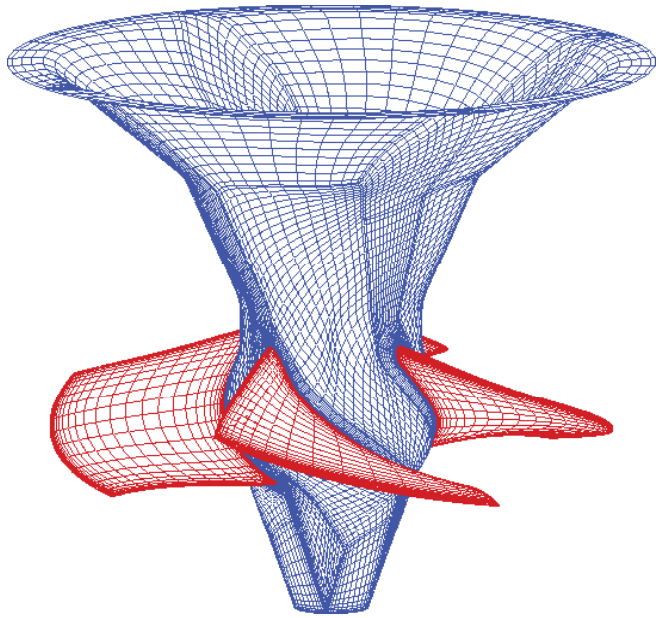

Figure 2.2: An example of a structured multiblock grid. Only the grid planes attached to surfaces are shown. [31]

of the grid. Lastly, postprocessing of the results on a structured block grid is a much easier task because the logical grid planes make excellent reference points for examining the flow field and plotting the results. For cases with complicated geometry, however, structured grid generation can be extremely time consuming. Some geometries even do not lend themselves to structured block topologies. The user is hence forced to stretch or twist the elements to a degree which can drastically affects solver accuracy and performance.

- **Unstructured grids** An unstructured grid is characterized by irregular connectivity. These types of grids typically utilize triangles in 2D and tetrahedral in 3D. Fig. 2.3 depicts an unstructured mesh consisting of tetrahedral elements.

  The advantage of unstructured grid methods is that they are very automated and, therefore, require little user time or effort. The user need not worry about laying out block structure or connections. Unstructured methods also enable the solution of very large and detailed problems in a relatively short period of time.

  The major drawback of unstructured grids is the lack of user control. The user involvement is limited to the boundaries of the mesh with the mesher automatically filling the interior. Triangle and tetrahedral elements have the problem that they do not stretch or twist well, and therefore the grid is limited to being largely isotropic, i.e. all the elements have roughly the same size and shape. Of course, with the development of grid generation techniques, for instance the size function, this sort of problems are being solved. Furthermore, unstructured flow solvers require more memory and have longer execution time than structured grid solvers on a similar mesh, because unstructured grids do not have a direct mapping between where

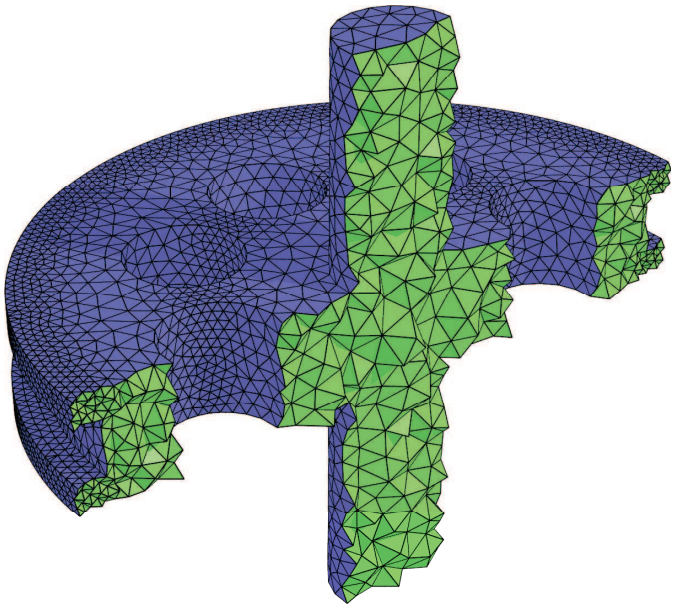

Figure 2.3: An example of an unstructured grid

things are in memory and how they connect in the physical space.

- **Hybrid grids** An example is illustrated in Fig. 2.4,grids of this type are designed to take advantage of the positive aspects of both structured and unstructured grids. Hybrid grids can contain hexahedral, tetrahedral, prismatic, and pyramid elements in 3D and triangles and quadrilaterals in 2D. The various elements are used according to their strengths and weakness. Hexahedral elements are excellent near solid boundaries (where flow field gradients are high) and afford the user a high degree of control, but are time consuming to generate. Prismatic elements (usually triangles extruded into

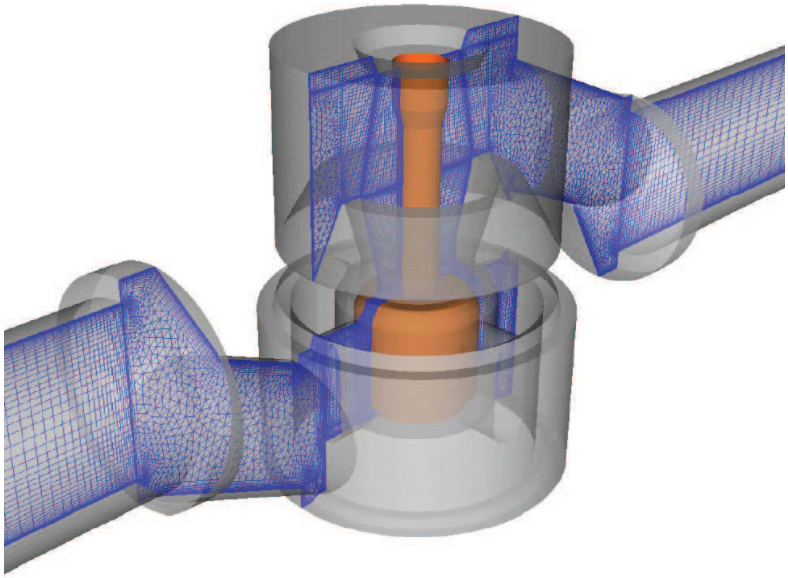

Figure 2.4: An example of a hybrid grid (CRAFT Tech)

wedges) are useful for resolving near wall gradients, but suffer from that fact that they are difficult to cluster in the lateral direction due to the underlying trangular structure. In almost all cases, tetrahedral elements are used to fill the remaining volume. Pyramid elements are used to transition from hexahedral elements to tetrahedral elements.

Another type of hybrid grid is the quasi-structured or "cooper" grid. This grid generation method allow for some sophisticated forms of growing the 3D mesh using a sweeping concept within a CAD solid model. One disadvantage of hybrid grid generation is that it is not easy to handle to get the best results. Additionally, hybrid grids are typically less robust than unstructured grids and flow solver will use more resources.

Near-wall treatment

Turbulent flows are significantly affected by the presence of walls. Therefore, accurate representation of the flow in the near-wall region determines successful prediction of wall-bounded turbulent flows. Numerous experiments have shown that the near-wall region can be largely subdivided into three layers. In the innermost layer, called the "viscous sublayer", the flow is almost laminar, and the (molecular) viscosity plays a dominant role in the momentum and heat or mass transfer. In the outer layer, called the fully-turbulent layer, turbulence plays a major role. Thirdly, there is an interim region between the viscous sublayer and the fully turbulent layer where the effects of the molecular viscosity and turbulence are equally important. Fig. 2.5 illustrates these subdivisions of the near-wall region, plotted in semi-log coordinates.

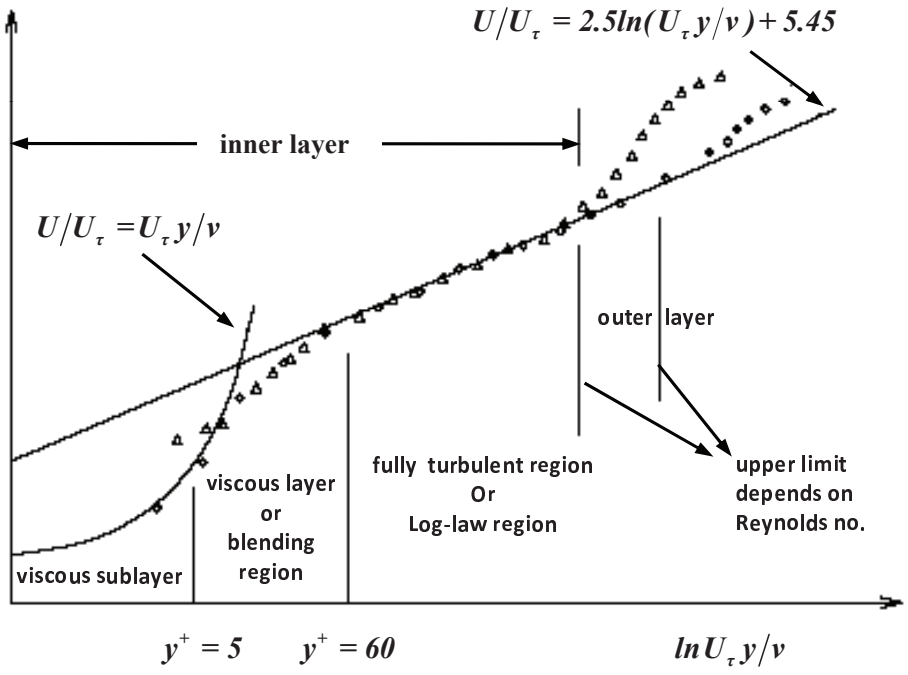

Figure 2.5: Subdivisions of the near-wall region [5]

In Fig. 2.5, y^+,Wall Yplus, is a non-dimensional parameter defined by the equation

$$y_+ = \frac{\rho u_\tau y}{\mu} \tag{2.18}$$

where, y is the distance from a point to the wall, ρ is the fluid density, μ is the fluid viscosity, and u_τ is the friction velocity, defined as

$$u_\tau = \sqrt{\tau_w/\rho} \tag{2.19}$$

FLUENT provides two traditional approaches to modeling the near-wall region. In one approach, the viscosity-affected inner region (viscous sublayer and buffer layer) is not resolved. Instead, semi-empirical formulas called "wall functions" are used to bridge the viscosity-affected region between the wall and the fully-turbulent region. The use of wall functions obviates the need to modify the turbulence models to account for the presence of the wall. The second one is termed as the "near-wall modeling" approach, in which the turbulence models are modified to enable the viscosity-affected region to be resolved with a mesh all the way to the wall. These two approaches are depicted schematically in Fig. 2.6.

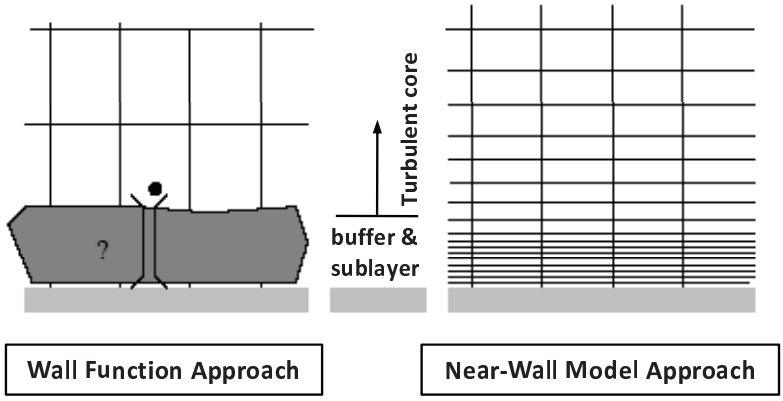

Figure 2.6: Near-wall treatments in FLUENT [5]

The wall function approach is a practical option for the near-wall treatments for industrial flow simulations because it is economical, robust and reasonably accurate. However, it is inadequate in situations where the low-Reynolds-number effects are pervasive in the flow domain in question, and the hypotheses underlying the wall functions cease to be valid. Some limitations of the wall function approach are presented in FLUENT documentation [5]:

• Pervasive low-Reynolds-number or near-wall effects (e.g., flow through a small gap or highly viscous, low-velocity fluid flow).

• Massive transpiration through the wall (blowing/suction).

• Severe pressure gradients leading to boundary layer separations.

• High three-dimensionality in the near-wall region (e.g., Ekman spiral flow, strongly skewed 3-D boundary layers).

In the case that any of the items listed above is a prevailing feature of the flow to be modeling, and if it is considered critically important to capture that feature for the success of the simulation, the near-wall modeling approach combined with adequate mesh resolution in the near-wall region must be employed. For such situations, FLUENT provides the enhanced wall treatment which can be used with the κ-ϵ models, the κ-ω models, and the RSM.

In this work, both the first item (flow through a small gap) and the third item (boundary layer separations) take place in the simulation. Therefore, the enhance wall treatment is used in 2-D modeling. However, the wall function is employed in 3-D modeling because the near-wall mesh should be fine enough (typically $y^+ \approx 1$) to use the enhanced wall treatment and this may lead to the computational cost prohibitively high.

2.1.5 The CFD process

Essentially there are three stages to every CFD simulation process: Preprocessing, solving and postprocessing.

• **Preprocessing** This is the first step in building and analyzing a flow model. It includes building the model within a computer-aided design (CAD) package, creating and applying a suitable computational mesh, and setting up the flow boundary conditions and fluid materials properties.

There are a great variety of meshing tools available in the market, such as GAMBIT, Tgrid, G/Turbo,ANSA, Harpoon, YAMS etc. Among them, GAMBIT is the FLUENT's own preprocessor, and CAD geometries generated in GAMBIT are easily imported and adapted for CFD solutions. Its unique curvature and proximity based "size function" produces a correct and smooth CFD-type mesh throughout the model. In this project, GAMBIT is used for the geometry construction and grid generation.

• **Solving** In this stage, the CFD solver carries out the flow calculations and produces the results. For someone who is new to CFD, selecting a CFD solver can sometimes be a daunting task due to the bewildering variety of choices. Some famous commercial providers of CFD codes are ANSYS, Inc., CD-Adapco, Aerosoft, Inc., and Cobalt Solutions, LLG etc. ANSYS, Inc. provides FLUENT and CFX solvers, and controls something like half of the commercial CFD market. FLUENT′ adaptive and dynamic physics is unique among CFD vendors and works a wide range of physical models.

• **Postprocessing** This is the final step in CFD analysis, and it involves the organization and interpretation of the predicted flow data and the production of CFD images and animations if necessary. Postprocessing is integrated in FLUENT solver, and users can perform sophisticated data analysis easily. FLUENT′ CFD data can also export to third-party postprocessors and visualization tools such as Ensight, Fieldview and Tecplot as well as to VRML formats.

2.2 CFD modeling of packed beds

2.2.1 CFD models: "porous medium" vs. "discrete particle"

In the field of packed-bed modeling, there are two different types of models in term "CFD simulation" [32]. In the first, the bed is represented as an effective porous medium, with lumped parameters for dispersion and heat transfer. The reactions that take place in the porous catalyst particles are represented by source or sink terms in the conservation equations and corrected for volume fraction and particle transport limitations. The velocity field can be obtained from a modified momentum balance or a form of the Brinkmen-Forcheimer-extended Darcy equation. These approaches provide an averaged velocity field, usually in the form of a radially varying axial component of velocity, which is an improvement over the classical assumption of plug flow. The disadvantages of this approach are the continued lumping of transport process and the lacking of detailed flow structure. This approach was applied by Rasul et al. [33] to model and simulate the thermodynamic process of vertical shaft kiln. The combustion, particle-gas dynamics and heat transfer processes were modeled by Eulerian multiphase model, and species transport and finite volume chemical reaction model. Though the authors declared that the simulated results showed a reasonably good agreement with designed data, the temperature profile through the kiln seems too high than practical, due to the steady state assumption and the exclusion of the decomposition process of dolomite. Therefore, the practical significance to model the heat transfer in shaft kilns producing soft-burnt lime is dubious. Additionally, the simulation was based on a 2-D geometric model. There is no doubt that the kiln can be axisymmetrical, but, the firing system is definitely not. In a 2-D model, a gap or slot shaped burner is used instead of a group of tube pipes. Thus the influence of the dimension of the slot and the setting of the boundary condition should be investigated intensively.

In the second type, the geometric complexities of the packing are not simplified, or replaced by the effective medium, and the flow through the space between particles is calculated by solving the Navier Stokes equations and others. In this approach, to solve the governing equations for the fluid flow itself is relatively simple, however, the geometric modeling and grid generation become complicated and the computation demands increase significantly. But it′s worthwhile as this approach yields very detailed solutions which are of great importance in understanding the phenomena that occur in the bed. Via this "discrete particle" approach, the complete characteristics of the flow in the entire flow domain can be described in terms of the main variables like velocity, pressure, and temperature and so on. In the following section, the literature review is based on this approach. Meanwhile, as the geometry building is one of the most important and time consuming process of CFD analysis, the review mainly focuses on the geometry development strategies in this field.

2.2.2 Achievements and challenges

The first CFD approaches included 2-D studies that resolved flow patterns and heat transfer around proposed ideal geometries. These early 2D simulations, summarized by Nijemeisland and Dixon [34], only focused on studying fluid through packed beds at a very low Reynolds number, e.g. creeping flow. In these cases, the geometries were very simple, generally only several spheres involved, including studies carried out by Lloyd and Boehm [35]. Even with the simple geometries, however, the results were much informative especially on the eddy formation, the effect of Re and Pr numbers on heat and mass transfer, and even the influence of the sphere spacing on the drag coefficients. In recent years, especially after 2000, there have been considerable studies carried out in 3-dimensional way. H. P.A. Calis et al. simulated the pressure drop and flow profile in a structured catalytic reactor packing by the commercial CFD package CFX-5 (AEA Technology), and validated the model by experimental results [25]. Fig. 2.7 shows the geometric model used in the simulation. This geometry was also employed by G. Dixon et

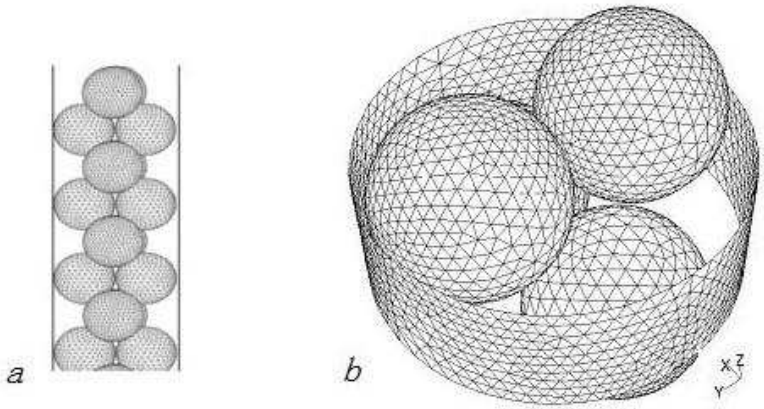

Figure 2.7: Side and close-up isometric view of a geometric model

al. who compared the CFD simulation to experiment for convection heat transfer in a gas-solid fixed bed, and gave a detailed investigation on the flow fields as well [34]. Though the studies were still limited by few particles and simple space structure, much information on the fluid flow structure was discovered more in detail comparing with 2-D simulations. Later, CFD applications in packed bed especially packed tubular rectors design had been extensively studied by Anthony G. Dixon group and Alfredo Guardo group [36, 32, 37, 38]. The tube-to-particle diameter ratio (N) was increased to 4, and particles were increased from 16 to 44. Meanwhile graded mesh was developed for the concern of the small gaps between particles and time saving. One example geometry is shown in Fig. 2.8.

Though great progress has been made on CFD flow simulation in packed-bed reactors, all works are restricted to low tube-to-particle diameter ratio due to the geometric complexity and computer power limitation. Calis et al. [25] investigated the mesh quality and the size of the grid cells needed for a grid-independent solution. The result showed that about three million cells are required for the simulation of a packed bed containing 16 particles if detailed study on turbulence character of the flow is required. While for a tube or rectangular channel, with the

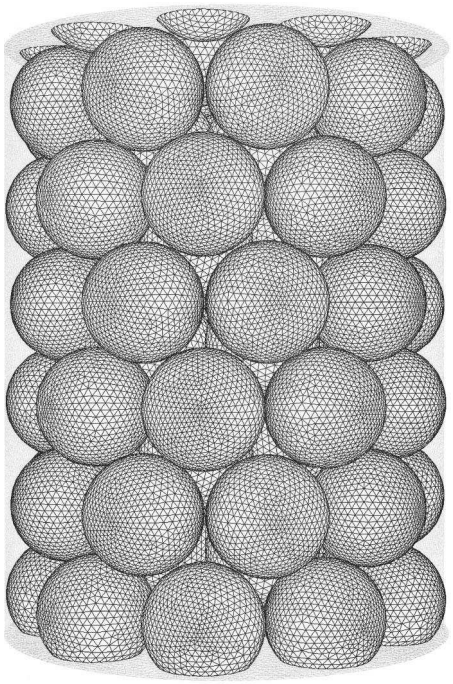

Figure 2.8: A full bed simulation geometry with graded surface mesh, N=4

increasing of the tube-to-particle diameter ratio, there will be a great increment of particles. This challenge is clearly depicted in Fig. 2.9. Apparently, to simulate a

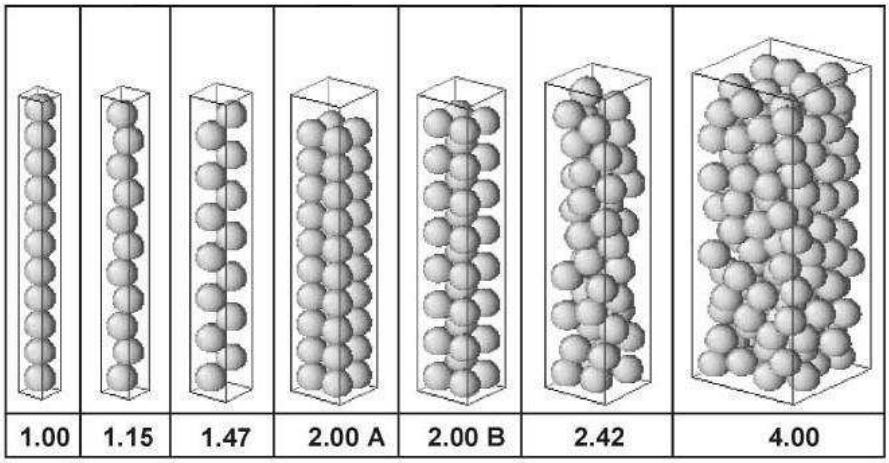

Figure 2.9: Isometric view of the arrangement of uniform spheres within a square vessel, for N changing from 1 to 4

complete industrial packed bed reactor in which there're thousands even millions of particles become prohibitively expensive.

To solve such a challenge, R.C. Hendricks et al. [39] managed to create a representative slice close to the real situation in a packed bed by using proper cutting planes, symmetry and periodicity boundaries. While, Dixon et al. [40] had put forward the Wall Section (WS) strategy , by which a bed segment with a certain angle was created as the geometric model, as shown in Fig. 2.10. With this method, M. Ertan Taskin simulated reactors packed with cylindrical catalyst

particles which is displayed in Fig. 2.11.

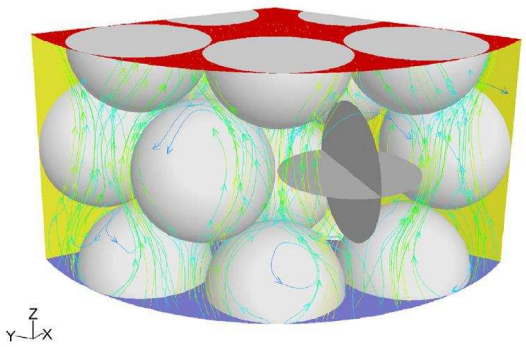

Figure 2.10: 3-D view of a wall segment geometry with flow path lines

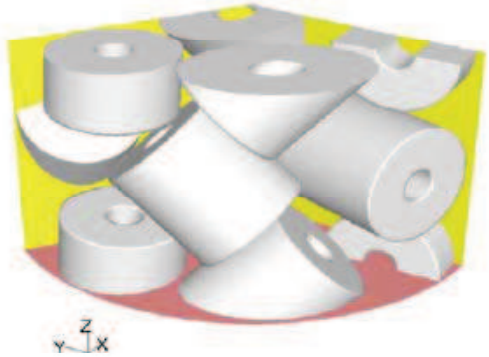

Figure 2.11: 3-D view of a wall segment geometry with cylindrical particles [6]

Another important subject in geometry generation is the construction of wall-to-particle and particle-to-particle contact points. If the contact point between two touching objects is defined by two nodes on walls of different entities, meshing process can not be carried out due to very high skewed grid elements around the contact.

In previous works, there are two methods to address this challenge. One is by leaving small gaps between surfaces and assuming zero velocity in the gap [24]. Fig. 2.12 shows the particle arrangement and the flow field with velocity vectors. In the other, the spheres were modeled by a small overlap, for instance 0.5% of their diameters, and thereby there were adjacent surfaces in the geometric model instead of 'points' [41]. A part of the geometry is shown in Fig. 2.13. In this work, small gaps between particles are used.

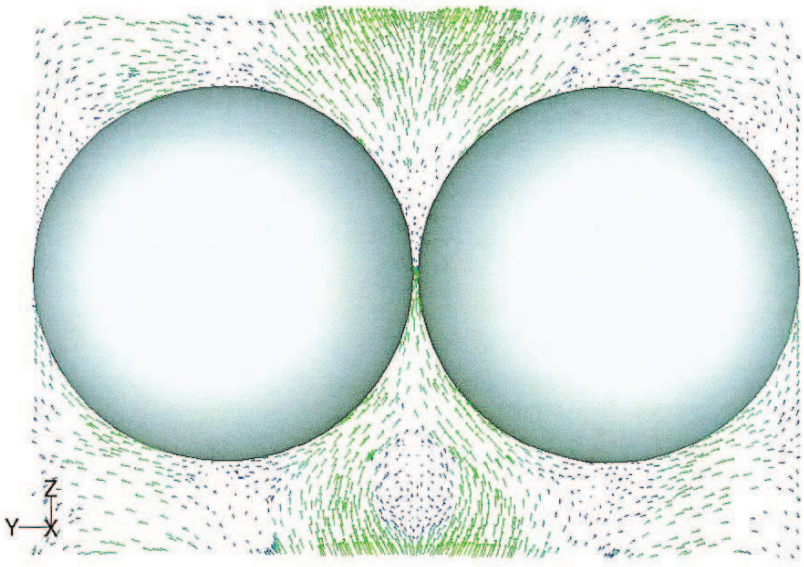

Figure 2.12: Geometric model with gaps between particles

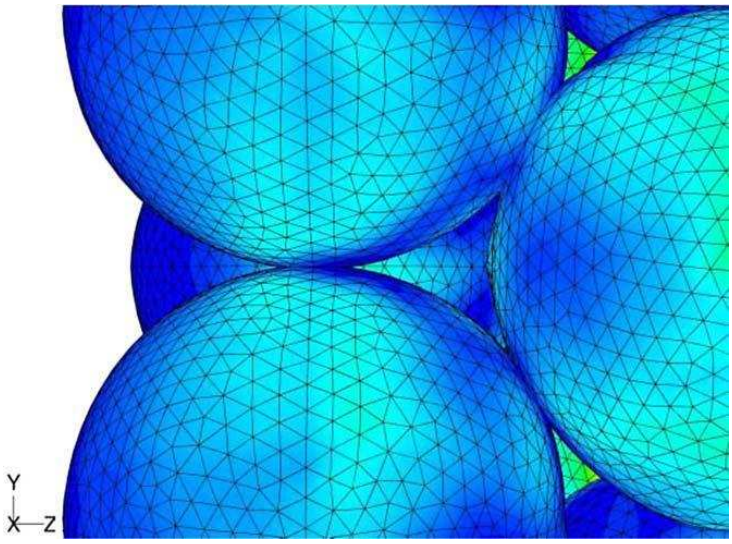

Figure 2.13: Geometric model with small overlap between particles

2.3 Summary

This chapter is devoted to the introduction on the fundamentals of the computational fluid dynamics and literature review of CFD application in modeling packed bed equipment in the past two decades. Due to the recent rapid grow of powerful computer resources and the development of general purpose CFD software packages CFD can nowadays be applied to solve industrial flow problems. The viability of using CFD analysis for packed bed reactors has been demonstrated by previous works. There are two types of models in terms of "CFD simulation", the "porous medium" and the "discrete particle". The later has the advantage of yielding a very detailed solution containing the local values of all relevant variables, such as pressure, velocities, temperature and so on. So far, however, studies based on this approach were restricted to low tube-to-particle diameter ratio, for instance $N \leq 4$, due to the extremely complicated geometry definition and of course the limitations of computer power. To model an industrial equipment like shaft kiln which has jet injections, the models defined with a small N is not applicable, whilst the big geometry contains huge amount of particles and lead to prohibitively computational cost. Wall segment strategy was put forward to address this challenge. For periodic flow, this method can reduce the model greatly and hence decrease the computational time. So far, however, no CFD based study on shaft kilns (packed bed reactors) in industrial scale has been done.

Chapter 3

Geometric Model Development

3.1 Geometry and process simplification

The geometry of a shaft kiln and the process that takes place inside are very complex. To model such a process based on a full representative "discrete particle" geometry is beyond the computer power so far and not necessary as well. In the first stage of developing the geometric model for simulation some simplifications were made as summarized below:

(1) Feeding port, discharging port, and cooling gas distributor not included. The shaft kilns normally consist of five parts, the main body lined with refractory materials, the feeding port on the top, the firing system in the middle, and the discharging port and the cooling gas distributor at the bottom, shown in Fig.3.1.

The discharging port has no influence on the flow structure in the kiln and is excluded in the model. The feeding port and the cooling gas distributor are assumed to work well and the desired radial particle distribution on the top and radial cooling air distribution through the cooling zone are achieved, and therefore both of them are not included in the model as well.

(2) Fixed bed. As a matter of fact, the solid phase is moving downwards the kiln during the continuous production. However, considering that the velocity of the bed′s movement is extremely slow, e.g. about 10 m/day in lime production, the bed is defined to be fixed.

(3) Regular packed spheres. Even though the limestones are sieved before feeding, they are varying in dimension and shape and packed in the kiln randomly. To model and simulate such a complicated system and process, the particles need to be generalized and packed in a specific pattern. In this work, the processed material granules are simplified to be uniform spheres and have a regular structure.

(4) No heat transfer between gas and solid. Heat transfer studies in packed beds are crucial for reactors design. Modeling the heat transfer in packed beds

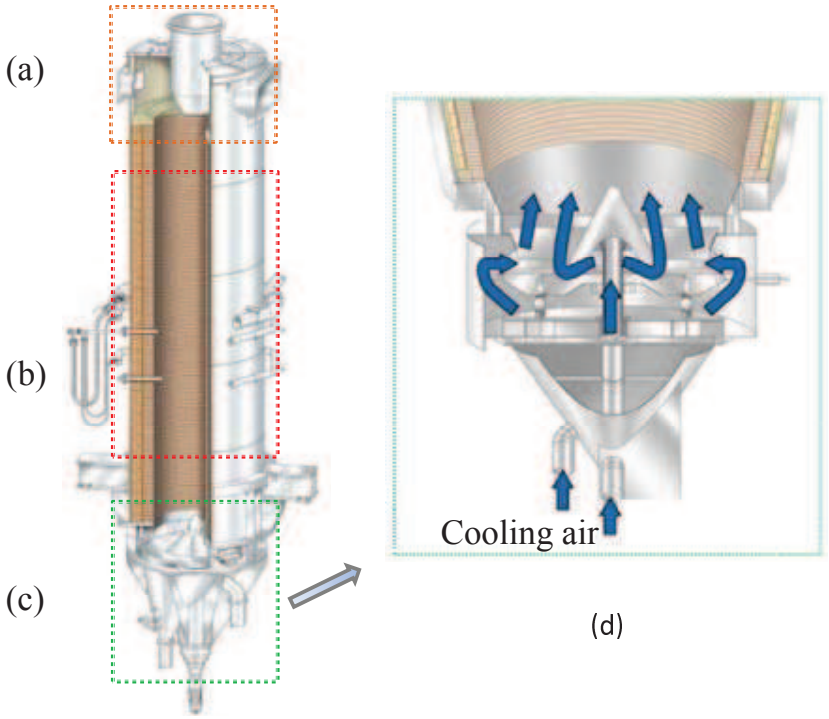

Figure 3.1: The schematic of RCE lime shaft kiln: (a) feeding port, (b) main body, (c) discharging port and cooling air distributor, and (d) close-up view of cooling air distributor

using CFD has been carried out by many scientists [42, 37, 38, 43], but all the works were conducted in beds of low tube-to-particle diameter ratio. The computational cost is extremely high or even beyond the power of computer to model and simulate a full scale equipment in this way. Fortunately, there have been lots of models dealing specifically with gas/solid heat transfer in packed bed equipment [9, 18, 44, 45], even CFD modeling using the Eulerian-Eulerian approach [46]. These works were based on homogeneous gas distribution and computationally cheaper, i.e. if homogeneous gas distribution can be achieved heat transfer can be numerically modeled with other approaches. Therefore, this work only focuses on flow analysis, and the behavior of the gas jet (burner) is of the most concern. However, the effect of heat transfer on the flow pattern is going to be studied with 2-D model.

(5) The radial void fraction distribution is constant. There is no doubt that the void fraction near the wall in a packed beds of spheres is larger than the average. The lower the tube-to-particle diameter ratio of the bed the bigger impact that this non-uniformity has on the flow pattern. For this project, however, the bed is huge relative to the particles, for instance $N \geq 20$. The influence was therefore not considered, and the wall was subtracted by particles to avoid a high local void fraction.

(6) Steady state. As the bed is regarded stationary, and heat transfer from gas-to-solid and the decomposition kinetics of limestone are not concerned, the process is assumed to be steady state.

3.2 2-D Geometric model development

3.2.1 Particle arrangement

The geometry of a shaft kiln is complicated because of the processed material the kiln is filled with. To develop the geometric model, how to arrange the particles, the limestones, is one of the fundamental challenges to tackle. In 2-D, however, spheres can not be modeled and therefore the structured packing of spheres becomes an array of tubes (tube bank). This is one of the deficits in 2-D modeling. Fig.3.2 shows the cross flow through a tube bank. The most common structures

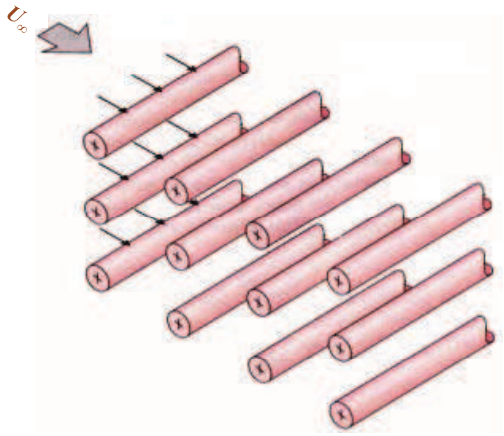

Figure 3.2: Flow through a tube bank

of tube banks are staggered and aligned in terms of the arrangement of the tube rows in the direction of fluid (Fig.3.3), and they are usually defined by the relative transverse $P_T = S_T/d$ and longitudinal $P_L = S_L/d$ center-to-center distances, called transverse and longitudinal pitches, respectively.

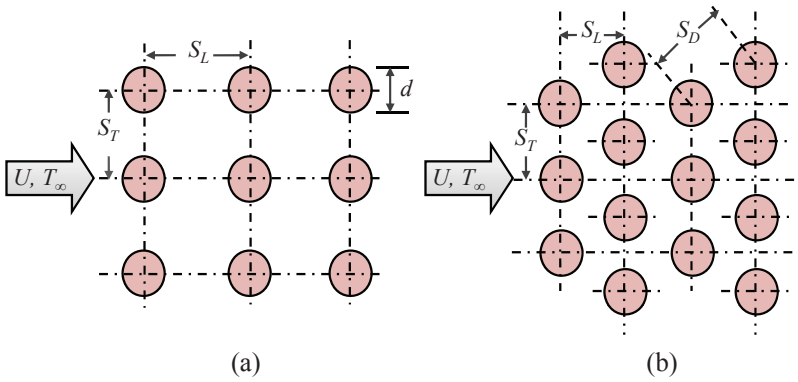

Figure 3.3: Arrangement of tubes in a bank: (a) aligned structure, (b) staggered structure

Obviously, the structure formed by aligned tube rows is too simple to be used. Therefore, staggered arrangement is selected, and the structure is generalized by defining the transverse pitch two times of the longitudinal pitch (S_T=2S_L), as shown in Fig.3.4.

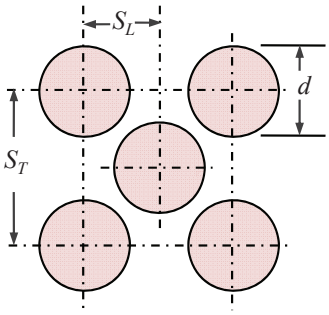

Figure 3.4: The arrangement in 2-D geometric model

The arrangement shown in Fig.3.4 may be viewed as a unit of the packed bed. According to the definition of the void fraction of a packed bed (φ), there is

$$\varphi = \frac{Bedvolume - Packingvolume}{Bedvolume} = \frac{S_T^2 - 2\frac{\pi d^2}{4}}{S_T^2} \tag{3.1}$$

where d is diameter of the particle (or tube in 2-D).

With given void fraction and particle size, the transverse distance can be determined by

$$S_T = d\sqrt{\frac{\pi}{2\,(1-\varphi)}} \tag{3.2}$$

3.2.2 Burner

As described in Chapter 1, the geometrical complexity of a burner depends largely upon its application. If short and intensive flame is necessary in application, premixed burner is required. In this case, the configuration of the burner can be very complicated, and CFD modeling of such burner itself is quite complex and time consuming [13, 2]. Generally, burners applied in lime shaft kilns are non-premixed and normally with relative simple geometry, for instance tube-in-tube structure. Limited by computer power, however, it′s still not possible to visualize the flow structure in a large-scale industrial shaft kiln, and at the same time gain the particular insight into the full burner system. To reduce the computational time thereby, only the tip of the burner is considered in the geometric model. In the case of the premixed burner, fuel and combustion air are assumed to be perfectly mixed prior to combustion. The simplified geometry for non-premixed burner or diffusion burner is depicted in Fig.3.5, in which d_f is the diameter of the fuel tube and d_b is the diameter of the burner lance.

Similarly as the limitation of modeling the spheres, 2-D model has deficit on tubular burners. As shown in Fig.3.6, burners can only be modeled as slot-in-slot instead of tube-in-tube, except the center burner which is exactly situated on the symmetry axis. Therefore, the distinction between the geometric specialty of the burner beam and the tubular burner were not considered in this work.

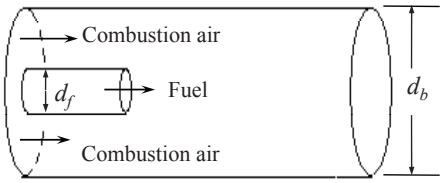

Figure 3.5: Schematic of the diffusion burner geometry in 3-D

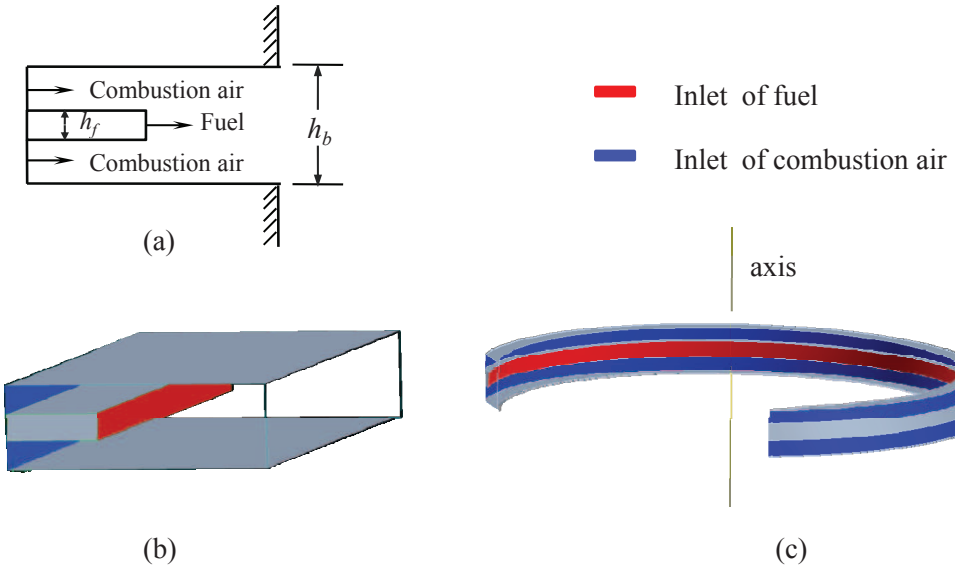

Figure 3.6: (a)The 2-D geometry of the diffusion burner,(b) the prototype the model representing in 2-D modeling, and (c) the prototype the model representing in 2-D axisymmetric modeling

Consequently, the challenge is that how to convert the dimension of a tubular burner into a slot properly so that the modeling is as representative as possible? Generally we can say, there are two basic approaches: (a) to remain the jet velocities of the fuel and the combustion air unchanged, and (b) to keep the hydraulic diameter constant. As the volumetric flow rates of the fuel and combustion air are fixed for given output of the kiln, the first approach can be put as that the inlet area of each stream in 2-D is equal to that in 3-D case. In 2-D axisymmetric modeling therefore, we have
horizontal burner:

$$2\pi r \cdot h_f = \pi \left(\frac{d_f}{2}\right)^2 \cdot n \tag{3.3}$$

vertical burner:

$$\pi \left(r + \frac{h_f}{2}\right)^2 - \pi \left(r - \frac{h_f}{2}\right)^2 = \pi \left(\frac{d_f}{2}\right)^2 \cdot n \tag{3.4}$$

where R is the inside diameter of the kiln, r is the distance between the centerline of the kiln and the burner outlet or the distance between the centerlines of the kiln and the burner in the case of vertical burner, and n is the number of burner.

The dimension of the fuel inlet thus can be obtained correspondingly as (for both cases)

$$h_f = \frac{n \cdot d_f^2}{8r} \tag{3.5}$$

Similarly, h_b can be calculated by

$$h_b = \frac{n \cdot d_b^2}{8r} \tag{3.6}$$

The disadvantage of this approach is that the hydraulic diameter of the burner is decreased dramatically, which changes the aerodynamic of the burner and leads to big challenge in the mesh design. For example, in the case of a kiln ($R = 1.5$ mm) with the firing system consisting of 12 peripheral burners ($r = R$,$d_f = 30$ mm), the dimension of the fuel inlet in 2-D model is calculated to be $h_f = 0.9mm$. Comparing the huge domain of the kiln, the tiny fuel inlet is too small to be meshed properly.

In the second approach, the inlet area of the fuel or the combustion air is much larger than that in tubular case, which implies that the velocity of both streams is decreased considerably for given volumetric flow rate, and thus the momentum flux ratio between the jet flow and the cooling air (cross flow from the bottom of the kiln) is decreased. The influence of the changes in momentum flux ratio on the jet behavior will be studied in Chapter 5

3.2.3 Bed height

The bed height or the bed loading of particles is another important problem to address. As we know, the height of an industrial shaft kiln can be up to 30 meters. It′s obvious that modeling of the entire kiln is beyond the computer power. Fortunately, the flow in the cooling zone is simple and not our interest, and meanwhile the flow structure in the preheating zone is largely dependent on the radial gas distribution through the burning zone, i.e. the fluid phenomena in the burning zone plays the dominant role. The computational domain therefore can be simplified to one zone, the burning zone. The question is whether the phenomena, especially the behavior of the burner injection in this zone, are independent on the height of preheating zone or not? If yes, what bed height (or what number of particles) is at minimum needed? The effect of the particle number on the flow through a packed bed with a certain tube-to-particle diameter ratio was studied by Calis et al. [25]. The results show that each subsequent particle represents a new entrance

region, i.e. the first particle is not different from the subsequent particles. The flow appears to be periodical right from the first particle onwards. The influence of the number of particles on radial jet behavior will be investigated in the chapter 5 of this work. The result shows that the jet expands fully into the bed after 3 to 4 particle layers above, and then the behavior becomes stable. That is to say, 4 or 5 particle layers above the burners are enough to model the flow structure in the burning zone, other details see chapter 5.

3.2.4 The basic 2-D geometric model

Based on the simplifications and assumptions presented above, the 2-D geometric model is created. As shown in Fig. 3.7, the basic geometry consists of a half perpendicular plane of the bed ($R = 1.0m$), subtracted by circles ($d_p = 100mm$) corresponding to the packed particles, and a peripheral slot-shaped nozzle. The overall void fraction of the bed is 0.4. The wall was subtracted by particles to avoid the occurrence of channeling.

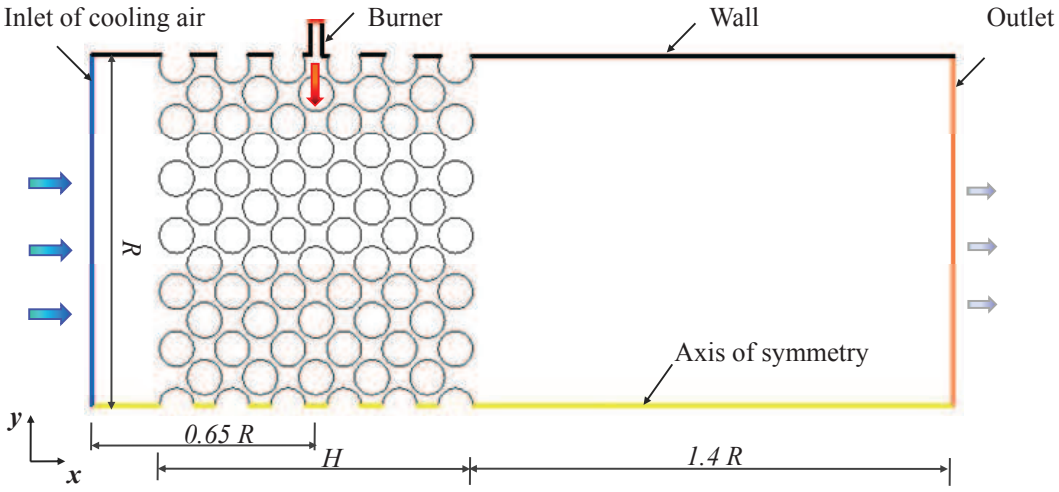

Figure 3.7: 2-D geometry schematic of the shaft kiln with horizontal burner

In Fig. 3.7, R is the radius of the kiln and, H is the bed height or loading height.

3.3 3-D Geometric model development

Geometry of the burner in 3-D has been mentioned in section 3.2.2 (Fig.3.5), and the bed height definition described above is applicable to 3-D modeling. Thus, only the particle arrangement of 3-D geometry is discussed in the following section.

3.3.1 Particle arrangement

For regular packing, the packed arrangements are determined by three basic types of sphere cluster which are similar to the arrangement of atoms in ideal crystals. According to the spatial structure of each sphere cluster, they are named octa-based arrangement, hexa-based arrangement, and tetra-based arrangement respectively.

Hexa-based arrangement. A hexa-based sphere cluster, corresponding to the *Simple Cubic* (SC) unit cell of crystal lattice structure is formed by eight spheres with centers at the apexes of a cube, shown in Fig.3.8. A packing, constructed by this arrangement, has a very simple structure and can be easily created. However, it's not practical as channeling problem tends to occur with this geometry, which can lead to a non-representative flow pattern. The void fraction of this arrangement is about 0.48.

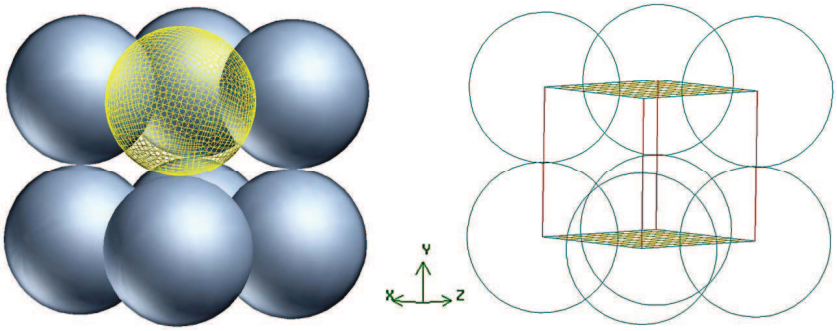

Figure 3.8: A hexa-based sphere cluster

Octa-based arrangement. Fig.3.9 depicts an octa-based sphere cluster, which is constituted by six spheres with centers at the apexes of an octahedron. This

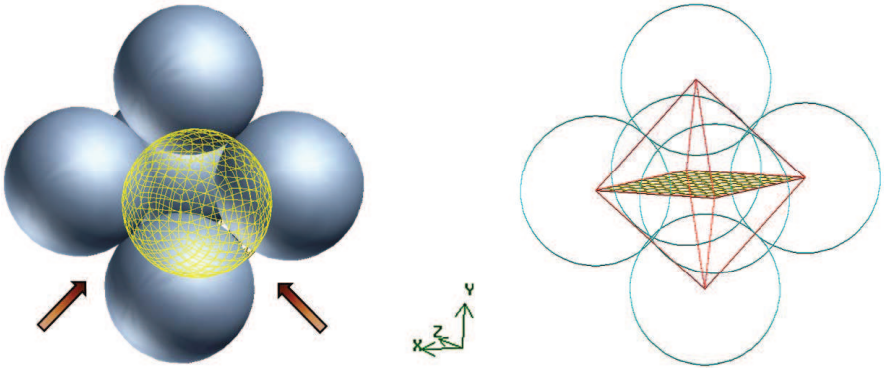

Figure 3.9: A octa-based sphere cluster

arrangement is similar to the *Body Centered Cubic* (BCC) crystal structure. For the primitive BCC structure, the packing efficiency is 68%, while for the closest structure, i.e. the corner particles on the middle face touch one another, the packing efficiency is 74%. Comparing with the hexa-space configuration, this structure is relatively compact and more sensible for modeling. But channeling problem cannot

be avoided if more than one streams are involved and flowing in certain directions which is indicated by the arrows in Fig.3.9. For normal shaft kilns, as being known, there is cooling air flowing axially from the bottom to the top and concurrently radial fuel injections from circumference. Therefore, this packed arrangement is not practical as well.

Tetra-based arrangement. Apparently, a tetra-based structure consists of four particles with centers at the apexes of a tetrahedron. Fig.3.10 shows a single tetra-based sphere cluster, a close *Face Centered Cubic* (FCC) unit cell. Comparing with the other arrangements, this configuration is more spatially stable. Besides, channeling problem can be prevented by properly stacking the clusters, which gives this arrangement a big advantage. However, the densely structure also leads to a low void fraction, about 0.26. Given that that the normal porosity of the packed material in shaft kilns is around 0.4, the particle is shrunk to a certain extent to get a bigger void fraction. Consequently, there are no real "contacts" between particles in the model, and of course this will influence the flow pattern somewhat especially on the heat transfer mechanism. When heat transfer is considered in modeling, the geometrical arrangement should be carefully designed.

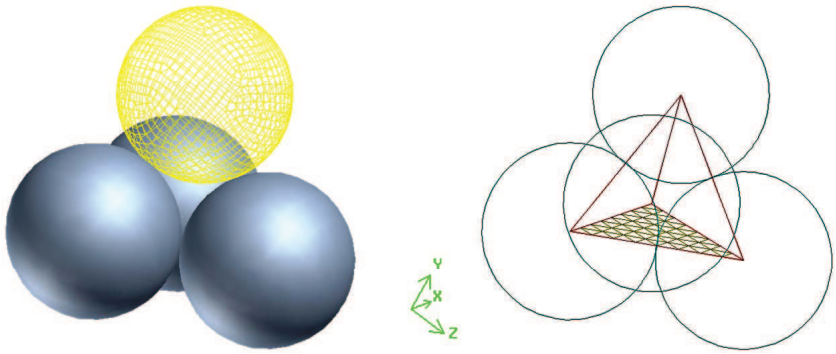

Figure 3.10: A tetra-based sphere cluster

3.3.2 The wall segment strategy

Even though the particles are simplified to spheres and the bed height is considered as short as possible, to simulate a full bed on industrial scale is still a huge challenge. As reviewed in Chapter 2, a wall segment strategy is employed to reduce the computational time. In this way, the full geometry is represented by a segment with certain degree by taking advantage of flow symmetry.

3.3.3 The basic 3-D geometric model

By using the wall segment strategy, the size of the 3-D geometry is reduced drastically. Of course, the degree of the angle depends on how many burners the shaft kiln has and how the burners are geometrically situated. Given a shaft kiln with 12 burners for example, if all burners are positioned horizontally and put into

the kiln at the same lance depth, the geometry angle would be 30 degree. The schematic of such a shaft kiln is depicted in Fig. 3.11. Fig. 3.12 illustrates the corresponding 3-D geometric model which is a 30^o segment consisting of 9 layer of particles.

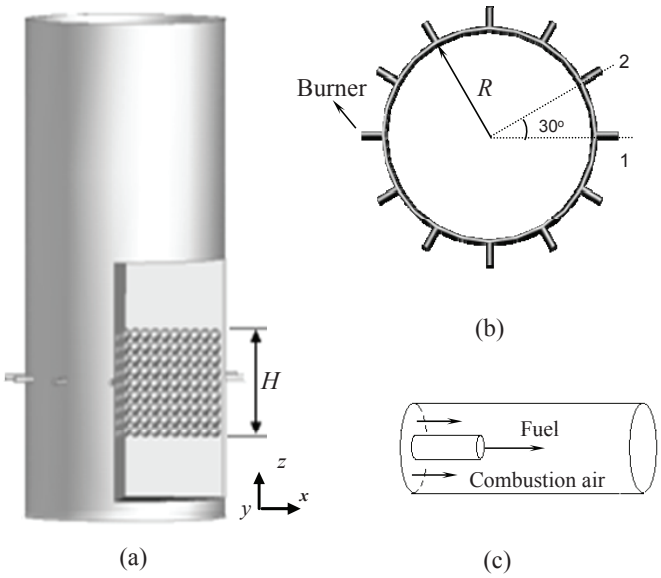

Figure 3.11: Schematic of a shaft kiln (main body) with 12 horizontal diffusion burners: (a) the side view, (b) the top view, and (c) the simplified diffusion burner

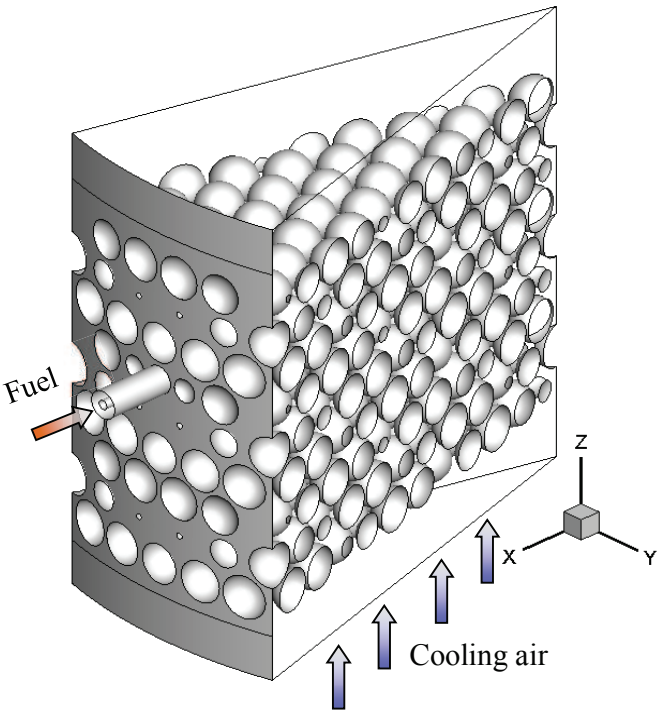

Figure 3.12: The 30^o WS 3-D Geometry

3.4 Summary

The geometric models for CFD flow simulation of shaft kilns were developed in this chapter. Regarding that the geometry of a shaft kiln and the process occurring in it are complicated, some simplifications were made firstly. The main components of the model, such as the particle arrangement, the burner, and the bed height etc. were discussed in detail, respectively. 2-D modeling has great advantage in reducing the computational time, but the deficits are 'remarkable' as well. The treatments on the particle arrangement and the burner in 2-D modeling were specified. Finally, the basic geometric models for 2-D and 3-D simulation were presented.

Chapter 4

Grid Design and Grid Convergence Studies

The computational grid or mesh represents the geometry of the region of interest. The computational domain needs to be discretized using grid cells that should provide an adequate resolution of the geometric and expected flow features. The accuracy of the simulation usually increases with increasing number of cells, i.e. with decreasing cell size. However, due to limitations imposed by the increased computer storage and run-time some compromise in mesh size is nearly always inevitable [47]. In this chapter, the gridding strategy and the methods of checking the discretization error are going to be discussed, and the grid convergence studies will be carried out to determine the proper grid densities for 2-D and 3-D simulation.

4.1 Discretization error and its estimation

4.1.1 Discretization error

Several various possible spatial discretizations have been introduced in Chapter 2. Within the finite-volume methodology, for example, the surface integral in the Navier-Stokes equations is approximated for each control volume by some appropriate method. The approximation of the convective and viscous fluxes across the boundaries of the control volume means that the discretized equations differ from the the governing equations, which we seek to solve. This difference causes a certain spatial *discretization error* [48]. The error is influenced by the numerical scheme applied for the evaluation of the integrals and by the resolution of the discretization. Therefore, the grid convergence study or model verification is quite necessary especially in the case that experimental data is not available.

In general, the discretization error can be estimated by two methods,

- General mesh refinement study. This approach is used when the theoretical value (exact solution) of the key parameter is available. The users of

CFD codes just need to refine the grids till the computed results meet the theoretical value or achieve a certain accuracy.

- Grid convergence index (GCI) method. This approach is based on a grid refinement error estimator derived from the theory of the generalized Richardson Extrapolation [49]. It is often used for the quantification of numerical uncertainty. The details of this method is described in the following section.

4.1.2 Grid convergence index (GCI)

The GCI is a measure of the percentage that the computed value is away from the asymptotic numerical value. It indicates an error band on how much the solution would change with a further refinement of the grid. A small value of GCI indicates that the computation is within the asymptotic range.

The grid convergence index can be computed using two levels of grid; however, three levels are recommended in order to accurately estimate the order of convergence and to check the solutions that are within the asymptotic range of convergence [50].

If there are three levels of grid, and f_1, f_2 and f_3 are the numerical solutions they yield respectively, the estimated value of the exact solution can be obtained by using Richardson extrapolation,

$$f_{ext} = f_1 + \frac{f_1 - f_2}{\gamma_{21}^p - 1} \tag{4.1}$$

where index 1 denotes the finest grid and index 3 the coarsest grid, γ_{21} is the grid refinement ratio.

The GCI on the fine grid is defined as

$$GCI_{fine} = \frac{F_s \left|\phi\right|}{(\gamma_{21}^p - 1)} \tag{4.2}$$

where F_s is a factor of safety, recommended to be F_s=3.0 for comparisons of two grids and F_s=1.25 for comparisons over three or more grids, and ϕ is the relative error, defined as

$$\phi = \frac{f_2 - f_1}{f_1} \tag{4.3}$$

The accuracy order,p, in Eq. 4.1 and Eq. 4.2 is connected to its truncation error which equals to the difference between the scheme and the exact formulation based on a Taylor expansion series. The first order scheme is likely to be more

robust, but it may yield less accurate solutions on a fine grid comparing with the higher order schemes. It should, however, be borne in mind that the order of a method has no direct connection to the accuracy of a solution on a given gird. For instance lower order upwind methods can yield better solutions on coarse grids than higher order schemes, while the higher order central schemes will approach the exact solution faster when the grid is refined. Usually, a first order scheme is not at all suitable for general large engineering applications involving complex flows with large gradients and thin boundary layers. The large truncation error introduced by the first order scheme is known as numerical viscosity or diffusivity as it gives rise to artificial diffusion fluxes. To assess the truncation error in practice, Roache [51] suggests some possible ways:

- Additional solution(s) on different grid(s) - grid refinement or coarsening, unrelated grid(s);
- Additional solution(s) on the same grid - higher- or lower-order accurate discretization;
- Solution of an auxiliary partial-differential equation on the same grid;
- Algebraic evaluation on the same grid.

The most common approach is to solve the governing equations on a series of grids with different cell sizes. When the grid refinement ratio is constant or from the generalized expressions, the order of accuracy can be estimated from,

$$p = ln\left(\frac{f_3 - f_2}{f_2 - f_1}\right) / ln\left(\gamma\right) \tag{4.4}$$

or from the generalized expressions

$$p = \frac{1}{ln\left(\gamma_{21}\right)} \left| ln\left|\frac{f_3 - f_2}{f_2 - f_1}\right| + q\left(p\right)\right| \tag{4.5}$$

$$q\left(p\right) = ln\left(\frac{\gamma_{21}^p - s}{\gamma_{32}^p - s}\right) \tag{4.6}$$

$$s = 1 \cdot sign\left(\frac{f_3 - f_2}{f_2 - f_1}\right) \tag{4.7}$$

It is important that each grid level yield solutions that are in the asymptotic range of convergence for the computed solution. This can be checked by observing two GCI values as computed over three grids,

$$GCI_{23} = \gamma^p GCI_{12} \tag{4.8}$$

If a desired accuracy level is known and results from the grid resolution study are available, one can then estimate the grid resolution required to obtain the desired level of accuracy,

$$\gamma^* = \left(\frac{GCI^*}{CCI_{23}}\right)^{1/p} \tag{4.9}$$

4.1.3 The key variables

To check the convergence of each grid, the critically important variables to the objective of the simulation should be selected. As the main objective of this work is to study the radial gas mixing in the shaft kilns, velocity of the fluid is fairly critical to the simulation. Therefore, velocity is selected to be one of the key variable. Meanwhile, pressure drop is also considered for the sake of further study in geometry development. In tube banks, the flow is dominated by the maximum velocity that occurs within the tubes, whilst in a packed bed it is characterized by the interstitial velocity. Therefore, the simulations are carried out to determine the values of the maximum velocity in 2-D modeling and the interstitial velocity in 3-D modeling.

As we know, the maximum velocity occurs in the minimum flow area of tube banks. It can be exactly calculated for given transverse and longitudinal pitches. The details of a staggered tube bank is illustrated in Fig. 3.3 in Chapter 3.

If $S_D \geq (S_T + \mathrm{d})/2$, it can be found from

$$v_{max} = \frac{S_T}{S_T - d} U \tag{4.10}$$

where S_T is the transverse pitch, and U is the superficial velocity.

Otherwise, the maximum velocity will occur at the diagonal cross section and can be calculated as

$$v_{max} = \frac{S_T}{2\left(S_D - d\right)} U \tag{4.11}$$

where S_D is the diagonal pitch, determined from

$$S_D = \sqrt{S_L^2 + \left(S_T/2\right)^2} \tag{4.12}$$

where S_L is the longitudinal pitch.

The Reynolds number is defined as

$$Re_D = \frac{\rho v_{max} d}{\mu} \tag{4.13}$$

where, d is the diameter of the tube.

For flow in the porous medium, the interstitial velocity is defined as

$$v_i = \frac{U}{\varphi} \tag{4.14}$$

where φ is the void fraction of the packing.

However, as the interstitial velocity is the average velocity that prevails in the pores of the packed bed, it is not so practical to locate the position and to find the corresponding computed value. Therefore, the average velocity through the minimum cross-section is used instead to check the grid convergence trend.

The pressure drop across tube banks can be found form the Zukauskas equation [7],

$$\Delta P = N_L \chi \left(\frac{\rho v_{max}^2}{2} \right) f \tag{4.15}$$

where N_L represents the number of tube rows counted in the flow direction; the friction factor f and the correction factor χ are determined from the Fig. 4.1.

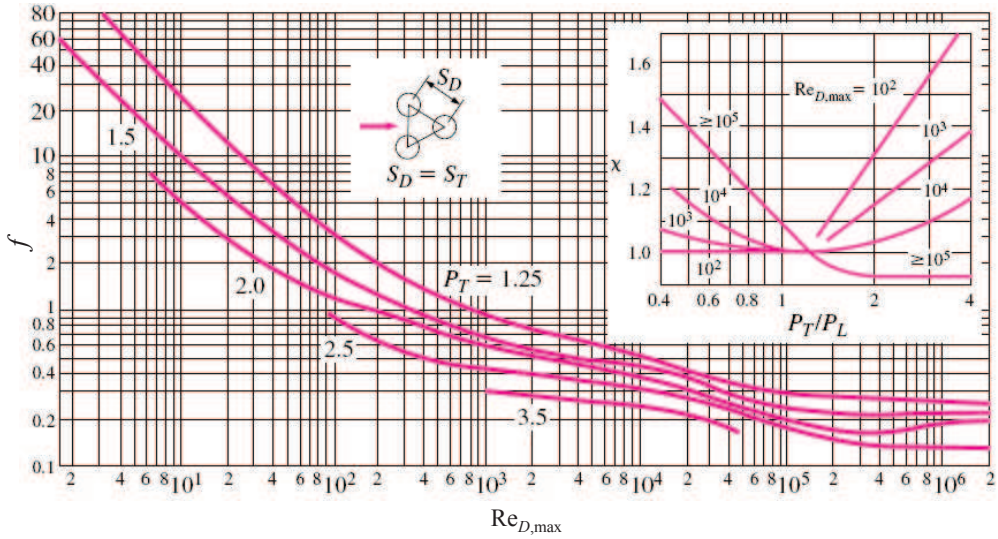

Figure 4.1: The friction and correction factors for staggered tube banks [7]

In the Fig. 4.1, P_T and P_L are the dimensionless transverse and longitudinal pitches, defined as P_T=S_T/d and P_L=S_L/d, respectively.

The pressure drop in the packed bed can be predicted by Ergun equation [52],

$$\frac{\Delta P}{L} = 150 \cdot \frac{(1-\varphi)^2}{\varphi^3} \cdot \frac{\mu \cdot U}{\overline{d_p}^2} + 1.75 \cdot \frac{1-\varphi}{\varphi^3} \cdot \frac{\rho \cdot U^2}{\overline{d_p}} \tag{4.16}$$

where L and φ are the height and void fraction of the bed respectively. U is the fluid superficial velocity and, $\overline{d_p}$ is the characteristic diameter, Sauter-diameter, defined as,

$$\overline{d_p} = \left[\sum_{i=1}^{n} \left(\frac{V_i}{V} \cdot \frac{1}{d_{pi}} \right) \right]^{-1} \tag{4.17}$$

For the pressure drop in packed bed with spherical particles, exists the equation obtained by Brauer [53],

$$\frac{\Delta P}{L} = 160 \cdot \frac{(1-\varphi)^2}{\varphi^3} \cdot \frac{\mu \cdot U}{{d_p}^2} + 3.1 \cdot \frac{1-\varphi}{\varphi^3} \cdot \frac{\rho \cdot U^2}{{d_p}^2} \cdot \left[\frac{\mu \cdot (1-\varphi)}{\rho \cdot U \cdot d_p} \right]^{0.1} \tag{4.18}$$

Brauer′s correlation is based on experimental data and applies to a packed bed consisting of spherical particles of the same diameter. In this case, the Sauter-diameter is equal to the sphere diameter. Considering that the 3-D geometric model in this work also consists of spherical particles of the same diameter, Brauer′s equation is applied to calculate the pressure drop.

By comparing with the simulation output, the results calculated by Eq. 4.15 and Eq. 4.18 are used to check the grid convergence trend on pressure drop.

4.2 Gridding strategy and model reduction

4.2.1 Gridding strategy

As we discussed at Chapter 2, to discretize the computational domain we can choose between structured, unstructured, and hybrid grids. The decision depends not only on their specific advantages and shortcomings but the geometry of the domain.

In this work, according to the geometric characters the computational domain of the model can be regarded as consisting of 4 domains: burner(s), outlet, inlet, and packing, as shown in Fig. 4.2. The burner(s), and the outlet and inlet domains are in the shape of a square in 2-D and a straight tube in 3-D, and therefore they are subdivided by structured quadrilaterals and prisms (unstructured). The packing domain is filled with particles which leads to complex geometric structure, and unstructured triangles and tetrahedra are used accordingly. It is worth noting

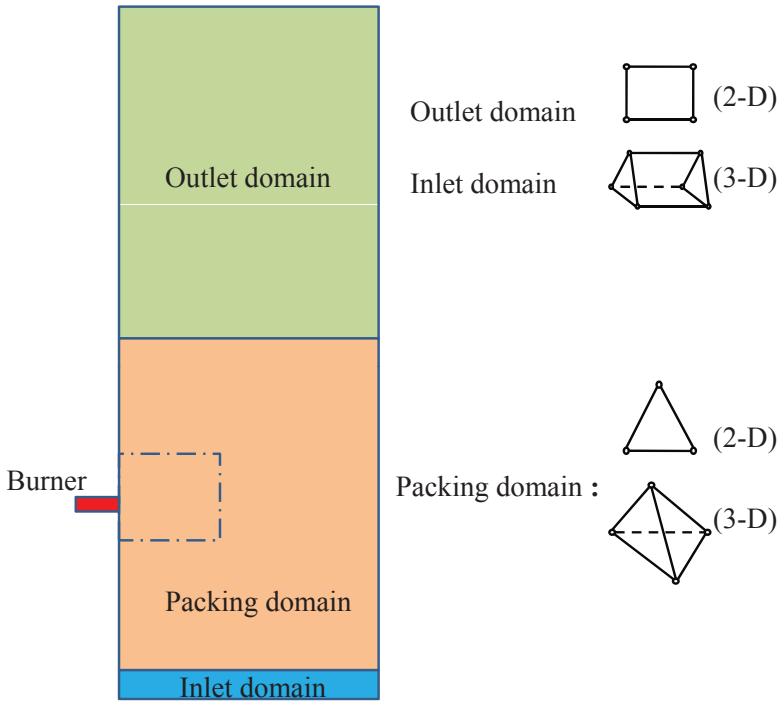

Figure 4.2: The scheme of computational domains and sub-domains for gridding

that hexahedra can not be used for the other domains as the packing domain is subdivided by tetrahedra.

In 2-D modeling, hybrid grid is used to build the mesh in the packing domain. A structured boundary layer is created around the surface of each tube (circle), while the unstructured triangles are used for rest of the domain. The structure of the grid can be seen in the following section (Fig. 4.5-4.7).

4.2.2 Model reduction

As described above, a grid convergence study normally involves performing the calculation on three successively finer grids. This may result in a big problem to carry on the grid convergence study in this project due to the large and complex geometry of the shaft kiln. Refining a mesh by a factor of 2, for example, can lead to an 8 fold increase in problem size (4 fold in the case of 2-D modeling) and thereby more time and computer power are required or even unacceptable for the available resource. To reduce the computational efforts, the grid convergence studies are carried out with “unit models”, which represent the basic packing structure of 2-D and 3-D models . While considering the jet flow of the burner(s), specially finer grid is created in the near-burner area which is highlighted in a square frame shown in Fig. 4.2. The detailed unit models used for the study are presented in the following sections.

4.3 Grid convergence study of 2-D model

4.3.1 *Unit model* description

As explained in the Chapter 3, the 2-D geometric model is actually a 2-D section of a tube bank. If the firing system is not considered, the problem can be simplified as flow across a tube bank. A schematic of the problem is shown in Fig. 4.3. The bank consists of regularly spaced tubes with a diameter of 50 mm, which are staggered across the cross-fluid flow. Their centers are separated by a distance of 81 mm in the x direction (S_L), and 162 mm in the y direction (S_T). The default depth of the bank is 1 m.

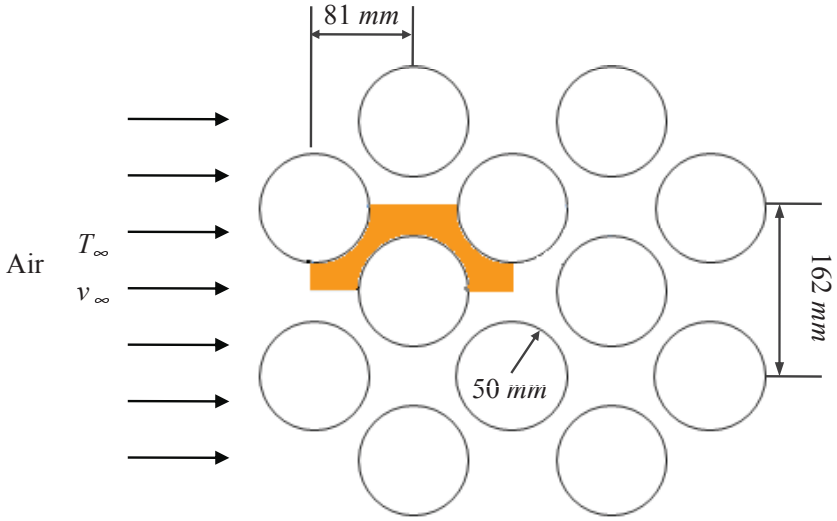

Figure 4.3: A schematic of the tube-bank geometric model

Apparently, the fluid domain is made up of many a "unit cell", the orange area shown in Fig. 4.3. Therefore, only this portion of the domain needs to be modeled. The computational domain used for 2-D grid convergence study is depicted in Fig. 4.4.

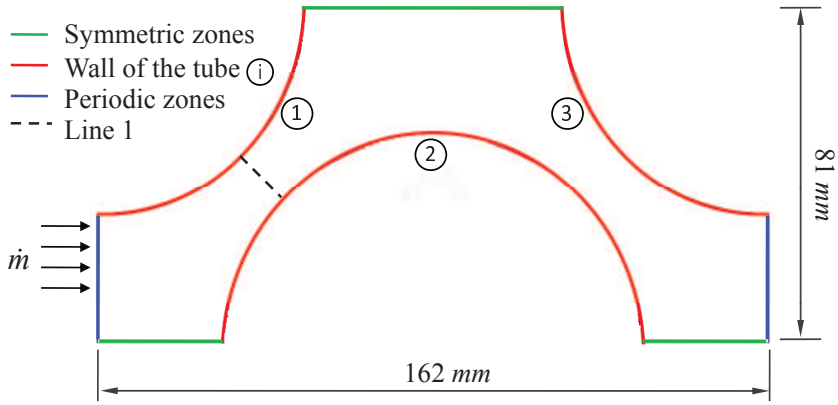

Figure 4.4: The unit model and the boundary definition

In Fig. 4.4, the Line 1 indicates the minimum cross sectional area of the bank

where the maximum velocity occurs. A mass flow rate of $\dot{m}$ is applied to the inlet boundary of the periodic module.

4.3.2 Material properties , operating conditions and solution control

Air is used as the cross flow. As the process is adiabatic, the properties of air at 288.15 K are applied. The mass flow rate of air is calculated from a superficial velocity of 0.5 m/s which is the normal superficial velocity of "cold flow" in lime shaft kilns. The properties of air and the operating conditions are shown in Table 4.1.

Table 4.1: The properties of air and the operating conditions

ρ $[kg/m^3]$	μ $[kg/m \cdot s]$	$\dot{m}$ $[kg/s]$	P $[Pa]$	T $[K]$
1.229	1.73×10^{-5}	0.05	101325	288.15

The relaxation factors for each transport variables are shown in Table 4.2.

Table 4.2: Under-relaxation factors for the computing variables

Pressure	Density	Body forces	Momentum	κ	ϵ	Turbulent viscosity
0.3	1	1	0.7	0.8	0.8	1

As the solution is converging at an extremely fast rate due to the small unit model, the convergence criterion for continuity is set to 10^{-4}. The default value 10^{-3} is defined for the rest variables.

4.3.3 Grids

For air across the tube bank, the wall of the tube has great impact on the turbulence of the fluid. Considering that the gaps between two neighbor rows of tubes are very small (about 14.5 mm for a given void fraction of 0.4), and flow separation occurs, the enhanced wall treatment is used instead of the standard wall function. Therefore, a fine resolution in the near-wall region is necessary. A boundary layer is built to meet the requirement. The thickness of the first cell is calculated based on the Reynolds number and desired y^+ value ($y^+ \approx 1$). The details that how the wall affects the turbulence modeling, and the difference between the enhanced wall treatment and the standard wall function are presented in Chapter 2.

In this case, the dimension of the geometry and the spacing (d_s) to the wall to yield the first grid in the laminar sublayer are shown in Table 4.3. d_s is estimated by a viscous grid spacing calculator [54].

Table 4.3: Estimation of the wall distance to yield the first grid

S_T $[mm]$	S_L $[mm]$	S_D $[mm]$	$\dot{m}$ $[kg/s]$	v_{max} $[m/s]$	Re_D -	d_s mm
162	81	114.5	0.05	2.80	1.98×10^4	0.1

Accordingly, three significantly different set of grids are built. Table 4.4 lists the details of all grids, and the structure of each grid is displayed in Fig. 4.5 to 4.7.

Table 4.4: The grids used for grid convergence study (2-D)

Grid	Boundary layer		Interval size $[mm]$	Cells	Grid density [cells/cm^2]
	Growth factor	Rows			
1	1.35	8	1.4	6416	121.8
2	1.6	7	2.5	2165	41.1
3	2.0	5	5	705	13.4

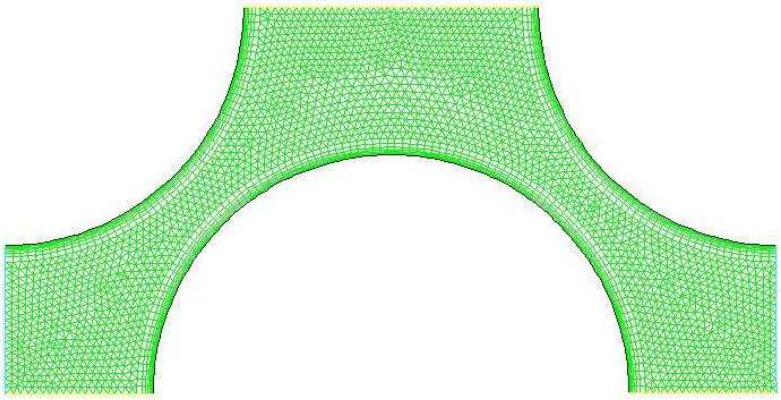

Figure 4.5: The finest mesh (Grid 1)

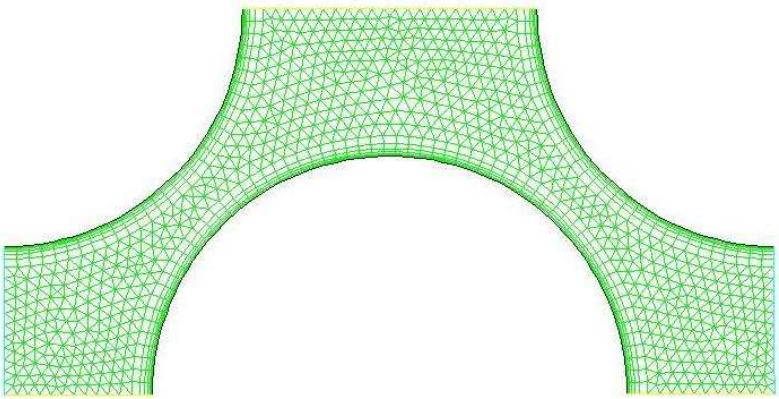

Figure 4.6: The medium mesh (Grid 2)

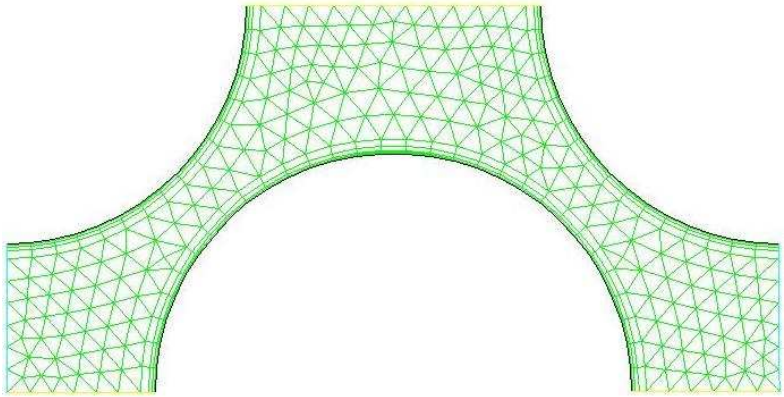

Figure 4.7: The finest mesh (Grid 3)

4.3.4 Computation and analysis

Wall Yplus

According to the guidelines presented in FLUENT documentation, the value of y^+ should be approximately equal to 1 or at least less than 4$\sim$ 5 when enhanced wall treatment is used. The values of y^+ with respect to different grids are plotted in Fig. 4.8. It is clear that the values are quite low and meet the requirement.

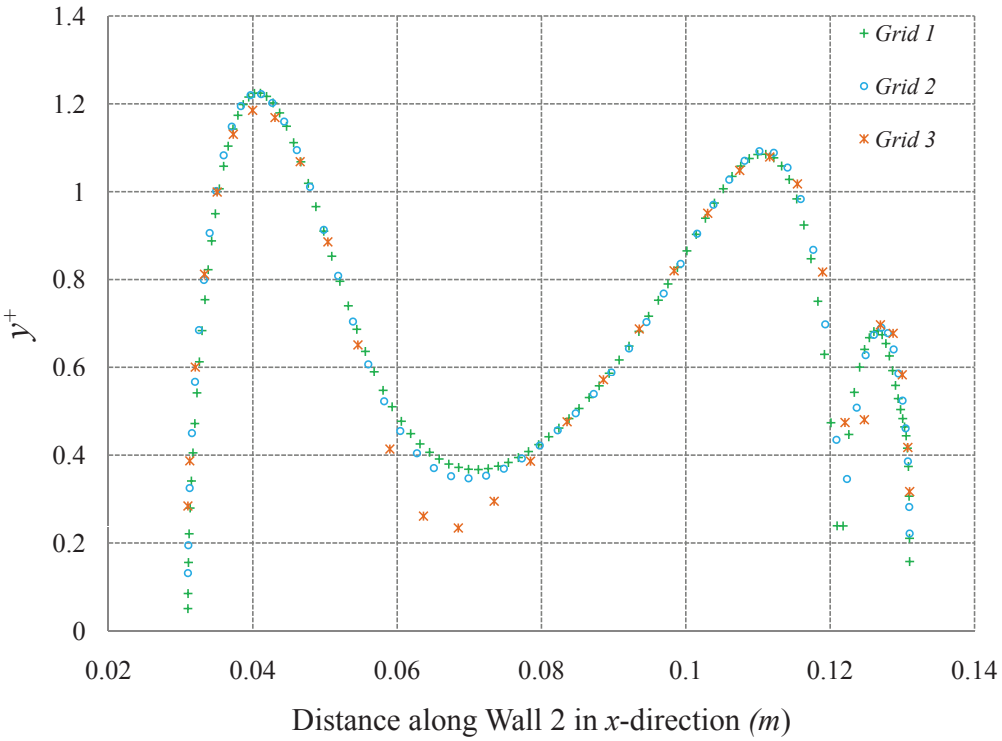

Figure 4.8: y^+ plots in each case

The maximum velocity and the pressure drop

Table 4.5 presents the theoretical value (exact solution) of v_{max} calculated by Eq. 4.11, the empirical value of ΔP obtained from Eq. 4.15, and their computed results upon each grid. The number of iterations and the computational time are also listed.

Table 4.5: Computational results upon the three levels of grid

Grid	Velocity $[m/s]$		Pressure drop $[Pa/m]$		Iterations	CPU time
	v_{max}	$v_{max,comp}$	ΔP	ΔP_{comp}		[s]
1	2.79	2.79	17.0	20.30	322	35
2		2.80		20.96	166	15
3		2.79		23.50	64	5

In the Table 4.5, $v_{max,comp}$ is the average velocity over Line 1 which is shown in Fig. 4.4.

Apparently, v_{max} is independent on the grid and the computed values are in good agreement with the exact solution. Fig. 4.9 displays the velocity profiles along Line 1 in each case. The curves fit each other properly, which means that the coarsest grid density in the gap of tubes is sufficient for simulation.

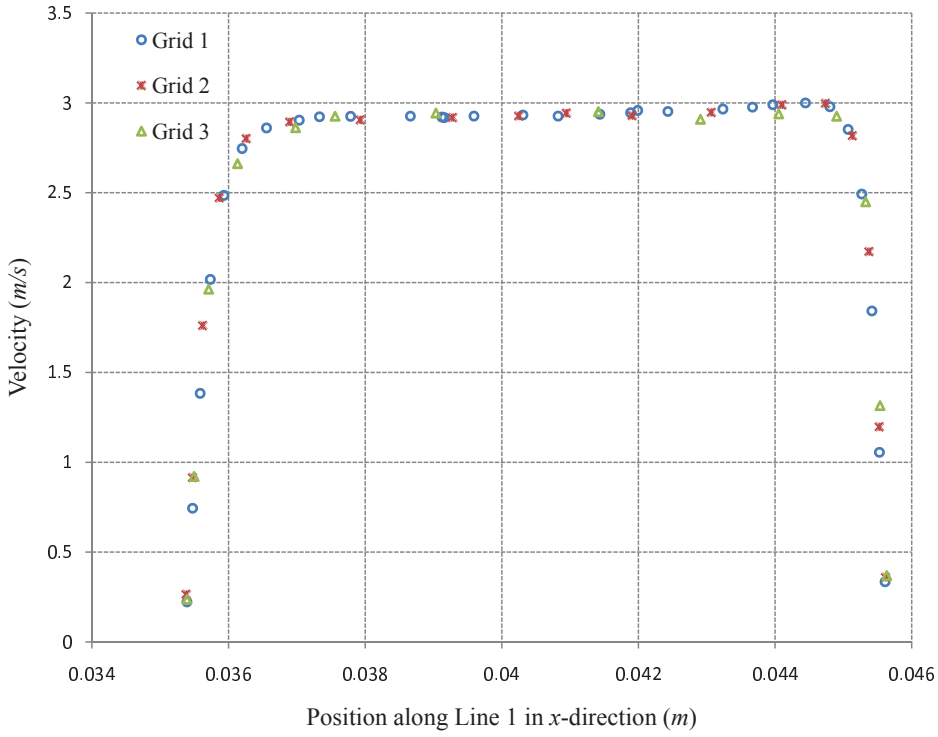

Figure 4.9: The velocity profiles along Line 1 on three sets of grid

The computation of the pressure drop, however, is influenced by the grid density. From Table 4.5, we can find that the coarser the grid is, the higher value

of the pressure drop that the simulation predicts. To find how the grid density affects pressure drop simulation, the velocity contours are displayed in Fig. 4.10 to 4.12, in which the contours are colored by velocity magnitude (m/s). From the comparison, we can find that with coarser grid the separation region or the wake behind the tube is under-predicted. This may over-predict the pressure drop caused by frictional force. The phenomenon is more easily to be observed in vector plots, as shown in Fig. 4.13.

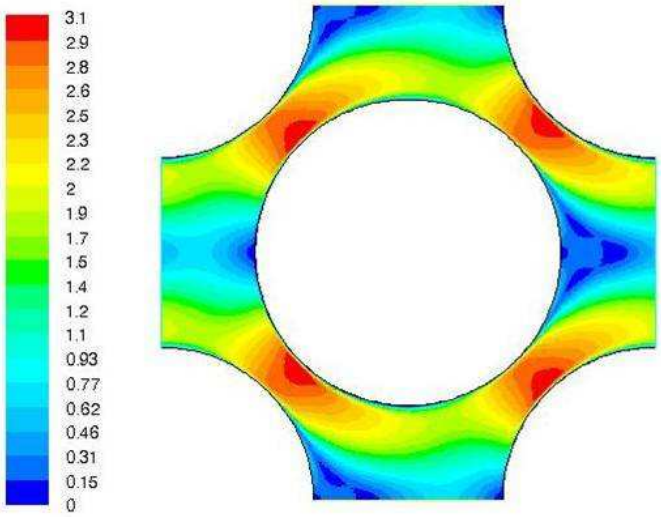

Figure 4.10: The velocity contours predicted on Grid 1 (fine grid)

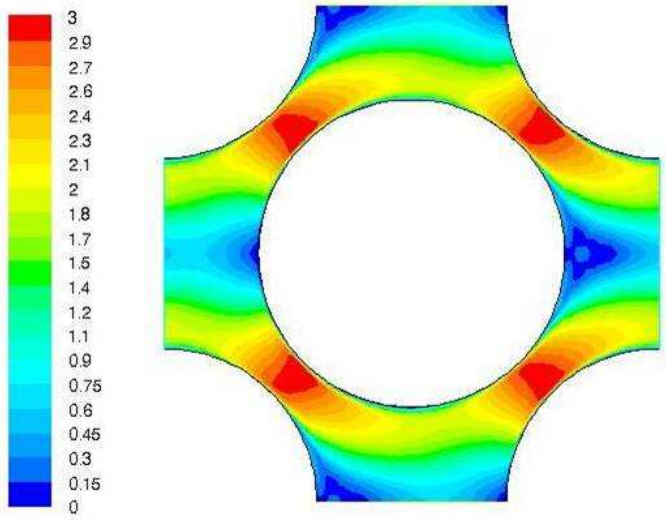

Figure 4.11: The velocity contours predicted on Grid 2 (medium grid)

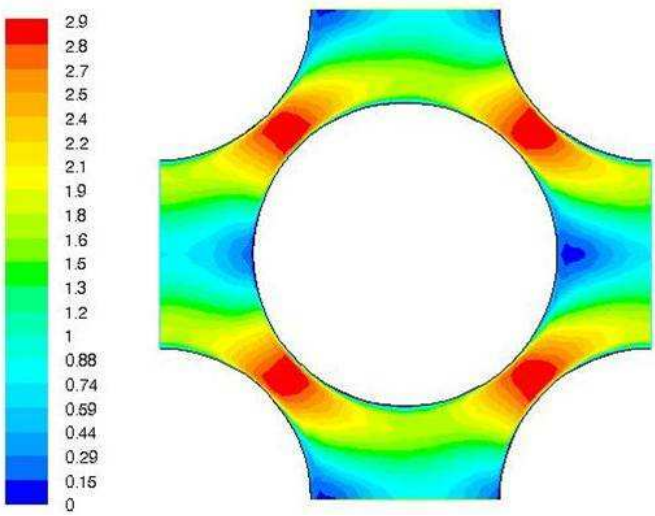

Figure 4.12: The velocity contours predicted on Grid 3 (coarse grid)

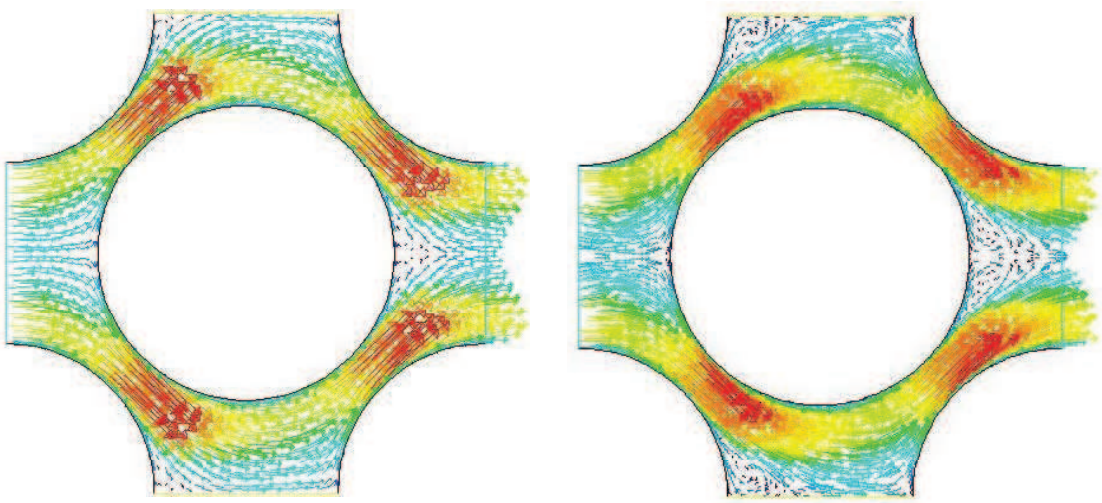

(a) (b)

Figure 4.13: The velocity vector plots: (a) on Grid 3 (coarse grid) and (b) on Grid 1 (fine grid)

Meanwhile, comparing the computed values and the pressure drop obtained by the Zukauskas correlation, we can find that the pressure drop predicted by the Zukauskas equation is lower. This may be explained by the periodic boundary condition which is set to the *unit model*. As being well known, the nature of flow around a tube in the first row resembles flow over a single tube. The nature of flow around a tube in the second and subsequent rows is very different because of wakes formed and the turbulence caused by the tubes upstream [55, 56]. A periodic condition indicates that the inlet effect is not considered in the simulations and thus leads to the higher pressure drop. Therefore, the value calculated from the Zukauskas correlation can not be regarded as one of the criteria on grid convergence in this case.

To check the grid convergence trend on the pressure drop, the extrapolated

value and the GCI for the grids are calculated based on Eq. 4.1 and Eq. 4.2. Table 4.6 shows the results.

Table 4.6: Calculation results based on the GCI method

γ	p	ΔP_{ext}	GCI_{12}	GCI_{23}
1.738	2.4	20.06	1.468%	4.88%

It can be noted that the GCI value of the finest grid is quite low. The computational time, however, is also quite longer comparing with that of the coarsest grid; and this may give rise to a big challenge when modeling an industrial-scale problem. In view of this, we can say Grid 3 is a reasonable compromise between the accuracy and the computational effort for the purpose of industrial engineering design.

The order of accuracy

According to the calculation shown in the Table 4.6, the accuracy order is as determined as 2. However, the computation above is performed with the first-order upwind scheme. To examine the influence of a higher order spatial accuracy, simulations are carried out with the second-order upwind scheme. Table 4.7 presents the results and the comparison.

Table 4.7: Comparison between the upwind schemes

Grid	Upwind scheme	$v_{max,comp}$ $[m/s]$	ΔP_{comp} $[Pa/m]$	Iterations	CPU time [Sec]
1	1^{st}	2.79	20.30	322	35
	2^{th}	2.79	20.71	483	58
2	1^{st}	2.79	20.96	166	15
	2^{th}	2.79	21.44	240	23
3	1^{st}	2.79	23.50	64	5
	2^{th}	2.75	21.47	138	13

The comparison shows that the results are quite similar except the computation on the coarsest grid. On this grid, the second order scheme gives a better prediction on the pressure drop whilst under predicts the maximum velocity. It can be said that the higher order schemes are not always superior, especially on coarse grid and computational cost is concerned.

4.4 Grid convergence study of 3-D model

4.4.1 *Unit model* description

The 3-D geometric model has been discussed in Chapter 3. The tetra-based sphere cluster is used as the basic structure of the particle arrangement. As men-

tioned, the porosity of such packing is around 0.26. To increase the porosity without changing the arrangement, the particles are shrunk by a certain degree of the diameter after the initial definition of the geometry. In the other words, the position of all particles in the geometric model are calculated based on a certain particle diameter d_p, but the particles actually defined in the CFD domain have a diameter of $\varphi \cdot d_p$, here φ is the shrinking factor which can be obtained once the wanted void fraction is given. For example, the void fraction can be increased to 0.4 when all particles are shrunk by a factor of 93.25%. As a result, the packing contains no points of contact.

In this work, particle diameter of 100 mm is considered. Particles are shrunk by a factor of 93.25% firstly to reach a void fraction of 0.4. Fig. 4.14 depicts a 4-layer arrangement, in which the *unit cell* of the structure, bounded by dotted lines, indicates the portion of the domain needs to be modeled. The compuational *unit model* is specified in Fig. 4.15.

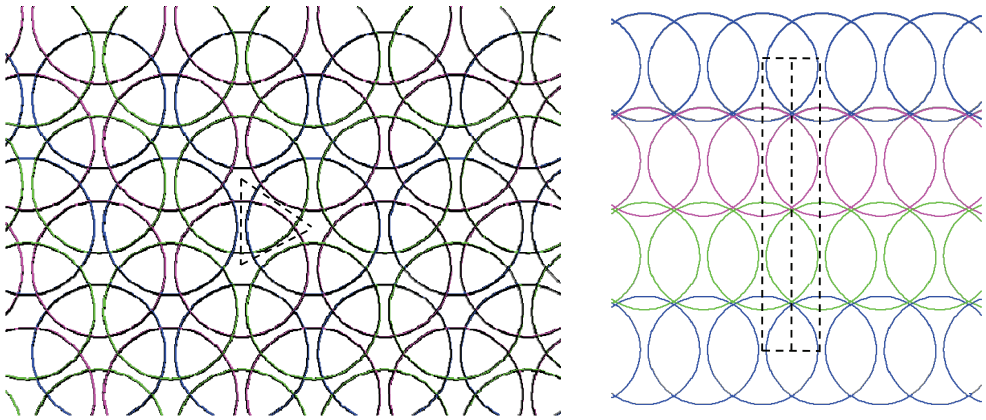

Figure 4.14: A 4-layer scheme of the 3-D packing: (a) z view, and (b) y view.

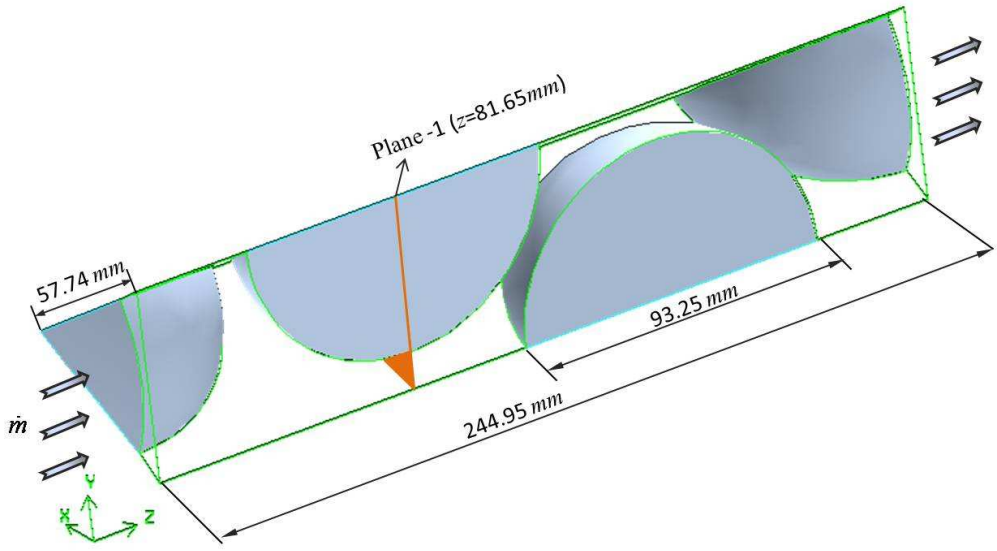

Figure 4.15: Schematic of the 3-D unit model

In Fig. 4.15, plane-1 shows the position at which the average maximum velocity ($\bar{v}_{max}$) is extracted.

4.4.2 Grids

In 3-D modeling, there is a great challenge in building the computational grid not because of the geometrical complexity but the large mesh density to reach the grid independence of the solution. Calis et al. [25] investigated the mesh density for the simulation of a packed bed containing 16 particles. The result shows that about three million cells are required for a grid-independent solution. For a 3-D geometric model of shaft kilns in which several hundred or even thousand of particles are involved, the computational size of the geometry is thus too large to be managed currently. For these considerations, the need of compromise between the computational cost and accuracy is apparent. Therefore, the standard wall function is used instead of the enhanced wall treatment to avoid a high resolution on the walls of particles; and the $y+$ criterion to the standard wall functions is not considered. In addition, as not all of the grids are within the asymptotic range of grid spacings, grid convergence index method is not used for this study. Instead, a series of grids, from the coarsest with mesh density of 23 cells/cm^3 to the extremely finest with mesh density of 2149 cells/cm^3, are used to give an extensive investigation on the grid convergence trend to find the optimal grid for the future and the optimal compromised grid for this work.

Table 4.8 presents the details of the grids used for simulation, and three grids representing the coarsest, the moderate, and the finest are displayed in Fig. 4.16 to 4.18.

Table 4.8: The grids used for grid convergence study (3-D)

Grid	Interval size [mm]	Cells	Skewness (>0.7) [%]	Grid density [cells/cm^3]
1	5	8045	0.25	23
2	4	15541	0.08	44
3	2.5	62328	0.12	176
4	2.0	112485	0.13	318
5	1.5	260870	0.15	738
6	1.25	424279	0.16	1200
7	1	760026	0.18	2149
8	0.8	1510584	0.19	4271

4.4.3 Material properties, operating conditions and solution control

Same as 2-D modeling, air at 288.15 K is used as the cross flow, and the process is adiabatic. For the superficial velocity of 0.5 m/s, the mass flow rate of

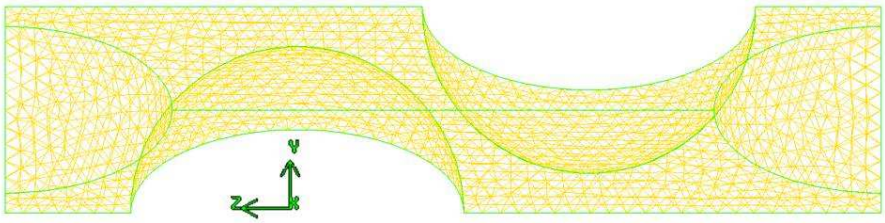

Figure 4.16: The coarsest mesh (Grid 1)

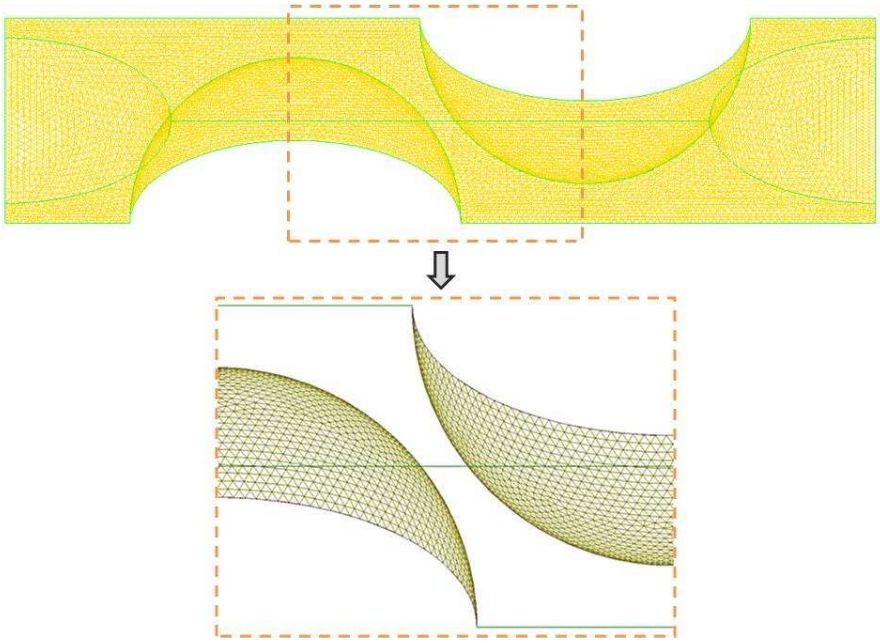

Figure 4.17: The medium mesh (Grid 4)

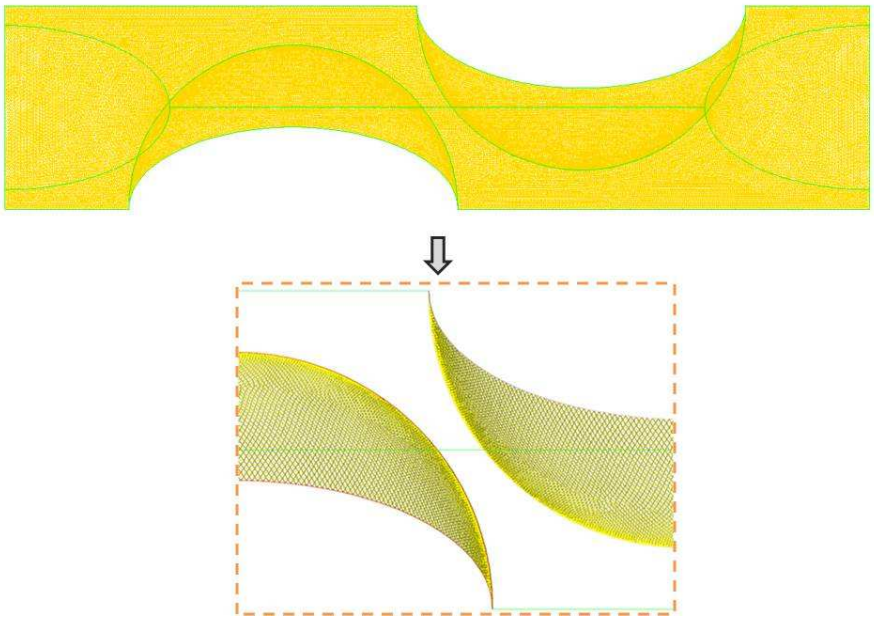

Figure 4.18: The finest mesh (Grid 8)

air passing the interstitial space of the periodic boundary is calculated as 0.00089 kg/s.

The relaxation factors for each transport variables are shown in Table 4.9.

Table 4.9: Under-relaxation factors for the computing variables

Pressure	Density	Body forces	Momentum	κ	ϵ	Turbulent viscosity
0.3	1	1	0.5	0.7	0.7	1

The iterative convergence is achieved with three orders of magnitude decrease in the residuals for each variable.

4.4.4 Computation and analysis

The theoretical flow velocity $\bar{v}$ through Plane-1, the empirical value of ΔP obtained from the Brauer′s correlation (Eq. 4.18) , and their corresponding computed results, $\bar{v}_{comp}$ and ΔP_{comp}, upon each grid are presented in Table 4.10. The results show that solution of the flow velocity becomes grid independent after two levels of refinement, while the prediction of the pressure drop varies drastically from the coarsest to the finest grid. In order to see the convergence trend more clearly, the resulting pressure drop is plotted as a function of the grid density, shown in Fig. 4.19.

Table 4.10: Computational results upon the three levels of grid

Grid	Velocity $[m/s]$		Pressure drop $[Pa/m]$		Iterations	CPU time
	$\bar{v}$	$\bar{v}_{comp}$	ΔP	ΔP_{comp}		[Min]
1	2.38	2.32	41.40	8.22	216	0.4
2		2.36		8.30	176	0.6
3		2.37		9.32	462	6
4		2.38		10.58	748	20
5		2.38		13.92	917	57
6		2.38		22.19	590	66
7		2.38		31.77	637	134
8		2.38		33.45	685	300

Fig. 4.19 illustrates a three-staged relationship. In the first, the pressure drop is under-estimated dramatically and is independent on the grid density, which can be noticed with the slight increases within a large variation in the grid density, from about 20 cells/cm^3 to 700 cells/cm^3. In the second, pressure drop changes sharply with the refinement of the grid into extremely high density. And the last, it becomes independent again. This observation indicates that there must be a factor which dominates the pressure drop and is poorly predicted by the simulation with coarse grids.

As known, the drag coefficient of a complete structure includes the effects of skin friction, the form drag and the interference drag. Interference drag arises

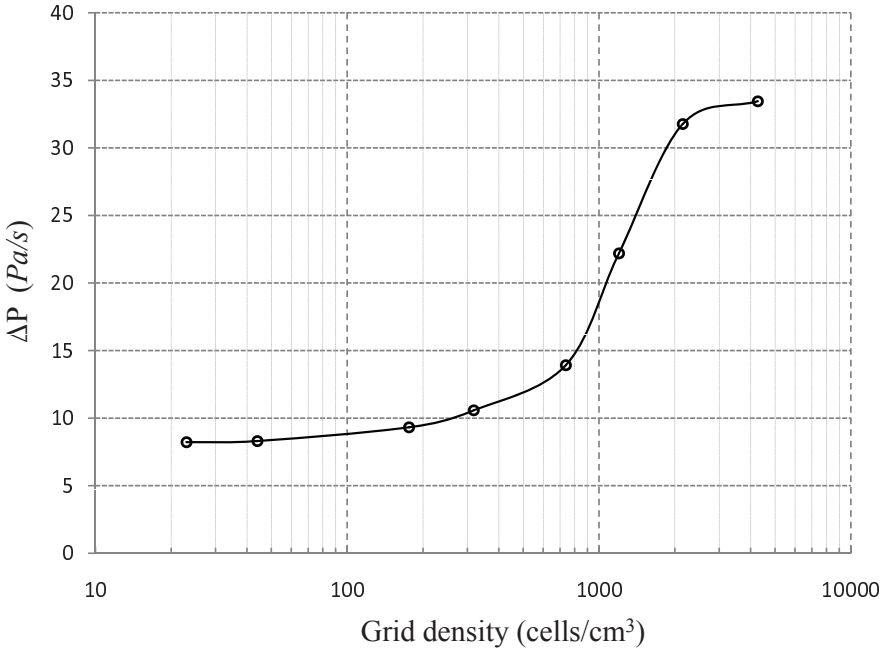

Figure 4.19: Dependence of the simulated pressure drop as a function of the grid density

from vortices and plays an significant role in aerodynamic resistance. And it has been observed by many researchers that the flow in the packed bed has a tendency to form vortices [25, 32]. Hence does the great change in pressure drop indicate the formation of the vortices? Fig. 4.20 to 4.22 present the evidence. Obviously, vortices are formed when the grid is fine enough. Fig. 4.21 shows the transient state and explains the dramatic change in pressure drop shown in Fig. 4.19. Compared with Brauer's correlation, FLUENT under predicts the pressure drop even with extremely fine grid. As the CFD modeling of pressure drop in structured packed bed had been experimentally validated by many researchers [25], the deviation in our case may be explained by the specific big gaps between particles.

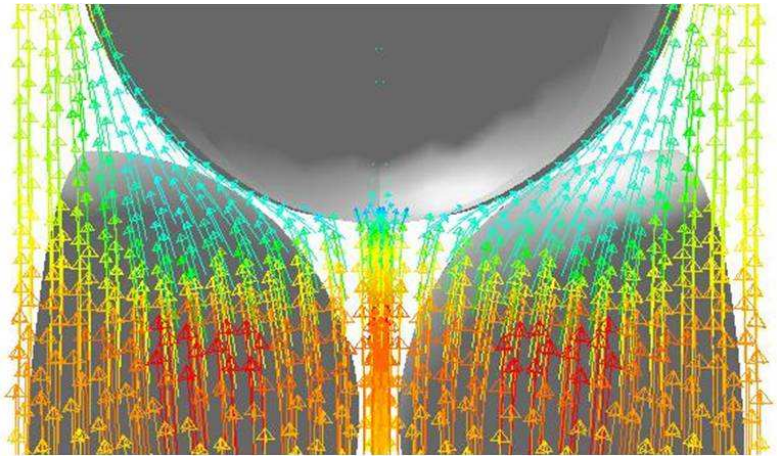

Figure 4.20: Velocity vector map of the simulation on the Grid 1 (23 cells/cm^3), colored by velocity magnitude in m/s

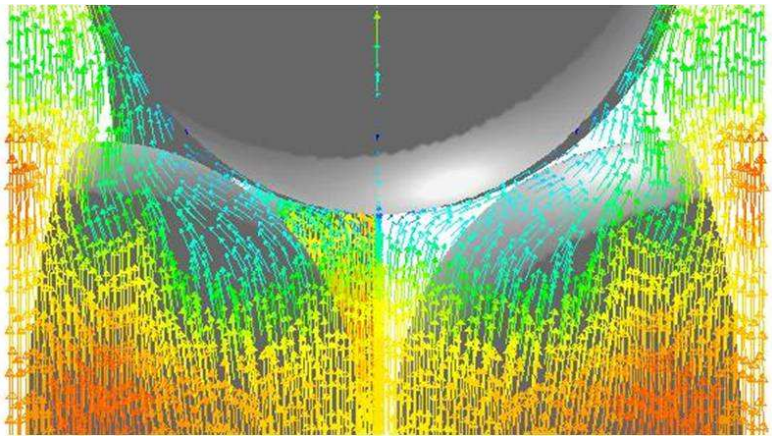

Figure 4.21: Velocity vector map of the simulation on the Grid 6 (1200 cells/cm^3), colored by velocity magnitude in m/s

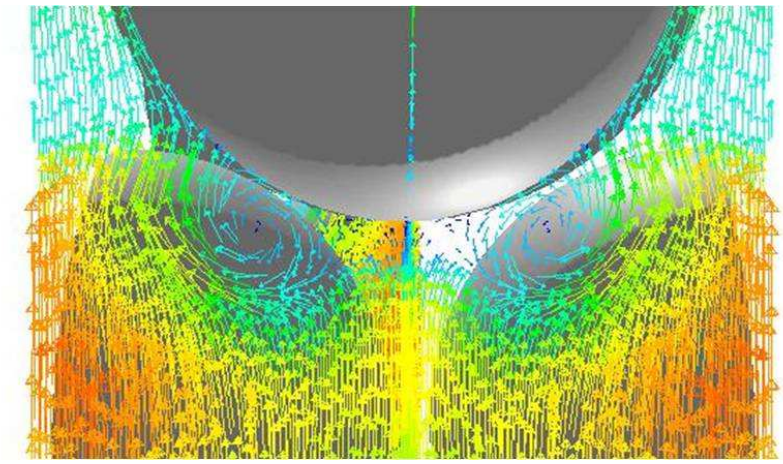

Figure 4.22: Velocity vector map of the simulation on the Grid 7(2149 cells/cm^3), colored by velocity magnitude in m/s

With respect to the pressure drop, however, an interesting linear relation is found in comparing a series of the CFD simulations on the coarsest grid (Grid 1) against the results calculated from Brauer′ correlation. Table 4.11 and Fig. 4.23 present the calculation of the pressure drop as a function of the superficial velocity. From the comparison, we can easily find that the pressure drop obtained from Brauer′s correlation is approximately equal to 5 times of CFD data ($\Delta P_{Brauer} \approx 5 \cdot \Delta P_{CFD}$).

From the analysis presented above, it can be concluded that extremely fine grid is required if precise prediction of the turbulence or the flow structure in small-scale is very important to the simulation, for example in the case that heat transfer between the fluid and the solid is concerned. However, extremely fine grid also implies extremely high computational cost. Table 4.10 shows how the CPU time soars with the increasing of the grid density. Therefore, just as mentioned at the beginning of this chapter, compromise must be made currently. Given that heat transfer is not considered and the restriction of the computer resource, the coarsest grid is used in this work.

Table 4.11: Comparison of pressure drop prediction between CFD simulation and Brauer′s correlation (CFD simulations performed on Grid 1)

Velocity $[m/s]$		0.5	1.0	3.0	5.0	10.0
ΔP	ΔP_{CFD}	8.14	29.32	250.67	660.38	2469.83
$[Pa/m]$	ΔP_{Brauer}	41.4	152.8	1222.9	3222.5	12011.1

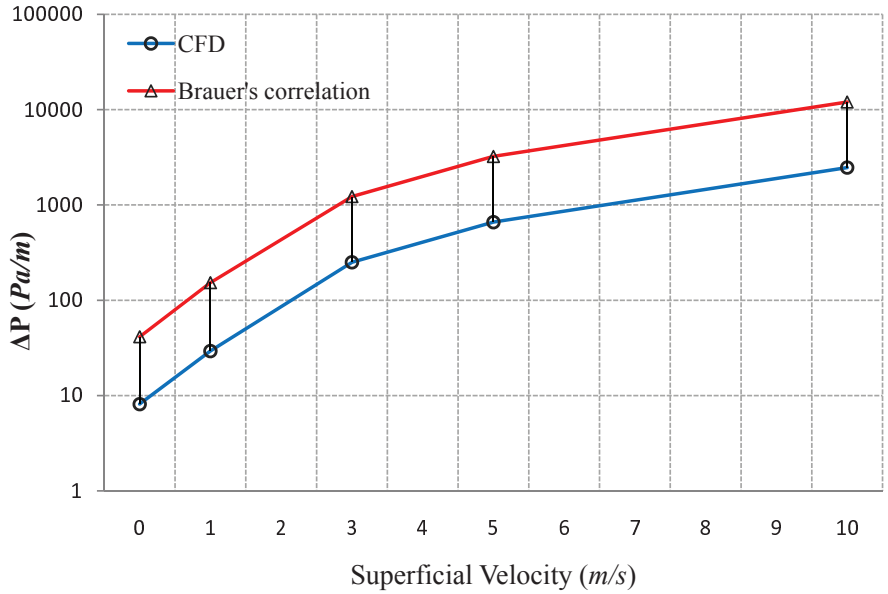

Figure 4.23: Pressure drop as a function of velocity calculated by CFD and Brauer′s equation

Additionally, special grid design is necessary to deal with the cases in which the void fraction of the packing is smaller. A smaller void fraction indicates smaller

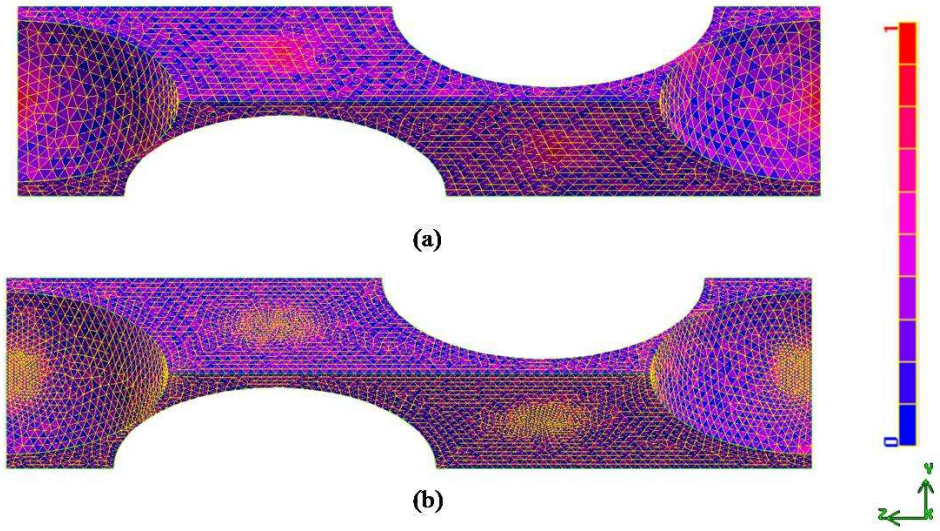

Figure 4.24: Comparison of grid quality between the normal mesh and the graded mesh: (a) mesh based on uniform interval size, and (b) mesh based on size function, colored by the skewness.

gaps between particles, which may lead to extremely high skewed cells when a coarse mesh is generated. To solve this problem, a *size function* is defined. In the function, the cell number in the nearest area of two particles is fixed, a growth rate and a limit size of cell are given, which means that smaller cells are forced to be generated in the gaps and then the size is growing in a certain rate with the increasing of the void. Fig. 4.24 shows the quality of the normal mesh and the graded mesh based on size function. Fig. 4.25 depicts the grid pattern of the graded mesh in the full-bed model.

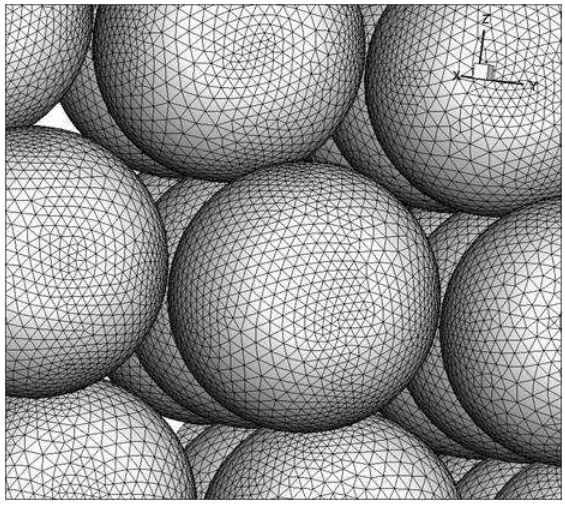

Figure 4.25: Graded mesh design on the surface of particles

4.5 Summary

Verification is quite important for CFD simulation. Grid convergence study for the 2-D and 3-D models are performed in this chapter. *Unit models*, instead of the full geometric models, are employed to reduce the computational efforts. As a general verification approach, grid convergence index method is used for the grid study of 2-D model. Considering the influence of the wall on the turbulence modeling, κ-ϵ turbulence model with enhanced wall treatment is applied for the grid study of 2-D model. Accordingly, boundary layers on the walls are created to meet y^+ criterion. For 3-D modeling, enhanced wall treatment is impractical due to the requirement of high resolution near the wall. Alternatively, κ-ϵ turbulence model with standard wall function is applied. Simulations on a series of grids with different grid density are carried out. Based on the observed values of pressure drop and by comparing the simulation results with the known analytical solutions, it is found that extremely fine grid is required to achieve grid independent solution. On industrial scale modeling, however, this will lead to huge grid size which is unmanageable respect to the current computer power. Taking the practice into consideration, a coarse grid with local refinement is decided to be used; and in the smaller void fraction case, a graded mesh is developed to improve the mesh quality in the small gaps.

Chapter 5

2-D Flow Simulations

2-D modeling has great advantage in reducing the computational cost, but at the same time it has serious flaws in geometric modeling as discussed in the Chapter 3. The short computational time and the simplified geometry make it possible to investigate the operating and geometric parameters extensively, while the disadvantages in geometry almost make the possibility of modeling the real process excluded. In this sense, the main purpose of 2-D modeling is to obtain the general information on the jet behavior in packed bed and some knowledge about the effects of the different geometries and boundary conditions which is important to develop 3-D models. Therefore,the operating conditions applied for the simulations may or may not follow the real industrial cases.

In this chapter, the simulations are carried out in two parts. In the first part, without loss of generality, the shaft kilns are regarded as packed bed reactors with jet injections. The work aims to obtain some general information of the jet behavior in cross flow in packed beds. Combustion is not considered for simplification. Accordingly, CO_2 and N_2 are used as the fluid of the jet flow and the main stream respectively instead of fuel injection and cooling air in shaft kiln process. In part 2, combustion is introduced in modeling and the results are compared with the simulations of the cold flow. Boundary conditions are calculated from the basic mass and energy balance of lime shaft kilns.

5.1 Simulations of *cold flow*

5.1.1 Description of geometries and grid in near jet region

Fig. 5.1 shows the geometry of the structured packed bed with side slot nozzle. The main body of the geometry is a half perpendicular plane of a tube, which is subtracted by circles corresponding to packed tubes with diameter of d. The bottom edge in x-direction is defined as the inlet for the main stream (N_2). The nozzle, highlighted yellow, is 100 mm in length. Besides this configuration, the nozzle is also put into the loading as a lance or situated on the axis to provide a vertical center injection.

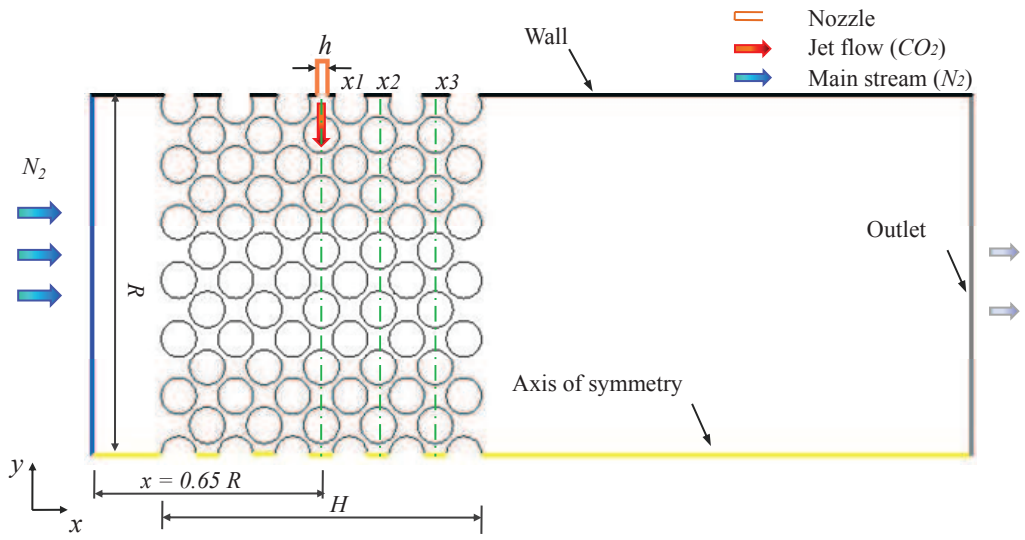

Figure 5.1: Geometry of packed be with side-nozzle

In Fig. 5.1, h is the width of the slot nozzle, varying from 20 to 90 mm. H is the bed height which is changing from 90 mm to 3000 mm to determine the appropriate height for simulation. $x1$, $x2$, and $x3$ are referring lines at where the data are extracted in need of post-processing. Unless specified, the radius of the packed tube (R) is 1 m , the particle diameter (d) is 100 mm, and the void fraction (φ) is 0.4.

In the Chapter 4, grid convergence study is performed without considering the jet flow. Regarding that the dimension of the nozzle is relatively small and the jet velocity is much higher, the cell size used for the normal fluid domain is too large to mesh the nozzle and the near jet region. Size function is used to control the size of the mesh in the specified region surrounding the nozzle to increase the accuracy and reliability and meanwhile to circumvent convergence problems caused by deterioration of the grid quality when the small cells connecting to the large cell directly.

The type of size function employed is called “Meshed”. In this function, the mesh size of a given entity is specified as starting size and, a “growth rate” and a “size limit” are defined to control the mesh size of the rest domain.

Fig. 5.2 to 5.3 show the grids in the near jet region generated with and without size function. By comparison, we can find that with the help of size function the meshes are more finer and smooth throughout the specified domain.

5.1.2 Definition of the simulation model and materials

Turbulence flow is assumed in the calculations. The standard κ-ϵ model with enhanced wall treatment is applied. Species transport model is used to calculate the non-reacting multi-species transport. According to the grid independence study performed in Chapter 4, the first order upwind schemes are selected to compute the field variables. The SIMPLE is used for the pressure-velocity coupling algorithm.

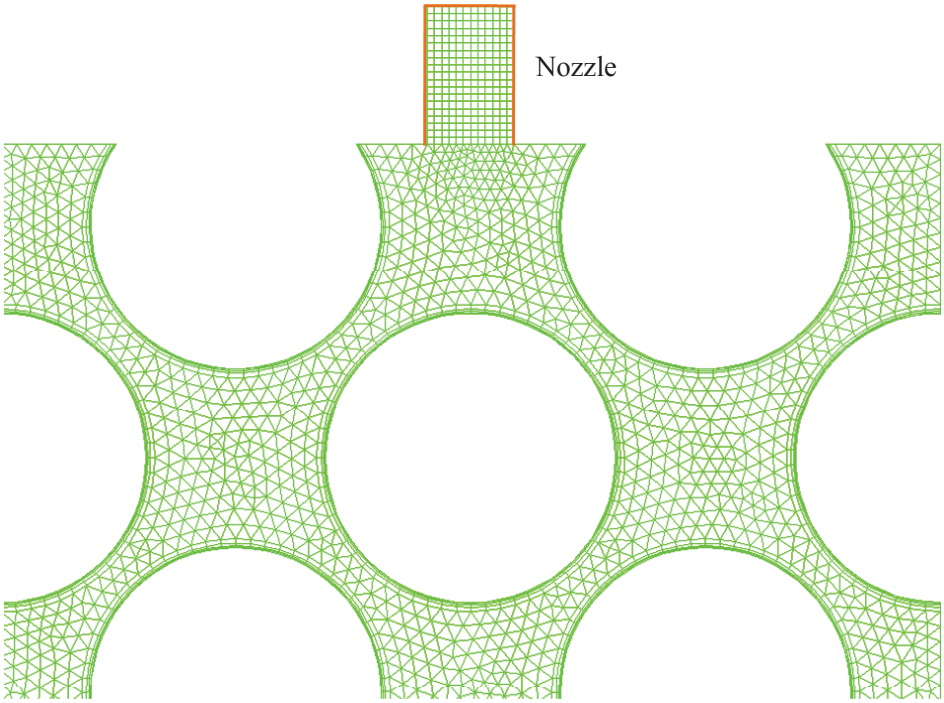

Figure 5.2: Grid in the near jet region without size function

The relaxation factors for each transport variables are shown in Table 5.1.

Convergence of the solution of each variable is assumed at a residual value of 10^{-3} except that of the energy which is at 10^{-6}.

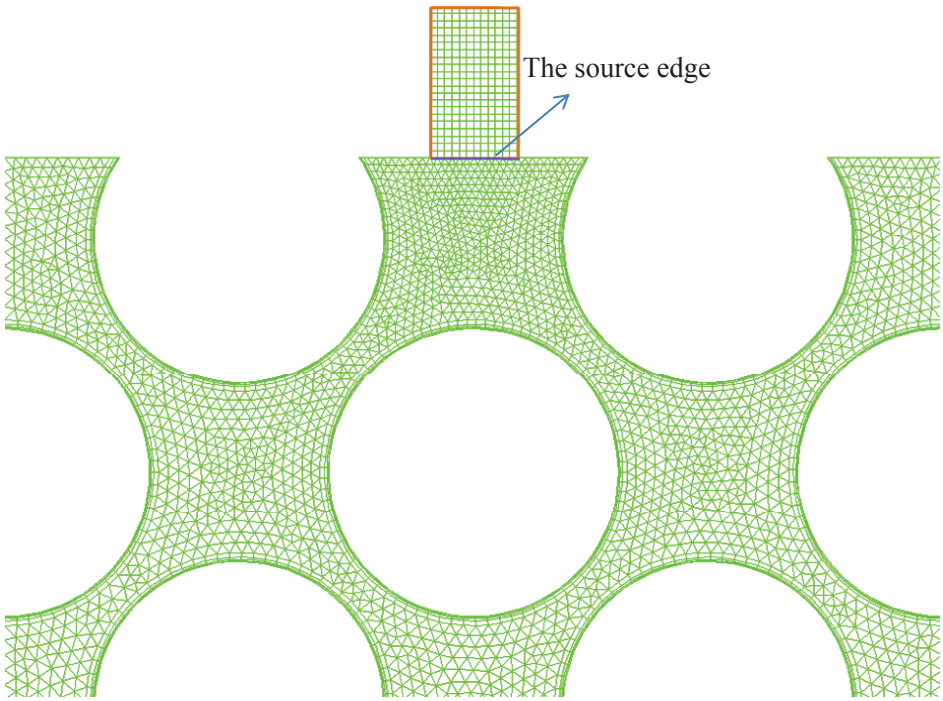

Figure 5.3: Grid in the near jet region with the *Meshed size function*; Growth rate:1.01, and Size limit: 5 mm

Table 5.1: Under-relaxation factors for the computing variables

Pressure	Density	Body forces	Momentum	κ	ϵ	Turbulent viscosity	N_2	Energy
0.3	1	1	0.7	0.8	0.8	1	1	1

CO_2 and N_2 are used as the fluid. The properties of them are listed in the Table 5.2. The properties of the mixture are also shown in the table to specify the rules governing the interaction of the two species.

Table 5.2: Properties of the gases

Properties / Gas	ρ (Kg/m^3)	C_p $(J/Kg/K)$	λ $(W/m/K)$	μ $(Kg/m/s)$	D_{ij} (m^2/s)
CO_2	1.788	840.37	0.0145	$1.37e^{-5}$	-
N_2	1.138	1040.67	0.0242	$1.663e^{-5}$	-
Mixture	incompressible ideal gas	mixing law	ideal gas mixing law	$1.72e^{-5}$	$2.88e^{-5}$

In the table, D_{ij} is the mass diffusivity for the component i in component j. The value can be calculated from Fujita′s formula [57]:

$$D_{ij} = \frac{6.70 \times 10^{-8} T^{1}.83 \left(\frac{1}{M_i} + \frac{1}{M_j}\right)^{1/2}}{P \left[\left(\frac{T_C}{P_C}\right)_i^{1/3} + \left(\frac{T_C}{P_C}\right)_j^{1/3}\right]^3} \tag{5.1}$$

where the operating temperature, T and pressure, P are 298 K and 101325 Pa, respectively. T_C and P_C are the critical condition and can be obtained from Wakao [58].

Considering that the mass diffusivity is not critical in the following simulations, the default value is used.

5.1.3 Effect of bed height on jet behavior

In the industries, the shaft kiln can be up to 30 meters high. CFD simulation of the whole furnace is prohibitively expensive and impractical due to the tremendous number of particles (processed material) involved. As the aerodynamic region, the burning zone of the shaft kilns, has a decisive effect on limestone firing, the primary aim of the CFD simulation is to visualize the flow fields in this portion. The very important questions in geometric modeling are that whether the bed height affect the jet behavior and what would be the minimum bed height for a representative geometric model.

To study the effect of the bed height on the jet behavior, simulations are performed on geometries with bed height of 900 mm and 3000 mm. Investigations are done upon geometries with side-nozzle (slot shaped) and center-nozzle (tube shaped) as well to avoid the influence of the situation and the shape of the nozzles.

Boundary and Initial conditions

Table 5.3: Boundary conditions

		D_h (m)	I (%)	Velocity (m/s)	Temperature (K)
Inlet	Jet flow	0.06	5	12.5	300
	Main stream	2	10	0.25	300
Outlet		2	10	-	300

In the table, D_h is hydraulic diameter, velocity is superficial velocity, and I is the turbulence intensity. Normally, the turbulence intensity at the inlet boundary can be obtained from external, measured data. The turbulence intensity at the core of a full-developed duct flow can also be estimated from the following formula derived from an empirical correlation from pipe flows [5]:

$$I = \frac{u^{'}}{u_{avg}} = 0.16(Re_{DH})^{-1/8} \tag{5.2}$$

where $u^{'}$ is the root-mean-square of the velocity fluctuations, and u_{avg} is the mean flow velocity.

In this work, however, the values are estimated roughly due to no measured data available and the complicated history of the upstreams. Solution initialization is computed from the main stream inlet conditions. In the other calculations, solutions are initialized in the same way except specific cases.

Simulation results

In the following, the effect of the bed height on the jet behavior is illustrated by comparing the CO_2 distributions in beds with different height. To avoid losing the generality, simulations are carried out on geometries with two types of nozzles. As the geometries are axisymmetric, one is horizontal slot-shaped nozzle and the other, on the axis, is vertically tube-shaped. The comparisons are shown by means of displaying the mass fraction of CO_2 and plotting the distribution of CO_2 along the cross-section at the jet level. The results are presented in Fig. 5.4 to 5.7.

In both cases, apparently, there is no big difference can be observed by comparing the CO_2 contours in the packing zones. And CO_2 concentration plots at the

jet level are neatly the same. Altogether the results indicate that the bed height has no obvious impact on the jet behavior in the bed, i.e. the jet penetration.

The effect of bed height on the jet flow in a packed bed has been also experimentally studied by Chukin and Kuznetsov [59]. From their 50 experiments, a conclusion was drawn that, after the full expansion of jet flow into the bed, change in the bed height would not affect the gas-flow distribution. The experimental data also shows that the stabilization in the gas-flow distribution over the bed cross section begins even at a height of 15 mm. In other words, the jet expansion height is about three to four layers in terms of the particle size ($d_p = 4.6$ $6.0mm$). In order to make a comparison with the CFD simulation, mass fraction of CO2 along 4 cross-sections are plotted in Fig. 5.8. It shows that the largest discrepancy of CO2 concentration is found from $x1$ to $x2$, and then the difference gradually diminished. According to this tendency, the stabilization height predicted by the CFD simulation was around 300 mm, 3 packing layers above the nozzle, which is in good agreement with the experiments. Of course, the stabilizing height of the circumferential jet also depends on the nozzle-to-particle diameter ratio.

The finding that the jet behavior is independent of the bed height has great significance in model reduction. The computational efforts can be reduced dramatically by applying a section model instead of the entire model.

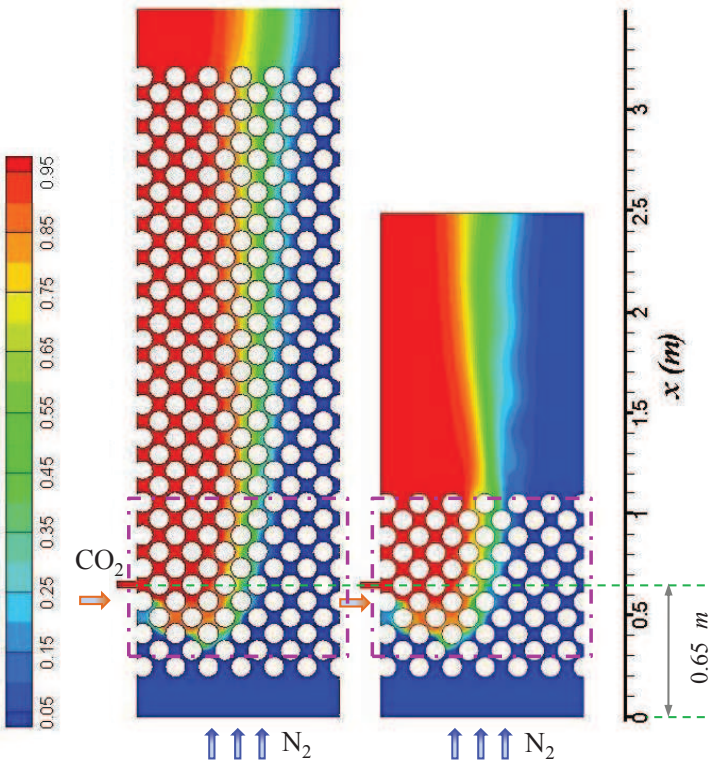

Figure 5.4: Comparison of the mass fraction contours of CO_2 in beds with height of $H = 3.0m$ and $H = 0.9m$ (slot-shaped nozzle); $v_{CO_2} = 12.5$ m/s, $v_{N_2} = 0.25$ m/s

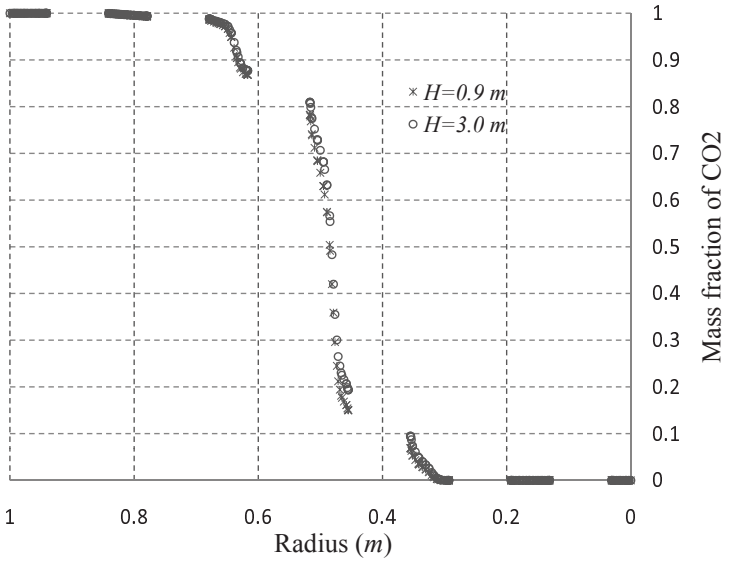

Figure 5.5: Comparison of the mass fraction of CO_2 along the cross-section at $x = 0.65\ m$ in beds with height of $H = 3.0m$ and $H = 0.9m$(slot-shaped nozzle); $v_{CO_2} = 12.5\ m/s$, $v_{N_2} = 0.25\ m/s$

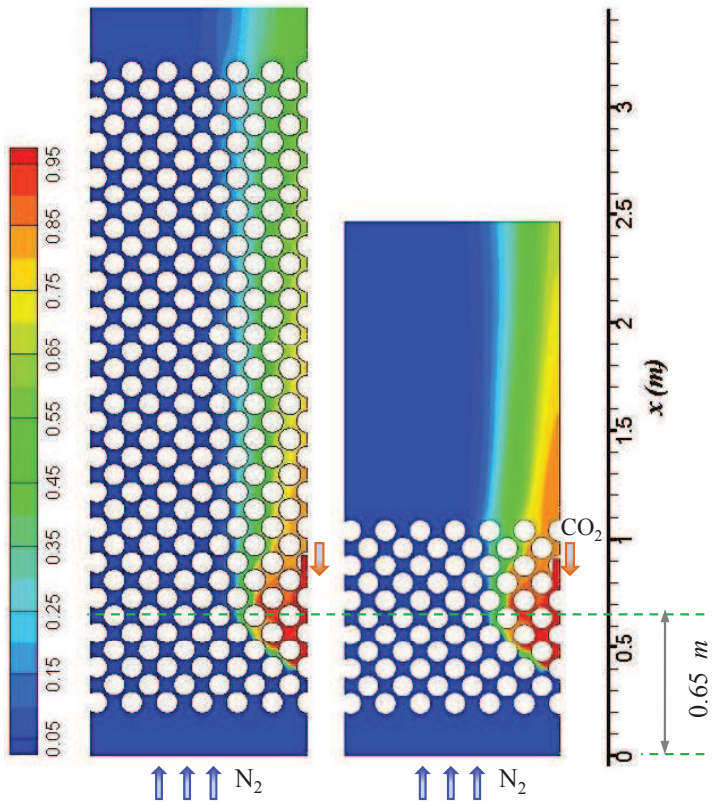

Figure 5.6: Comparison of the mass fraction contours of CO_2 in beds with height of $H = 3.0\ m$ and $H = 0.9\ m$ (tube-shaped nozzle); $v_{CO_2} = 12.5\ m/s$, $v_{N_2} = 0.25\ m/s$

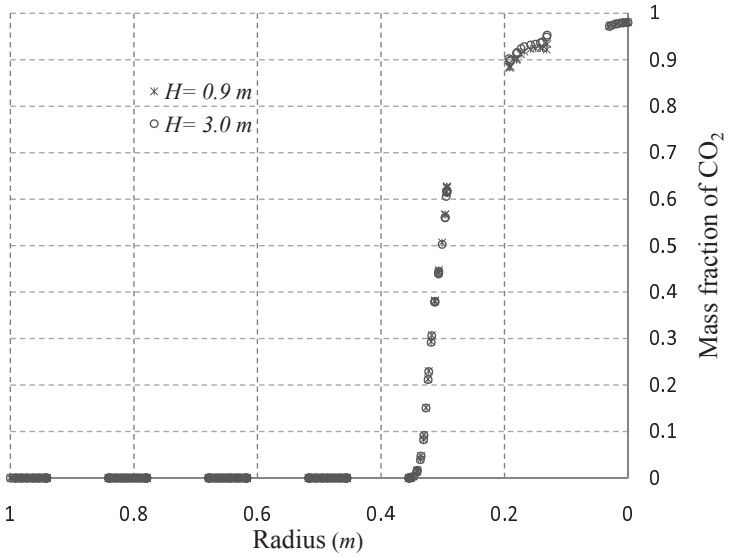

Figure 5.7: Comparison of the mass fraction of CO_2 along the cross-section at x = 0.65 m in beds with height of H = 3.0 m and H= 0.9 m(tube-shaped nozzle); v_{CO_2} = 12.5 m/s, v_{N_2} = 0.25 m/s

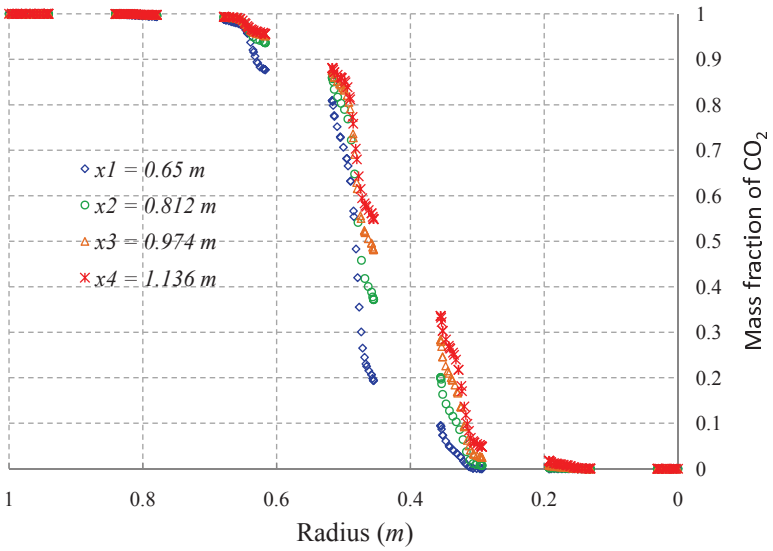

Figure 5.8: Distribution of CO_2 along different cross-sections(tube-shaped nozzle); v_{CO_2} = 12.5 m/s, v_{N_2} = 0.25 m/s

5.1.4 Effect of packing near the side-nozzle on jet behavior

As presented in the Chapter 3, the wall of the geometric model is also subtracted by particles to circumvent channeling problem near the wall. This limits the packing possibilities severely near the nozzle, especially the nozzle situated at the side. In order to prevent losing the generality of the geometry in the case of quantitative simulation, the packing near the side-nozzle is studied.

Fig. 5.9 shows a normal structure of packing near the side-nozzle. The nozzle is surrounded by particle 1, 2 and 3. In the figure, one can well imagine that the main stream can not bypass particle 1 and interact with the jet flow directly, and thereby the mixing between the two flows is under-predicted. Even worse is on the redistribution of the jet flow, which makes the jet behavior almost independent of the jet velocity for a given volume flow rate of the jet. It can be noted that the velocity of the redistributed jet flows only depends on the volumetric flow rate of the upstream jet as the areas ($A2$ and $A3$)of gaps are fixed. That is to say, if we change the size of the nozzle within the bound of particle 1 and 3 to change the jet velocity, the overall jet behavior in the bed can not be impacted much, and this can be misleading. Geometric model based on this structure is called *Model A*.

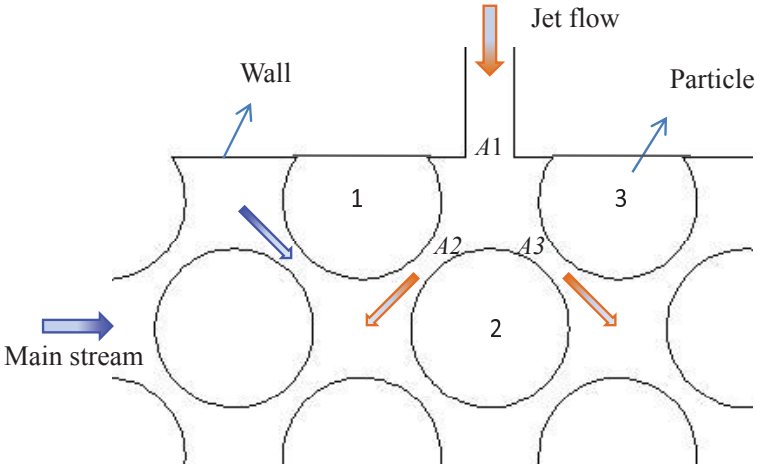

Figure 5.9: The structure of packing near the side-nozzle (Model A)

In Fig. 5.10, an improved geometric model is shown. In this model, one particle surrounding the nozzle (particle 1 in Fig. 5.9) is reduced in size, and a "bridge" is set up between the main stream and the jet flow. Geometry based on this packing structure is named *Model B*.

Boundary conditions

The dimensions of the geometries and the boundary conditions are the same as that given in Table 5.3 except the inlet velocity of the jet flow. The jet velocities of 4 m/s, 10 m/s and 22 m/s are used for the simulations. As the width of the nozzle

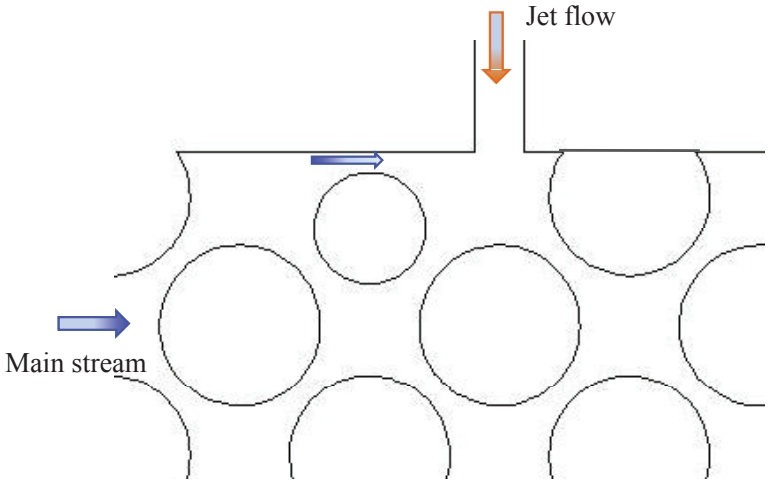

Figure 5.10: The structure of packing near the side-nozzle after being improved (Model B)

(h) is fixed, higher of the jet velocity means increase in the volumetric flow rate of CO_2. For the three cases, the volumetric flow ratio of CO_2 and N_2 ($\dot{V}_{CO_2}/\dot{V}_{N_2}$) is 1.06, 2.64, and 5.81, respectively.

Simulation results

Simulations are carried out on Model A and Model B to estimate the influence of the packing. The mass fraction contours of CO_2 and mass fraction of CO_2 on the cross-section $x1$ ($x = 0.65\ m$) are displayed and compared in Fig. 5.11 to Fig. 5.16. The effect is to be discussed based on the impact of the packing on the jet penetration and on the mixing between the jet and main flows as well.

As shown in the figures, there′s no significant difference can be found in each case regarding to the jet penetration, which is obviously dominated by the volumetric flow ratio of the jet flow to the main stream. In respect to the mixing of the flows, it appears that the influence is slight in low jet velocity case, and then getting stronger with increasing in jet velocity. A much better mixing can be observed below the jet area with Model B in the case with jet velocity of 22 m/s as illustrated in Fig. 5.15 and 5.16.

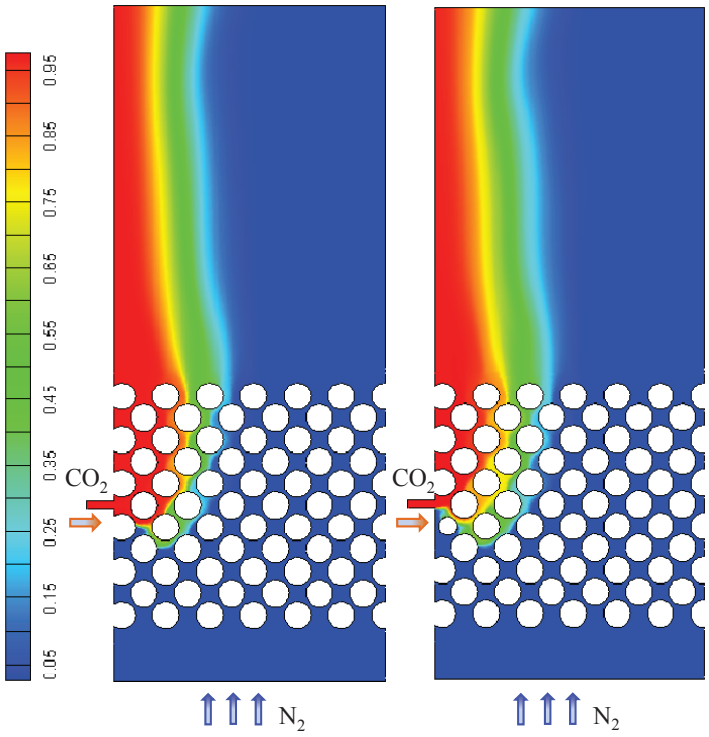

Figure 5.11: Comparison of CO_2 contours obtained upon geometric model A and B; Jet velocity $v_{CO_2} = 4\ m/s$, $\dot{V}_{CO_2}/\dot{V}_{N_2} = 1.06$

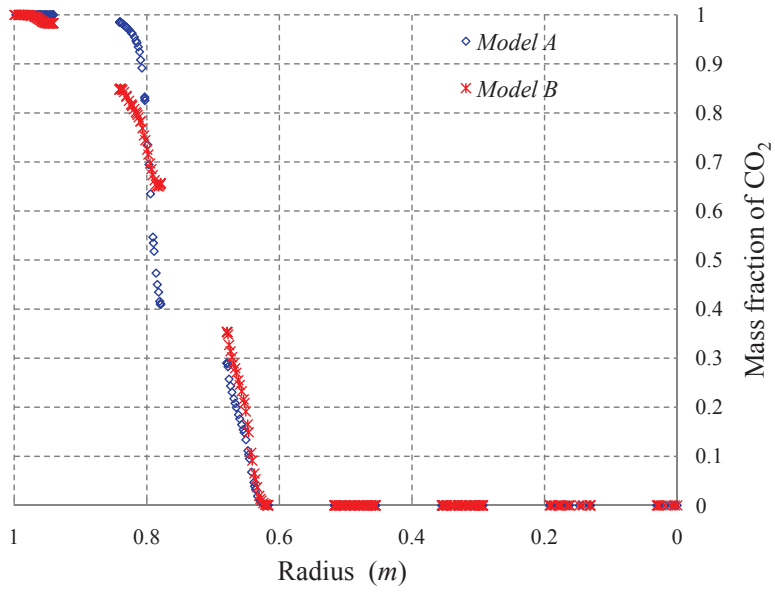

Figure 5.12: Comparison of mass fraction of CO_2 along $x1 = 0.65m$; Jet velocity $v_{CO_2} = 4\ m/s$, $\dot{V}_{CO_2}/\dot{V}_{N_2} = 1.06$

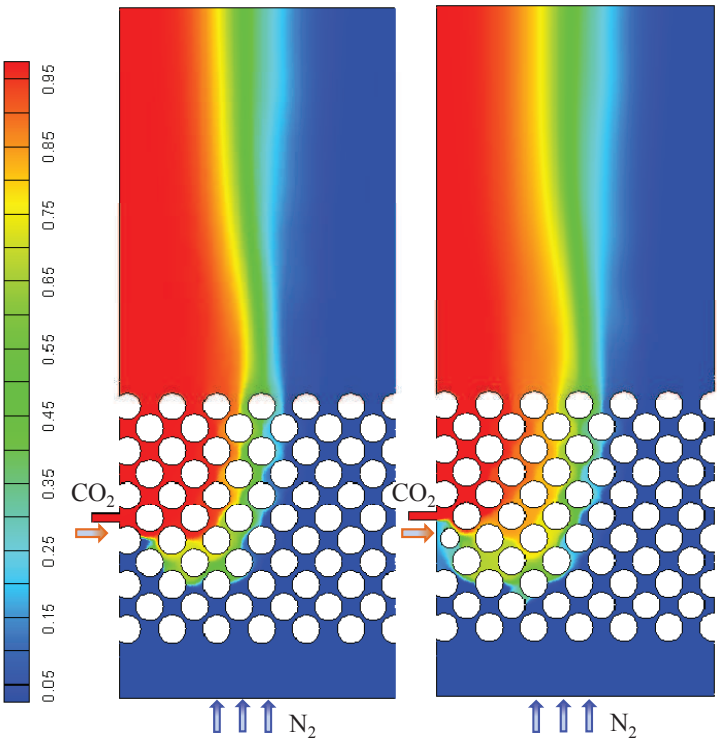

Figure 5.13: Comparison of CO_2 contours obtained upon geometric model A and B; Jet velocity $v_{CO_2} = 10\ m/s$, $\dot{V}_{CO_2}/\dot{V}_{N_2} = 2.64$

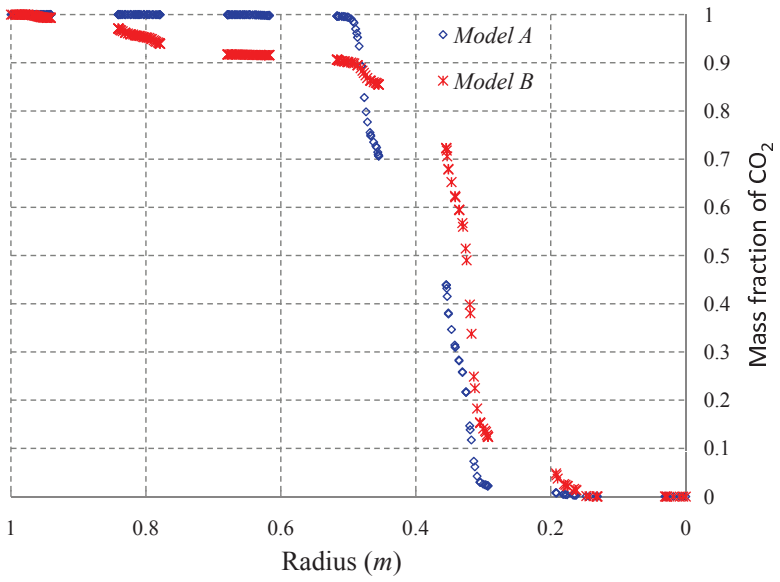

Figure 5.14: Comparison of mass fraction of CO_2 along $x1 = 0.65m$; Jet velocity $v_{CO_2} = 10\ m/s$, $\dot{V}_{CO_2}/\dot{V}_{N_2} = 2.64$

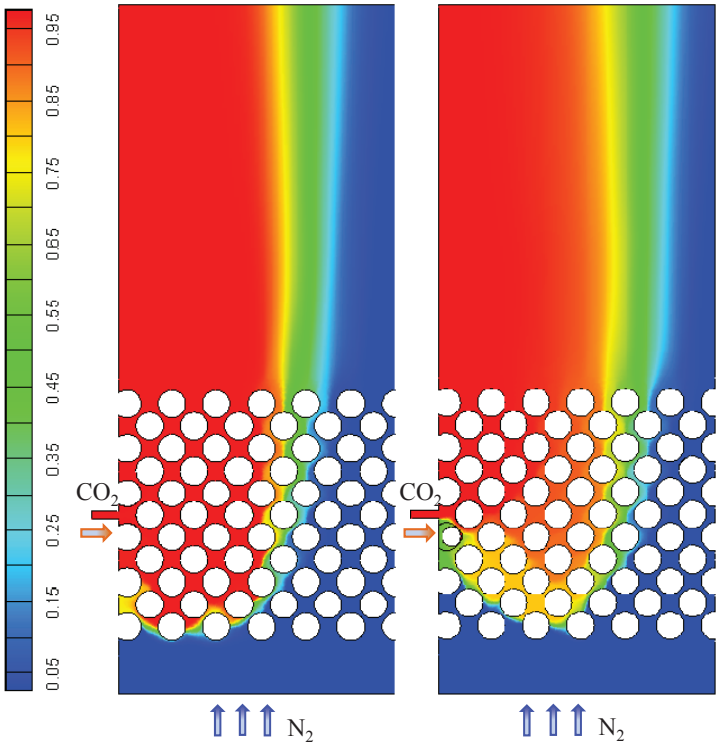

Figure 5.15: Comparison of CO_2 contours obtained upon geometric model A and B; Jet velocity $v_{CO_2} = 22\ m/s$, $\dot{V}_{CO_2}/\dot{V}_{N_2} = 5.81$

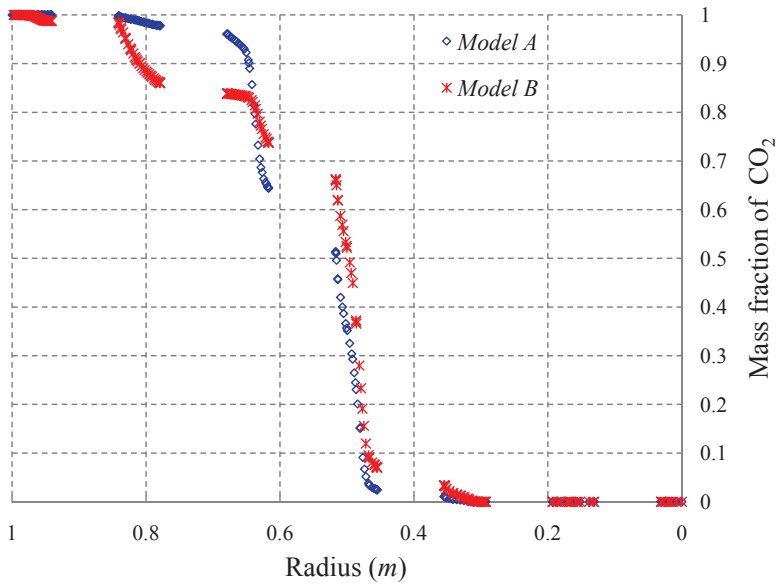

Figure 5.16: Comparison of mass fraction of CO_2 along $x1 = 0.65m$; Jet velocity $v_{CO_2} = 22\ m/s$, $\dot{V}_{CO_2}/\dot{V}_{N_2} = 5.81$

The influence of the packing structure near the slot-shaped nozzle on the mixing can be easily explained with the illustration of the path lines released from the inlet of main stream, as shown in Fig. 5.17. The left is the main stream pathlines obtained upon geometric model A. It is plain to see that the main stream, forced by the jet flow, flows toward the center of the bed, and mixing only occurs in the interface by means of diffusion. While in the case of Model B employed, part of the main stream, sucked by the jet flow, flows to the jet and mixes with the jet flow partially. The behavior of jet flow also implies that, to increase the jet velocity for a given volumetric flow ratio of the jet to the main stream may not improve the jet penetration significantly but can somehow enhance the mixing. More investigations on the effects of jet velocity on radial gas distribution in a packed bed are conducted in the next section.

Therefore, a conclusion can be drawn that no special treatment on the packing near the nozzle is required if only the jet penetration is to be estimated, whilst particular attention on the geometry must be paid when mixing efficiency is concerned.

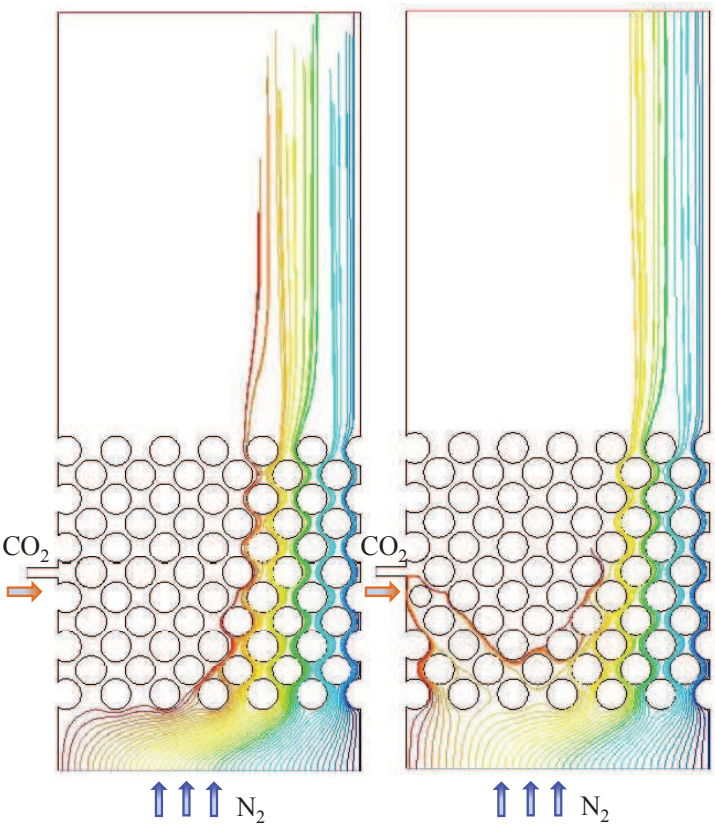

Figure 5.17: Comparison of pathlines of N_2 with different geometric model A and B, color by particle ID; Jet velocity $v_{CO_2} = 22m/s$

5.1.5 Effect of jet velocity on jet penetration and radial gas distribution

Many researchers have investigated the characteristics of circumferential jets in a cross flowing fluid [60, 61, 62]. Based on their findings, the momentum flux ratio (J) defined by Eq. 5.3 is one of the dominant influence factors on the jet penetration.

$$J = \rho_j v_j^2 / \rho_m v_m^2 \tag{5.3}$$

where the subscript j and m identify the jet flow and the main stream, respectively.

Substituting the velocities by the volume flow rates correspondingly, Eq. 5.3 yields

$$J = \frac{\rho_j}{\rho_m} \left(\frac{D^2}{n \cdot d_j^2} \right)^2 \left(\frac{\dot{V}_j}{\dot{V}_m} \right)^2 \tag{5.4}$$

where n is the number of nozzle, D is the diameter of bed, and d_j is the diameter of tube-shaped (round) nozzle.

In 2-D modeling, the nozzle is limited to one circumferential slot, and thereby Eq. 5.4 is changed as

$$J = \frac{\rho_j}{\rho_m} \left(\frac{D}{4 \cdot h} \right)^2 \left(\frac{\dot{V}_j}{\dot{V}_m} \right)^2 \tag{5.5}$$

where h is the width of slot-shaped nozzle.

Apparently, the momentum flux ratio can be increased by reducing the dimension of the nozzle(s) for the given volume flow ratio and number of nozzles, or by increasing the volumetric flow ratio ($\dot{V}_j/\dot{V}_m$) when the dimension and number of the nozzles are fixed.

As well known, the volumetric flow ratio also plays the dominant role on the jet penetration depth in a packed bed reactor. This is revealed by the comparison of Fig. 5.11, 5.13, and 5.15, in which one can find that the penetration depth of the jet flow is proportional to $\dot{V}_j/\dot{V}_m$. However, very few data are available on the effect of jet velocity by changing nozzle dimension in a packed bed. In this section, effects of nozzle dimension are studied. The gas flow rate is kept constant, so that a reduction in the nozzle width results in an increase in the velocity ratio (the momentum flux ratio).

Inlet boundary conditions

In this study, the nozzle hydraulic diameter is varied from 0.02 m to 0.09 m. The superficial velocity of the main stream or cross-flow is kept constant at 0.25 m/s in the cases with horizontal lance and 0.5 m/s in the center-nozzle (vertical) cases. The jet velocity is calculated corresponding to the volumetric flow ratio ($\dot{r} = \dot{V}_j/\dot{V}_m$) which is shown in Table 5.4. The values are not taken from any actual plant data. In vertical nozzle cases, the nozzle is round and the jet outlet area is relatively small which results in high jet velocity comparing with the nozzle lance, therefore, a higher v_m and a lower $\dot{r}$ are defined to prevent over-penetrating. Meanwhile, the bed height is one row higher for the high jet velocity cases to make sure that over-penetrating does not occur.

Table 5.4: Inlet boundary conditions of the nozzle

Nozzle	Case	D_h (m)	v_j (m/s)	I $(\%)$	T (K)	$\dot{r}$ -
Horizontal	I	0.09	4.8	5	300	1.55
	II	0.06	7.2			
	III	0.02	21.5			
Vertical (Center)	IV	0.06	16.0	5	300	0.0576
	V	0.04	36.0			
	VI	0.02	144.0			

Simulation results

Similarly as before, the contours of CO_2 are displayed to show the jet penetration and the gas mixing. As only the radial penetration and gas mixing are considered in this work, the jet penetrations depth of the vertical jet is defined as the horizontal distance from the nozzle exit to the furthest point that the jet flow (CO_2) can reach.

Fig. 5.18 and 5.19 show the CO_2 contours of each case. On the penetration of the horizontal jet, it can be noted that it is quite shallow in the cases of low jet velocity, which also leads to a poor radial gas mixing, whilst the depth is much deeper when the velocity changes from 7.2 m/s to 21.5 m/s. For the vertical jet, the penetration depth is also improved with the increases in jet velocity.

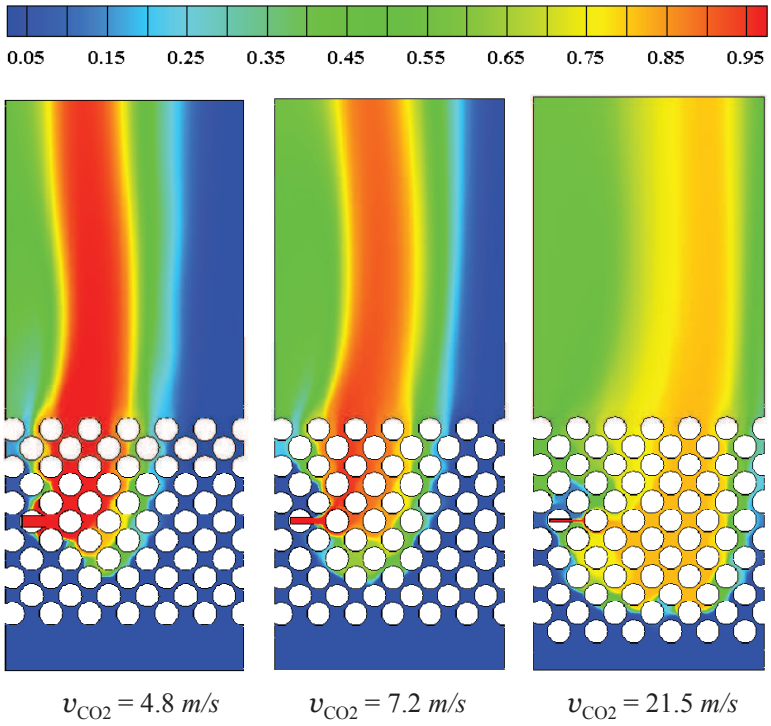

Figure 5.18: Comparison of CO_2 contours with different jet velocity (Horizontal jet); $\dot{V}_j/\dot{V}_m = 1.6$

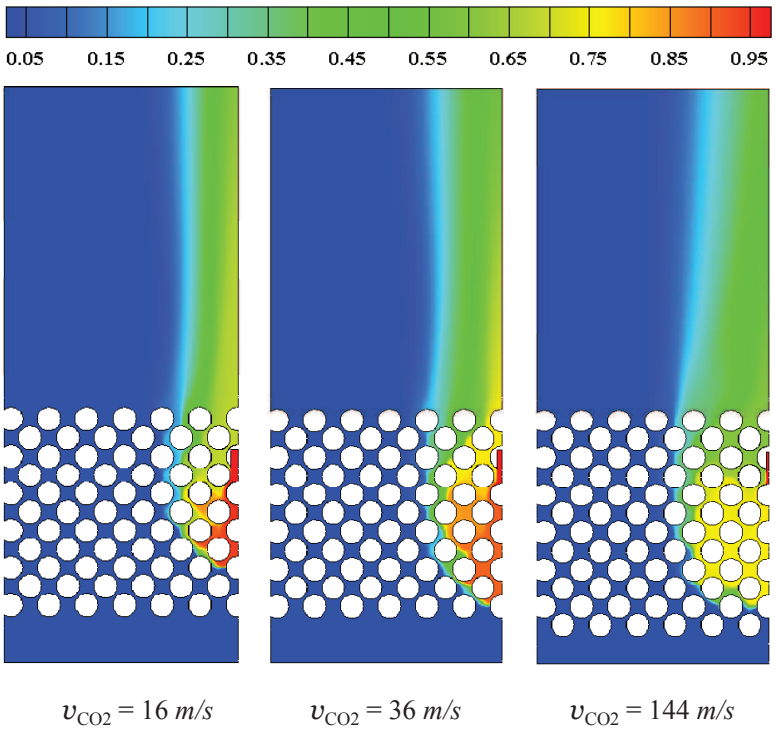

Figure 5.19: Comparison of CO_2 contours with different jet velocity (Vertical jet); $\dot{V}_j/\dot{V}_m = 0.0576$

For both types of jets, the comparisons illustrate that the radial gas mixing can be greatly enhanced with a big increase in the jet velocity. In this respect, it can be inferred that the increase in the jet velocity not only increases the radial momentum flux rate but also induces strong interaction between the jet and the main stream and thereby intensifies the mixing significantly.

The effect of jet velocity on the penetration and radial gas mixing can be further explained by comparing the main stream pathlines of cases I and III, as shown in Fig. 5.20. The pathlines show that the jet with high jet velocity (Simulation III) draws up more main flow, i.e. the jet flow rate is increased in some sense or the effective volumetric flow ratio ($\dot{r}$) is increased, and therefore penetrates deeper. While in the case of low jet velocity (Simulation I), the main stream is divided into two parts. One part flows upward along the wall and the other circumvents the jet and forms unmixed core in the center of the bed, which limits the jet penetration and leads to a poor mixing.

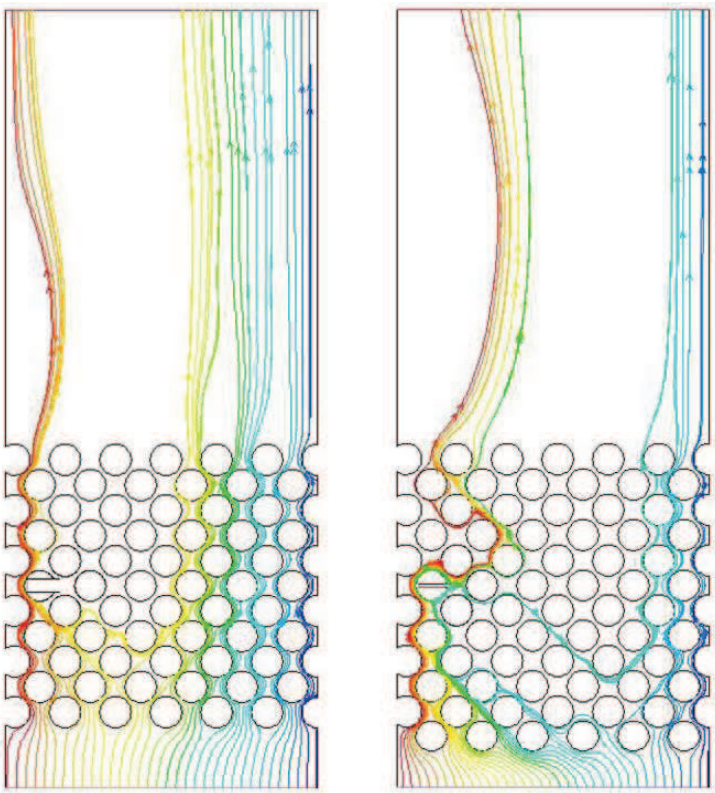

$v_{CO2} = 4.8\ m/s$ $v_{CO2} = 21.5\ m/s$

Figure 5.20: Comparison of the pathlines of the main stream with different jet velocity , colored by particle ID ; $\dot{V}_j/\dot{V}_m = 1.6$

Fig. 5.21 depicts the close views of velocity vectors in the near-jet fields. The vectors, colored by the mass fraction of N_2 (the main stream fluid), show clearly how the main stream bypasses the jet with low jet velocity while tends to mix with the high velocity jet due to jet suction(smaller nozzle).

The results prove that the jet penetration in a packed bed not only depends on the volumetric flow ratio $\dot{V}_j/\dot{V}_m$ but the momentum flux ratio (J). The effect

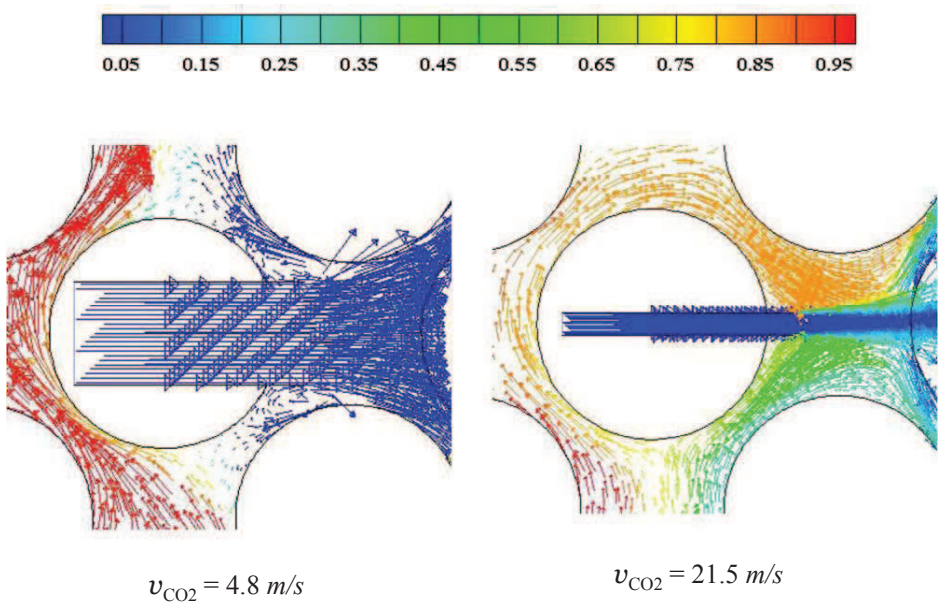

Figure 5.21: Close views of velocity vectors around the jets, colored by the mass fraction of N_2; Horizontal jet, $\dot{V}_j/\dot{V}_m = 1.6$

of change in jet velocity can not be neglected concerning the *jet induced mixing* of the jet flow and main stream. Further study is carried out in the following section to show the influence of jet velocity in the cases with combustion.

This effect can also be achieved by reducing a bigger nozzle progressively toward its outlet. This design is helpful in case that the main tube of the nozzle can not be as small as the outlet. In a premixed burner, for example, the main tube should be spacious enough for the premixing part. To increase the outlet velocity of the fuel mixture in this case, a tapering constriction of the outlet is practical. Fig. 5.22 shows the schematic structure of the nozzle used in Simulation I (the left) and a new nozzle with outlet constriction (the right).

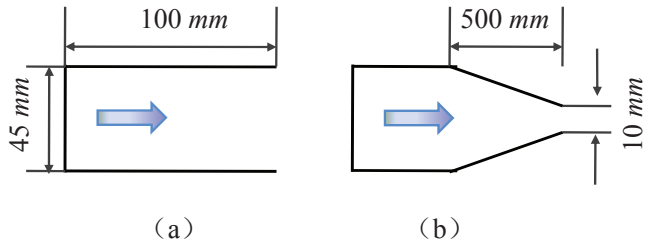

Figure 5.22: Schematics of normal nozzle (a) and nozzle with constriction (b)

5.2 Simulations of reacting flow

In this section, simulations of reactive flow are performed. Effects resulting from the changes in the geometry of the burner(s) are studied and compared with

Cold flow modeling. Simulations based on transient state are carried out as well to investigate the influence of heat transfer from gas to particles on the flow structures.

5.2.1 Description of the geometry and computational mesh

The general geometry and computational mesh are depicted in Fig. 5.23. As mentioned before, the geometry consists of 4 parts, the cooling air inlet domain, the packed region, the burner, and the outlet domain to prevent reversed flow. A gap is placed intentionally between the wall and the burner so that the cooling air can bypass the burner like the behavior in 3D. The grid has approximately a hundred thousand cells.

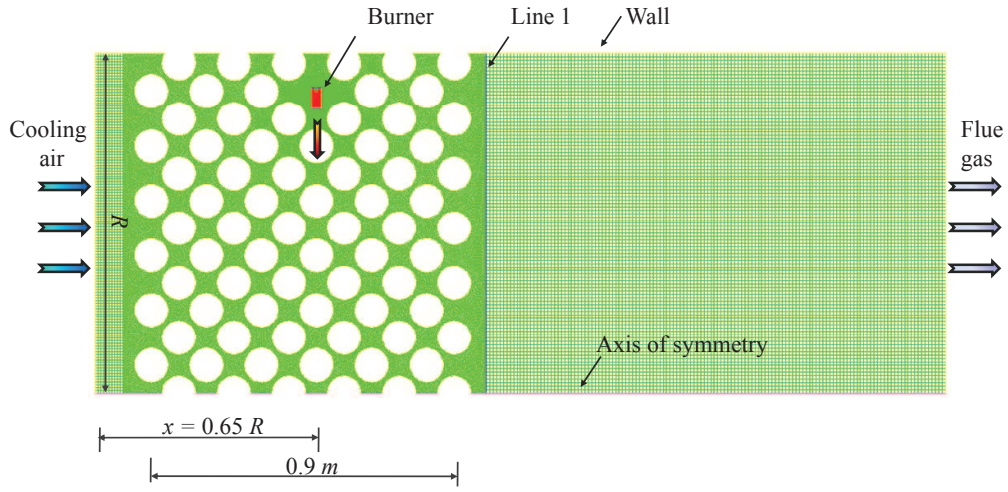

Figure 5.23: 2-D geometry for simulations of reacting flow

Comparing with the model used in the first section (*Simulations of cold flow*), the geometry has a burner instead of a simple nozzle. The 2D geometric model of the burner has been discussed in the Chapter 3. Considering that jet velocity may have great impact on the jet penetration based on the simulations of cold flow, two types of models are used in the following computations. One has the configuration of the original design, the other has a reduction in outlet to increase the jet velocity, the principle of which is described at the end of the last section. The geometries and corresponding meshes are illustrated in Fig. 5.24.

The dimension of the inlets of fuel and combustion air are fixed. The change in the dimension ratio of the inlets may also influence the flow characteristics but not the interest in this work currently. The size of the outlet is varying in a specific range to obtain different outlet jet velocity. As the dimension of the burner is relatively small, the mesh size is much smaller than that used to mesh the bed domain. Therefore, size functions are applied when creating the mesh of the bed domain surrounding the burner outlet to generate a smooth transition. The number of intervals on the edge of the fuel inlet is 10. Intervals on each edge of combustion air inlet are 12 with a growth rate of 1.025 from the inlet of fuel. Triangular elements are employed in the constriction part, as shown in Fig. 5.24,

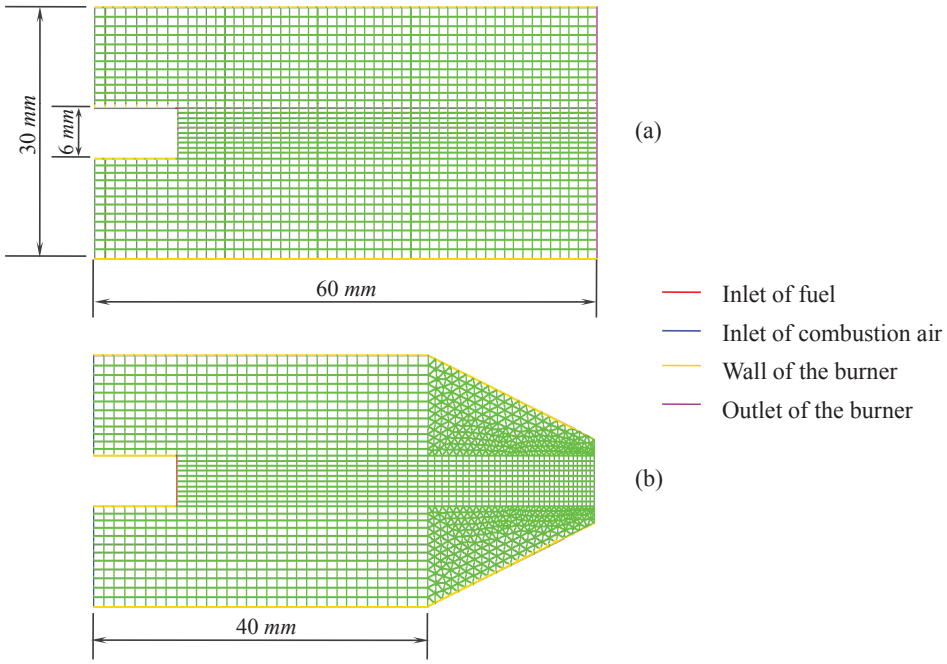

Figure 5.24: 2-D geometries and computational meshes of (a) normal burner and (b) burner with constriction outlet

in the case that the outlet is bigger than the inlet of fuel while much smaller than the normal size (without constriction).

5.2.2 Definition of the simulation model and materials

All the definition and parameters are as the same as that defined in the simulations of cold flow, the first section of this chapter, except that reactions are considered in modeling species transport. In the *Species Model*, *Volumetric Reactions* and *Eddy-Dissipation* are activated to model the combustion and the turbulence chemistry interaction. The value for density under-relaxation is reduced to 0.7 to improve the solution stability and accelerate solution convergence.

Mixture material of *methane-air-2step* in FLUENT database is used as the fluid. Default settings of the properties are applied for simulation.

5.2.3 Special procedure for combustion simulation

Obtaining a converged solution in flow with combustion is difficult especially in the case of complex geometry due to the strong impact of the reaction on the basic flow pattern. In combustion, as well known, the reactions lead to a large heat release and subsequent density changes and large accelerations in the flow.

To address this problem, a two-step process is a practical method. In this process, the flow, energy, and species equations are initially solved with disabling the reaction (the *cold-flow*, or unreacting flow). When the basic flow pattern

has thus been established, one can continue the calculation with re-enabling the reactions. This method is used in the following simulations. The procedure to accomplish this two-step approach is described in FLUENT documentation.

5.2.4 Effect of jet velocity on radial gas mixing and jet penetration

Burner dimensions and Boundary conditions

Studies are carried out on three geometries. In *Geometry I*, the outlet of the burner is 30 mm. In *Geometry II* and *III*, the outlet is reduced to 15 mm and 6 mm, respectively. The other dimensions are shown in Fig. 5.24. Boundary conditions of the inlets and outlet are listed in Table 5.5.

Table 5.5: Inlet/outlet boundary conditions

		Inlet			Outlet
		Fuel	Combustion air	Main stream	
v (m/s)		2.57	5.01	0.254	-
D_h (m)		0.012	0.048	2	2
I (%)		5	5	10	10
T (K)		300	300	600	450
Species	CH_4	1	0	0	0
mass fraction	O_2	0	0.23	0.23	0.23

Simulation results

Simulations are firstly carried out with a low initial temperature (600 K), i.e. fuel is not ignited. Then, combustion is initiated by patching a high temperature (1800K) into the fluid domain. Temperature contours are displayed in Fig. 5.25 and Fig. 5.26 to illustrate the jet penetration and the gas mixing of each case in the unreacting flow simulations and combustion simulations, respectively.

Similar as the results obtained in the first section, jet velocity has strong impact on the gas mixing which further influence the jet penetration. Fig. 5.25 shows that almost an uniform temperature distribution is achieved on Geometry III, in which the outlet jet velocity reaches around 25 m/s. However, the effects of the increase in the jet velocity are not so significant in the case of reacting flow, as shown in Fig. 5.26. This result indicates that jet-induced mixing plays a less important role in combustion case, or more high jet velocity is required to pull in the surrounding gas combustion taking place. Fig. 5.27 displays the pathlines of the main stream. Obviously, the mixing between the jet flow and the main stream is poor. None of the main stream is induced to the jet flow even in the case of high jet velocity.

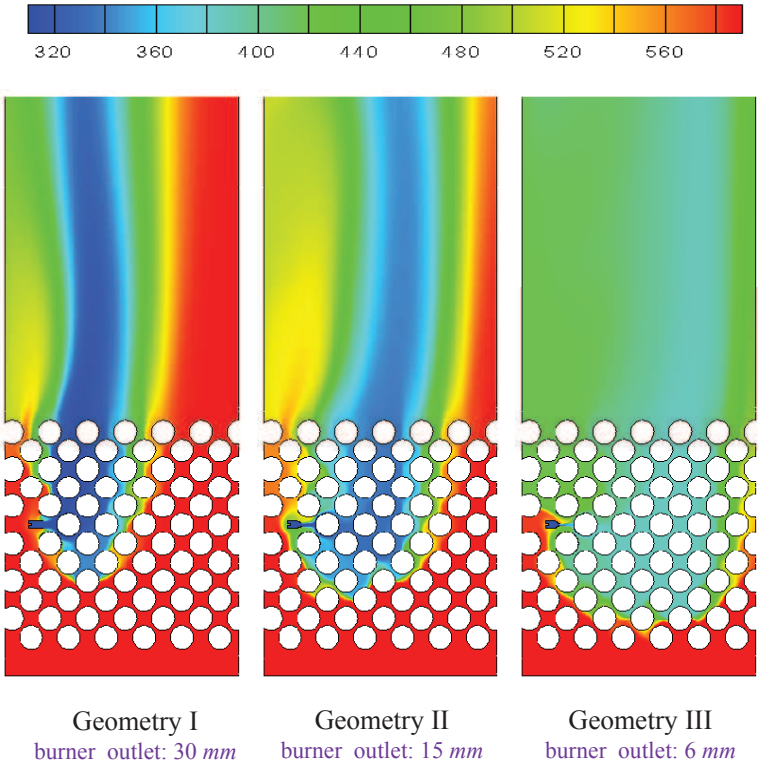

Figure 5.25: Temperature contours on each geometry (unreacting flow simulation); Legend in K

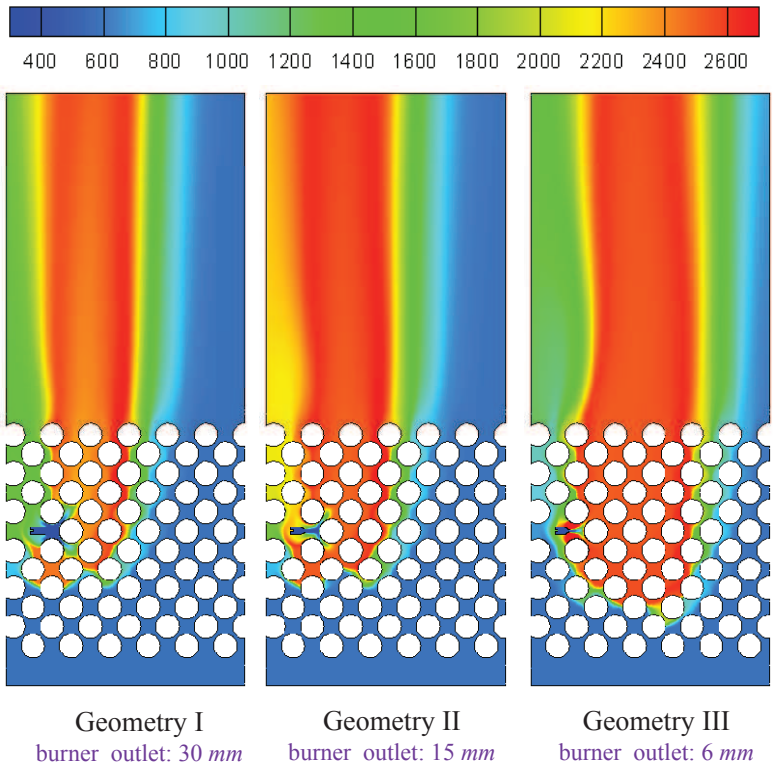

Figure 5.26: Temperature contours on each geometry (reacting flow simulation); Legend in K

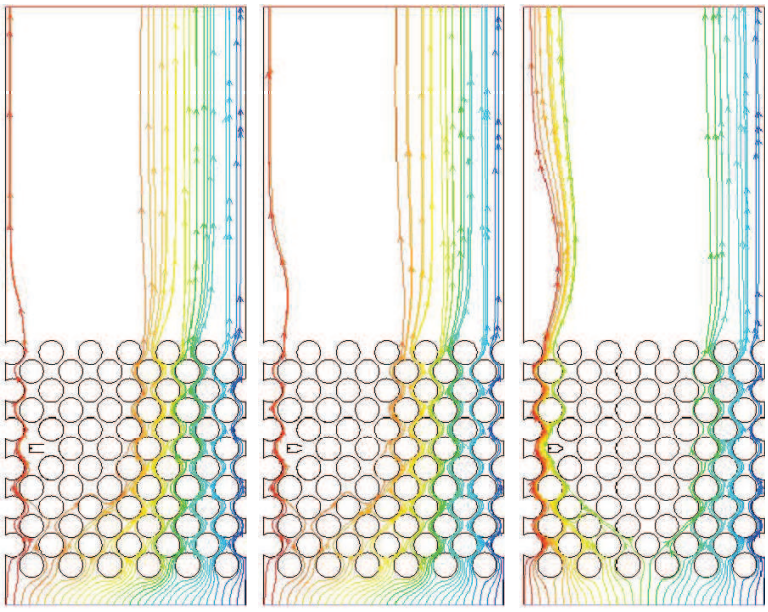

Figure 5.27: Comparison of the main stream pathlines in reacting flow

To show the difference in flow pattern in the unreacting flow simulation and the simulation of combusting flow, close views of the velocity vectors around the burner are displayed in Fig. 5.28 and Fig. 5.29. It is apparent to see the effective jet-induced mixing in the cold flow. In the combustion case, however, mixing does not occur due to the expansion of combustion gas. The spacial hindrance leads to reversed flows near the jet which prevent the cooling air being involved into the jet flow.

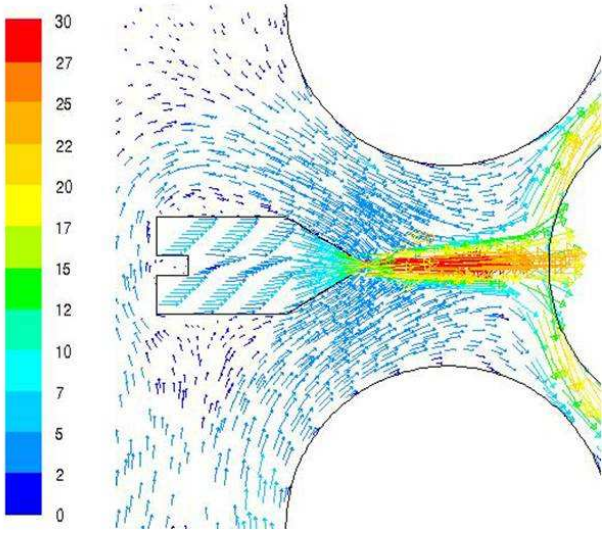

Figure 5.28: Close view of the velocity vectors near the burner (Geometry III, cold flow simulation), legend shows velocity in m/s

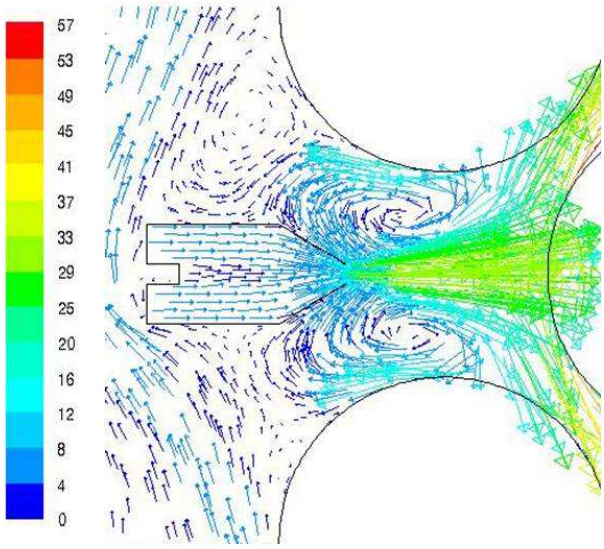

Figure 5.29: Close view of the velocity vectors near the burner (Geometry III, reacting flow simulation), legend shows velocity in m/s

Now that jet-induced mixing is a unique flow character of cold flow, what makes the difference from the simulation on Geometry III to that based on Geometry I and II?

Fig. 5.30 shows the velocity vectors in near-jet area in modelings with Geometry I and II. Comparing with flow structure depicted in Fig. 5.29, this figure manifests a big difference in the reversed flows. It is plain to observe that part of the reversed flows is pulled back due to the jet suction but most of them flow upward and do little contribution to the radial penetration. Fig. 5.27 shows that the main part of the reversed flows is cycling back when the burner outlet is smaller, and thereby the jet penetration is deeper.

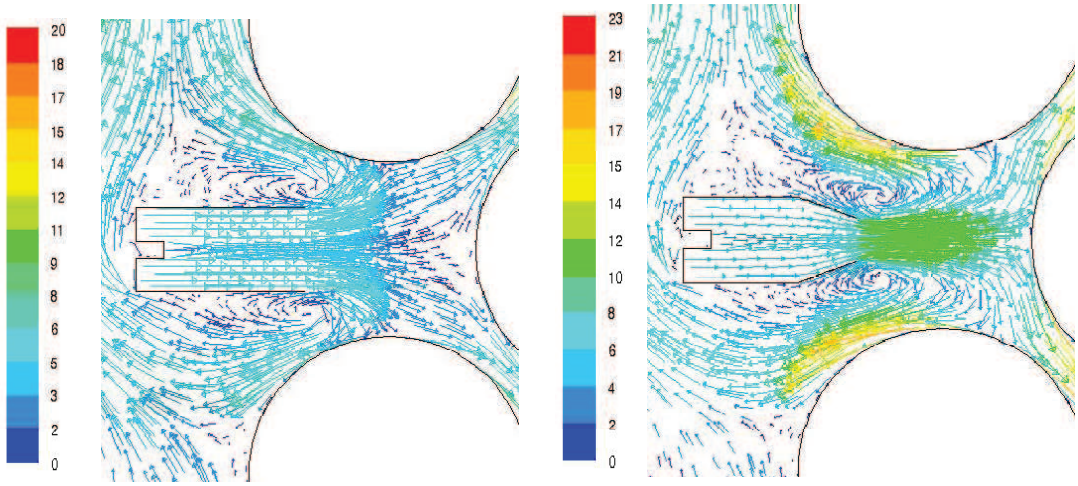

Figure 5.30: Close view of the velocity vectors near the burner (Geometry I and Geometry II), legends show velocity in m/s

Meanwhile, the change in the jet velocity by reducing burner outlet has great impact on the mixing of the fuel and combustion air, which leads to different rates of burning. The difference is depicted by comparing the mass fraction of CH_4 around the burner. As shown in Fig. 5.31, the concentration of methane is much lower in Geometry III indicating that a good mixing between CH_4 and combustion air due to the constriction of the burner outlet. As a result, this case has fast burning and therefore a short flame. This can be further proved by Fig. 5.32, in which the concentrations of CH_4 along Line 1 are plotted. The position of the peak concentration further shows that there is no obvious difference on penetration when the burner outlet is reduced from 30 mm to 15 mm. In this sense, we can say, the rate of combustion or the length of flame can be controlled by adjusting the dimension of the burner outlet, however, the corresponding effect on jet penetration can be neglected in the case of low jet velocity, for instance $v_j < 12m/s$.

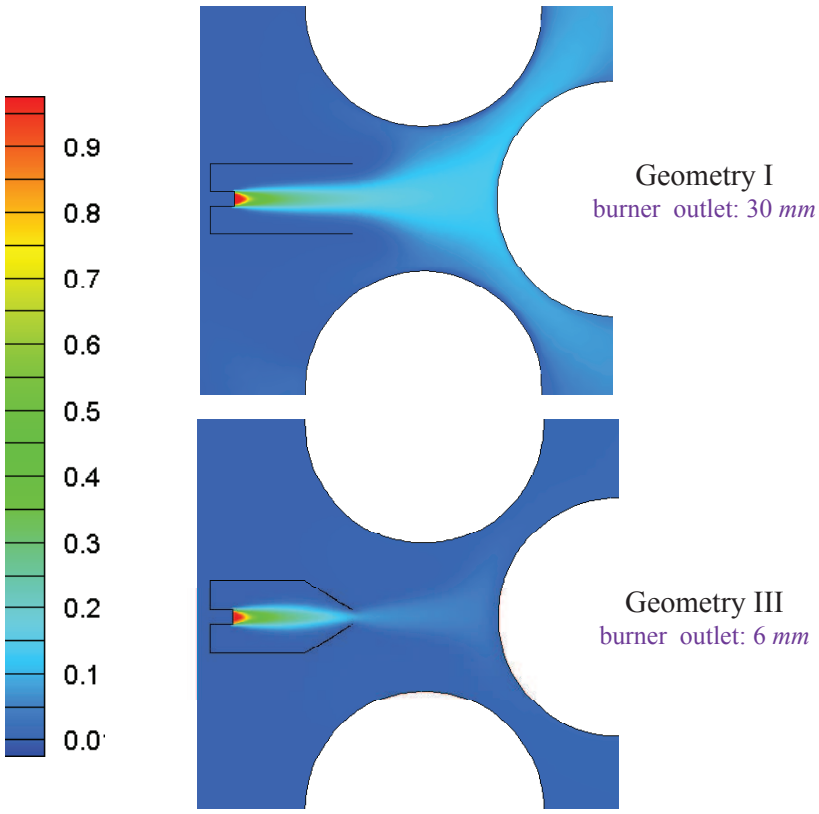

Figure 5.31: Close view of the mass fraction contours of CH_4 with different geometries

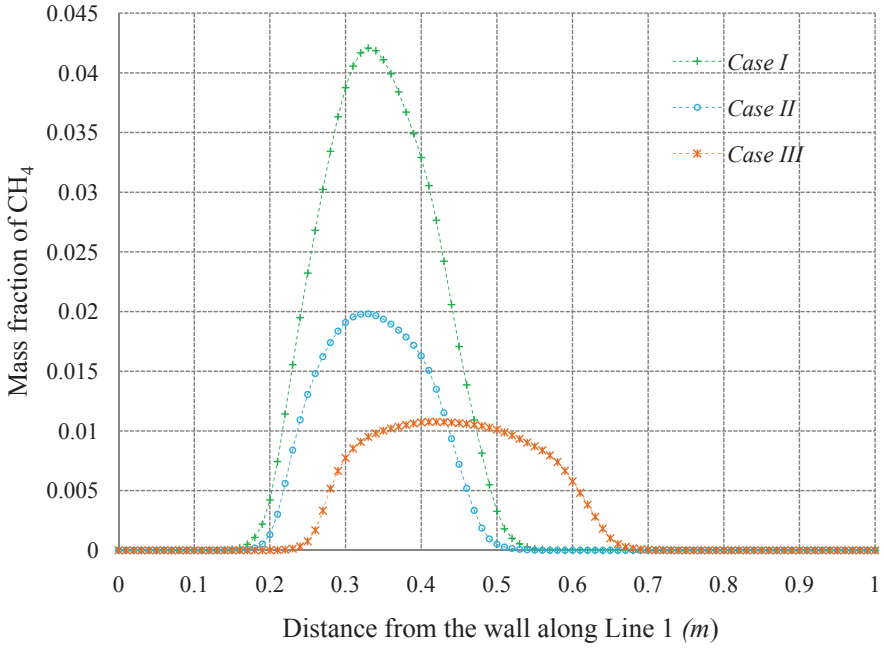

Figure 5.32: Concentration of CH_4 along Line 1

5.2.5 Effect of heat transfer and transient state on flow simulation

As described in Chapter 3, this work focuses on flow simulation in shaft kilns. The process is treated as steady state and, heat transfer from gas to solid is not considered to save computational efforts. However, this simplifications hypothesize that heat transfer between two phases has no or slight influence on the flow structures. In the following part, the effects are going to be discussed.

Models and boundary conditions

The geometric model of Case III is used as the prototype. The difference is that solid domain is introduced in this study. As can be seen in Fig. 5.33, around the burner solid domain with corresponding computational mesh is added. Material of the solid is Calcium carbonate ($CaCO_3$). The particle numbers are determined according to the flow characteristics without heat transfer to make the grid size as small as possible. In this case, the grid has approximately 140 thousand cells, i.e. about 40 thousand cells increased due to the presence of the solid domain.

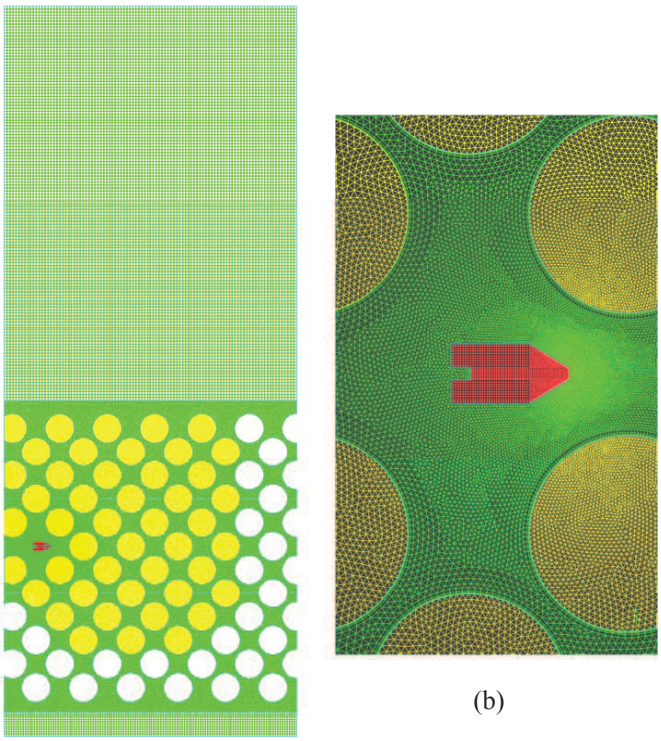

(a) (b)

Figure 5.33: (a) Geometry and mesh with solid domain, and (b) close view of the burner region

For the sake of comparison, boundary conditions listed in Table 5.5 are employed. Note that two-sided walls are generated between the solid and gas, and thermal boundary conditions at these walls are required for heat transfer calculation. To couple the fluid and solid, the *Coupled* option under *Thermal conditions*

is selected. Wall thickness is specified as zero so that there is no resistance from walls.

To calculate the transient heat transfer, the time step size is defined as 1 second in the first minute and increased to 5 seconds afterwards.

Simulation results

To demonstrate the influence of the transient, simulations are performed in a time-dependent manner and in steady state to compare. As a primary parameter, temperature distribution is used to illustrate the flow pattern. Fig. 5.34 and 5.35 present the temperature contours at 1 min, 15 min, 30 min, and steady state.

As can be seen from these figures, temperatures of both gas and solid are increasing with time till the steady state is reached. However, there are no visible changes in the flow pattern which is characterized by the temperature difference of combustion gas and cooling air. These results reveal that after being established the basic flow structures are independent of time and the temperature change of the gas and the solid. The increases in temperature cause the changes in density and consequently the changes in velocity, but have slight influence on the flow features, as shown in Fig. 5.36. Thus the flows can be solved in steady state instead of transient to check the jet penetration and the radial temperature distribution in the case that the absolute temperature is not the concern.

In some sense, the results above already prove that the flow pattern is independent of the heat transfer between the two phases. And this can be further confirmed by comparing the steady state simulations of the cases with and without the solid domain. Apparently, Fig. 5.37 shows no obvious difference in temperature distribution in the two cases.

As a result, flow simulations in steady state without considering the heat transfer of phases are reliable, which has great significance on simplifying the process modeling especially of three dimension.

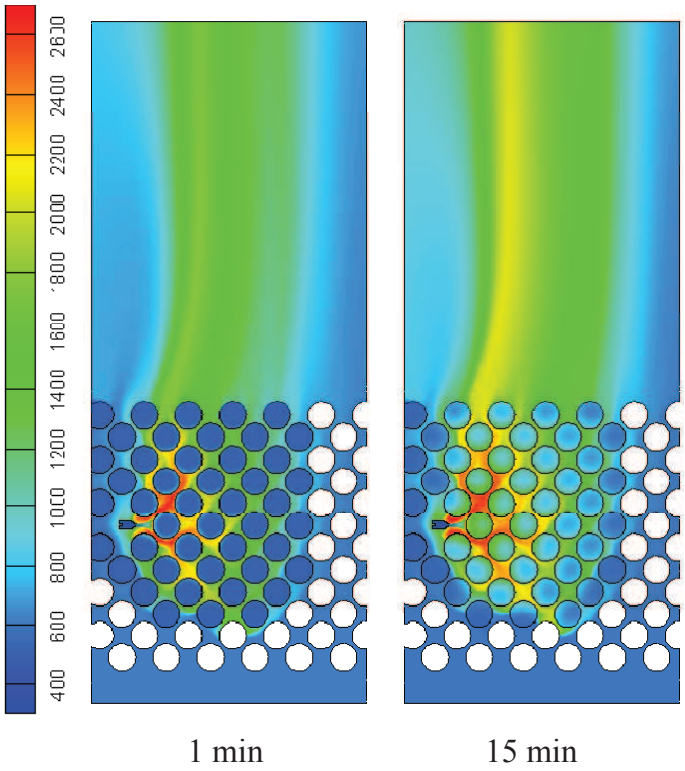

Figure 5.34: Temperature contours at 1 min and 5 min, legend shows temperature in K

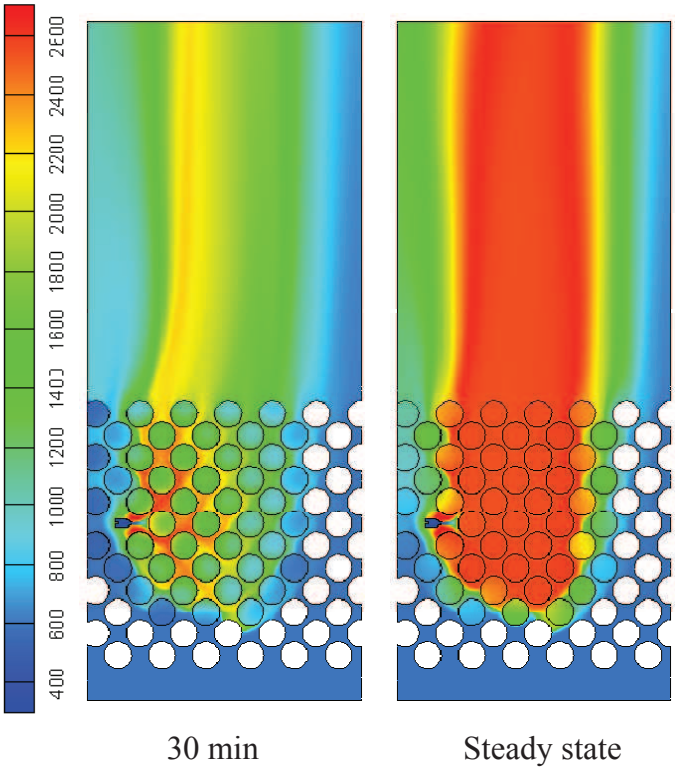

Figure 5.35: Temperature contours at 30 min and steady state, legend shows temperature in K

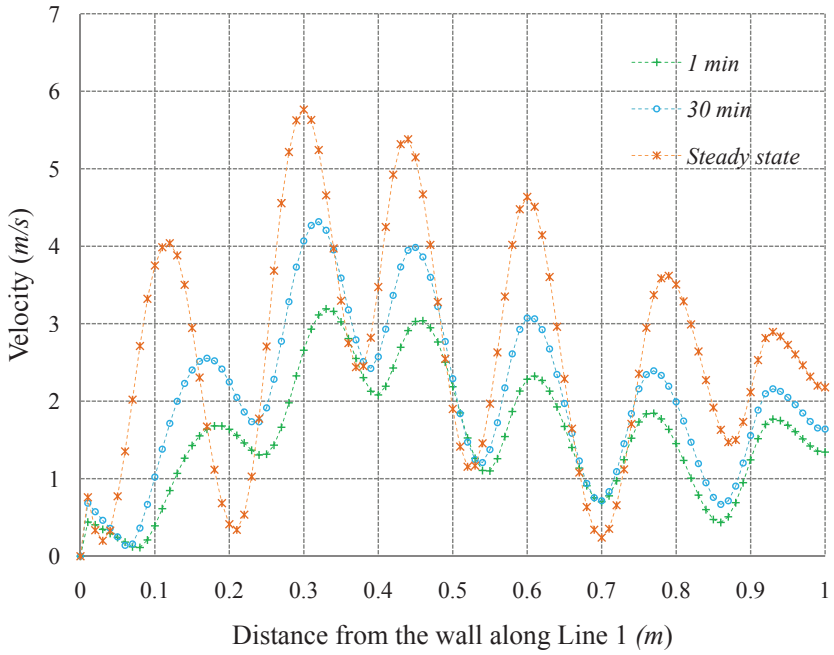

Figure 5.36: Velocity distributions along Line 1 with time

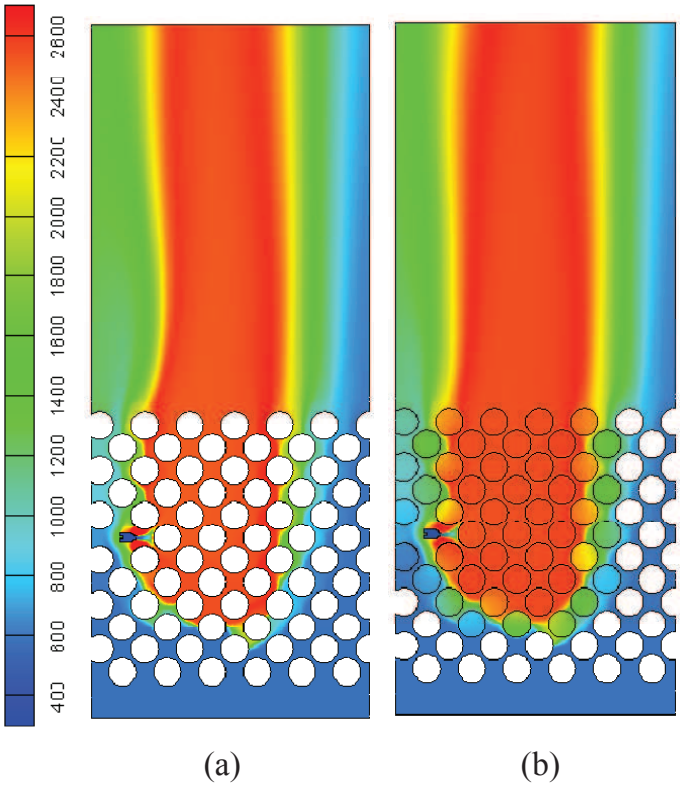

Figure 5.37: Comparison of temperature contours in cases with and without heat transfer from gas to solid, legend shows temperature in K

5.3 Case study

Based on the research presented above, the work of this section attempts to model the reactive flow in the lime shaft kilns. However, as the geometric model is still under developing and no industrial or experimental data are available, the primary aim of case studies is to gain some results which can be used to verify the viability of the 2-D modeling by comparing with 3-D simulations. Therefore, the current work has no intention to simulate any realistic case, and consequently the operating parameters may or may not follow the industrial operation.

5.3.1 Description of the kiln and model of the burner

The geometry is basically based on a type of RCE lime kiln, which is used for the production of basic and non-basic refractory products. The main features of the kiln is depicted in Fig. 1.11. However, the geometric model may not follow any of its original design.

One difference of this kiln from the others is that it is a high temperature shaft kiln. In case of gas firing, the mixing of gas and combustion air is accomplished within the burner lances by means of gas nozzles at each burner. Therefore, a new geometry of burner, with which the gas mixing is considered, is required. Fig. 5.38 shows the simple configuration of the geometry. As we assume that fuel and combustion air are perfectly mixed in the burner lance, the outlet of the lance is defined as the "inlet" through which the gas mixture is introduced into the kiln. The dimension of the inlet should be calculated in each case, while the length of the wall is flexible. Considering the special limitation of 2-D modeling, however, it can not be too long. In this study, it is fixed to 10 mm.

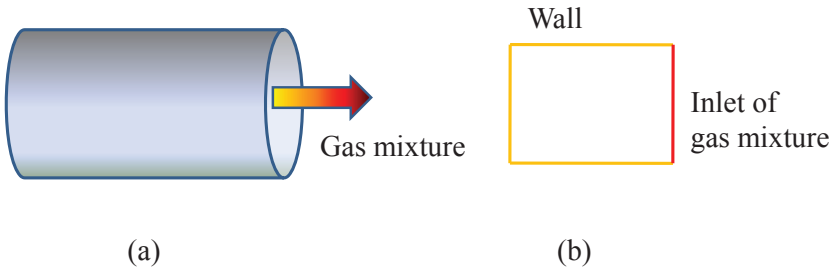

Figure 5.38: (a) The tip of the burner lance and, (b) the geometry for simulation

5.3.2 Basic calculations

Energy consumption and the fuel

To model the flow in shaft kilns, the energy consumption is an important parameter, based on which the fuel demand and air demand are calculated. The energy consumption, however, varies with different cases as it is a function of many factors, such as the type of fuel, output lime temperature, heat loss, excess air number, and so forth. The influence of these factors on the energy consumption of lime production is studied by A. Bes [9]. The value (4.0 MJ/kg_{lime}) is taken from her work. This value is calculated for natural gas L with assuming the heat loss through the wall of 170 kJ/kg_{lime}, the CO_2 concentration in the limestone of 42%, the residual CO_2 concentration of 0%, the lime discharge temperature of 80 ^oC, and the excess number of 1.3.

Table 5.6 shows the composition of the fuel, the air demand and net calorific value.

Table 5.6: Composition, air demand and net calorific value of nature gas L [9]

CH_4	C_2H_6	CO_2	N_2	$\tilde{L}$ (m^3_{air}/m^3_{fuel})	h_u (MJ/m^3)
0.82	0.04	0.01	0.13	8.5	31.4

Fuel demand and air input

As the type of fuel and energy consumption are determined and, the production capacity is known, the fuel demand can be calculated by the energy balance:

$$\dot{V}_f \cdot h_u = \dot{M}_L \cdot A \cdot Q \tag{5.6}$$

where $\dot{V}_f$ is the overall volume flow rate of fuel, $\dot{M}_L$ is the production capacity per area, A is the cross-section area of shaft kiln, and Q is energy consumption per kg lime production.

For this case study, the lime throughput is assumed to be 26.3 t/day/m^2 or 0.304 $kg/s/m^2$. The other operating parameters and corresponding fuel and air input are shown in Table 5.7.

In the table, R is the radius of the kiln, Ω is the mass flow ratio of cooling air to lime, $\dot{V}_{fa}$ is volumetric flow rate of combustion air, and $\dot{V}_{ca}$ is volumetric flow rate of cooling air.

Table 5.7: Calculations based on 26.3 t/day/m^2 lime production

R (m)	Ω	λ	$\dot{V}_f$ m^3/s	$\dot{V}_a$ m^3/s	$\dot{V}_{fa}$ m^3/s	$\dot{V}_{ca}$ m^3/s
1	0.6	1.2	0.122	1.236	0.445	0.791

5.3.3 Description of the cases

The kiln has 12 burners which have diameter of 0.07 m each and are horizontally situated in one or two levels. In the case that the burners are situated in one level, the burner lances protrude into the bed of material at the same depth. Therefore, in 2-D modeling there is only one horizontal burner, as shown in Fig. 5.39 (a). Simulations based on cases with different lance depth are performed to investigate the effect of lance depth on radial temperature distribution.

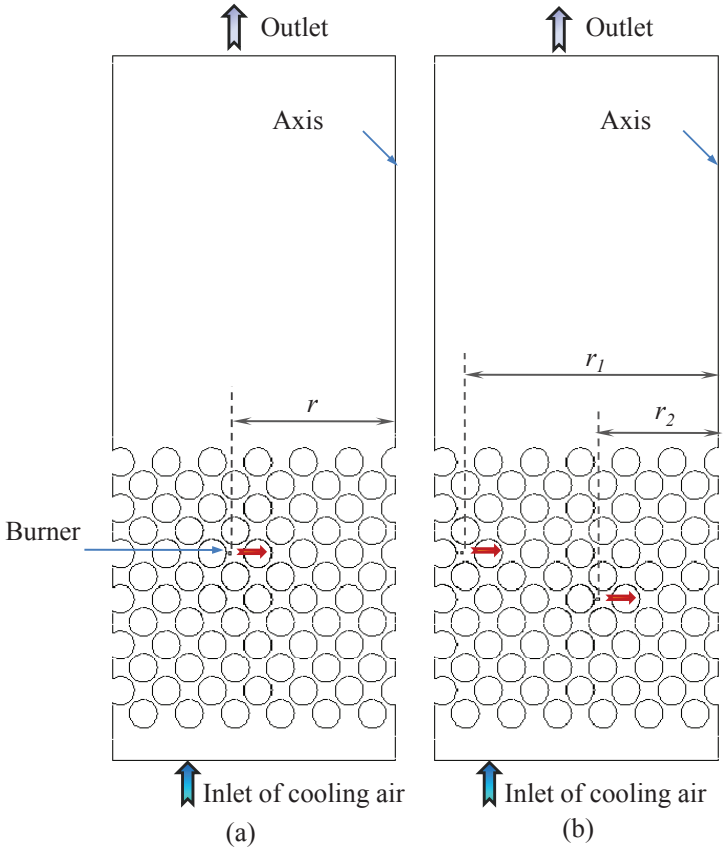

Figure 5.39: (a) 2-D geometry with one burner lance, (b) 2-D geometry with 2-level burner lances

In the other case, i. e. the burners are situated in two levels, the burner lances protrude into the bed at the same depth on the same level but at the different depths between the levels. Accordingly, in 2-D modeling two horizontal burners are required with each representing one level of burners, as depicted in Fig. 5.39 (b). As the fuel and combustion air are introduced from two levels, the volumetric flow ratio between the two levels ($\dot{V}_{f1}/\dot{V}_{f2}$) needs to be determined to

obtain optimal temperature distribution over the cross section. Here $\dot{V}_{fm}$ is the volume flow rate of fuel mixture (fuel and combustion air) and, the number denotes the burner level. For a fixed arrangement of burners, the influence of volumetric flow ratio is studied.

In the 2-D geometry, the dimension of the burner is extremely small so that the outlet velocity of the fuel mixture (mixture of the fuel and combustion air) can be the same as that in 3-D. This is because the influence of jet velocity on the flow structures can not be neglected in the case $v_j > 12m/s$, as discussed in the general study. The width of the burner outlet can be calculated by Eq. 3.3. Table 5.8 and Table 5.8 show the location and the width of the burners in each case. In

Table 5.8: Depth of the burner lance and its width (1-level burner system)

Case	r (m)	Depth $(R-r)$ (m)	h (m)
I	0.9	0.1	0.0082
II	0.68	0.32	0.0112
III	0.5	0.5	0.0148

the table, r is the distance from the burner outlet to the center of the kiln and h is the width of the burner outlet.

Table 5.9: Depth of the burner lance and its width (2-level burner system)

r (m)		Depth (m)		$h(m)$	
L-1	L-2	L-1	L-2	L-1	L-2
0.9	0.42	0.1	0.58	0.0062	0.0044

In Table 5.9, L-1 and L-2 indicate burners on the level 1 and level 2.

For 2-level burner system, simulations are performed based on 3 cases (Case IV, V, and VI). In these three cases, the volumetric flow ratio ($\dot{V}_{fm1}/\dot{V}_{fm2}$) is 5.5, 4.0, and 3, respectively.

5.3.4 Model definition and boundary conditions

Turbulence flow is assumed in the calculations. The standard κ-ϵ model with enhanced wall treatment is applied. As the combustion air and the fuel are premixed in the burner lance(s) and, the cooling air is introduced as the secondary oxidant, *partial premixed model* is used to model the combustion. Considering that a large amount of heat released in combustion which has profound impact on the solution stability, the relaxation factors for density, momentum and temperature etc. are reduced to facilitate convergence. The under-relaxation factors for some variables are shown in Table 5.10.

The default under-relaxation factors are set to the other variables.

Table 5.10: Under-relaxation factors for the computing variables

Density	Momentum	κ	ϵ	Temperature	Progress variable	Mixture fraction variance
0.6	0.5	0.8	0.8	0.7	0.8	0.8

As for the boundary conditions, cases differ each other only at inlet of fuel mixture ($Inlet_{fm}$) in hydraulic diameter for Case I to IV and in velocity for Case V to VI. Table 5.11 shows the setup at $Inlet_{fm}$ for each cases. Boundary conditions at the outlet of flue gas ($Outlet$) and the inlet of cooling air ($Inlet_{ca}$) are the same and listed in Table 5.12. The walls are specified as no-slip condition with heat flux zero.

Table 5.11: Boundary conditions at $Inlet_{fm}$ for each case

Case \ Parameter		v (m/s)	D_h (m)	I (%)	T (K)	$\bar{c}$	$\bar{f}$	$\bar{f'^2}$
I		29.2	0.0164	10	400	0	0.0887	0
II			0.0224					
III			0.0298					
IV	L-1	33.1	0.0124					
	L-2	17.52	0.0088					
V	L-1	31.92	0.0124					
	L-2	21.02	0.0088					
VI	L-1	29.2	0.0124					
	L-2		0.0088					

Table 5.12: Boundary conditions at $Inlet_{ca}$ and $Outlet$ for all cases

	v (m/s)	D_h (m)	I (%)	T (K)	$\bar{c}$	$\bar{f}$	$\bar{f'^2}$
$Inlet_{ca}$	0.415	2.0	10	800	0	0	0
$Outlet$	-	2.0	10	300	0	0	0

5.3.5 Results and discussions

Temperature distribution Vs. lance depth

Fig. 5.40 to 5.42 show the temperature contours with different burner lance depths. It can be noted that when the lance is too close to the wall, the flow pattern is characterized by under-penetration and a "cold core" is formed. In Case II, with a deeper lance depth the kiln is slightly under-penetrated and, after

the full expansion of the combustion gas the "cold core" is diminished, as shown in Fig. 5.41. While when the lance depth reaches 0.5 m (Case III), the kiln is over-penetrated.

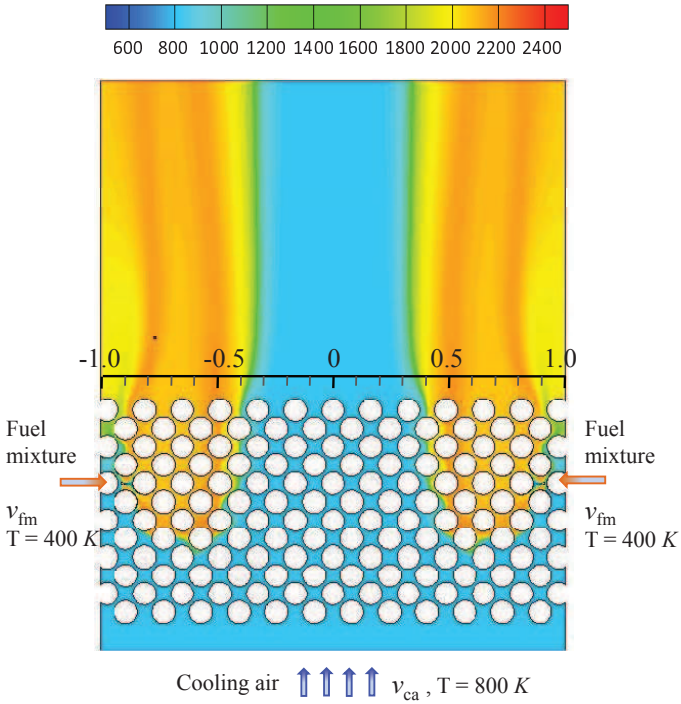

Figure 5.40: Temperature contours for Case I (lance depth = 0.1 m, $v_{fm} = 29.2m/s$, $v_{ca} = 0.415m/s$); Legend in K

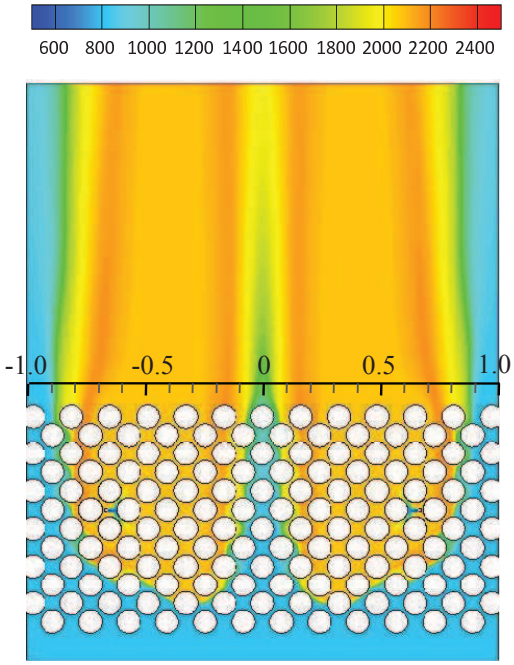

Figure 5.41: Temperature contours for Case II (lance depth = 0.32 m, $v_{fm} = 29.2m/s$, $v_{ca} = 0.415m/s$); Legend in K

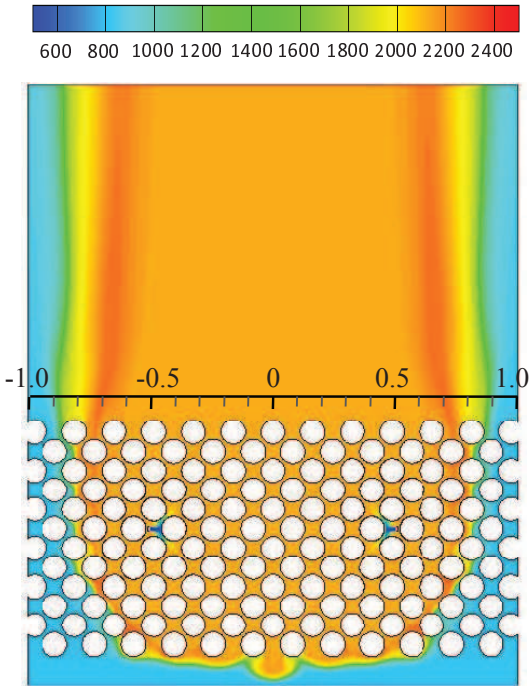

Figure 5.42: Temperature contours for Case III (lance depth = 0.5 m, v_{fm} = $29.2m/s$, $v_{ca} = 0.415m/s$); Legend in K

The influence of the lance depth on the radial temperature distribution can also be quantitatively studied. From Fig. 5.43 we may calculate approximately

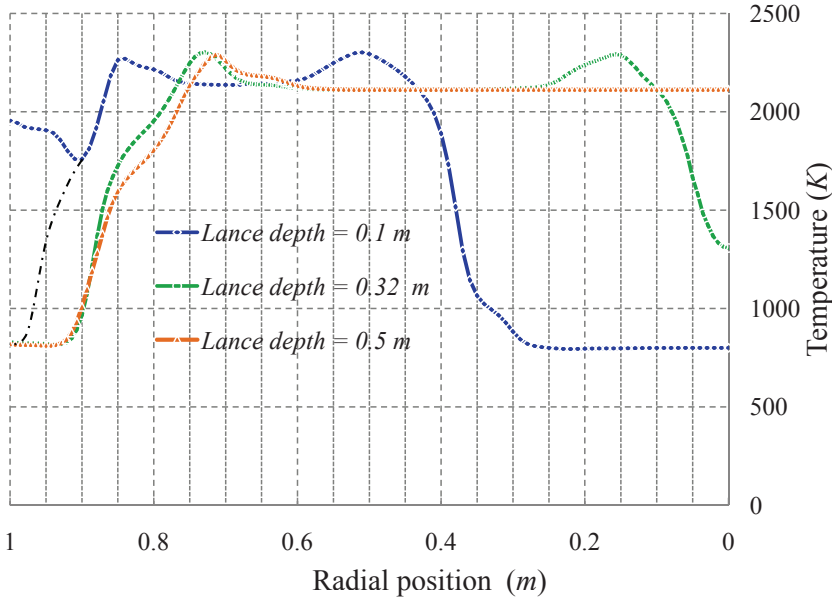

Figure 5.43: Comparison of radial temperature distribution along $x = 1.15m$

the percentage of the effective penetration area. If we define the position of 1000 K as the front of the penetration of the combustion gas, it is easy to find that the rate of the effective area over the cross section is 81% in Case II and III. In Case I (Lance depth is 0.1 m), it′s around 88%. However, it is mostly due to the special geometry near the wall. Without this effect, the temperature profile may follow

the trend, the dot-dash line shown in Fig. 5.43, and the percentage would be close to 81%. The result comes no surprise as the gas mixing is so poor that the flow area ratio of the combustion gas to the cooling air is certainly constant. Therefore, by adjusting the lance depth the radial temperature profile can be changed but the efficiency of the firing system is hardly possible to be improved. In spite of that, slight under-penetration or slight over-penetration may have advantage considering the protection of the wall (refractory) from over heating and heat loss through the wall to the environment as more cooling air flows upwards along the wall.

Distribution of the fuel mixture for two-level burners

In the case that the burner lances are situated at two levels with different depths, the distribution of the fuel mixture to each level can be determined once the location of lances is fixed. The fraction of the fuel mixture introduced from each level can be quantitatively studied as well by means of radial temperature distribution.

In Case IV, V, and VI, burners are arranged in two levels. The first level is located with a lance depth of 0.1 m, and the lance depth of the second one is 0.52 m. The fraction of the fuel mixture introduced from the second-level burner lance (with deeper location) is 15%, 20% and 25%,respectively. That is to say, the volumetric flow ratio of the first burner and the second one ($\dot{V}_{fm1}/\dot{V}_{fm2}$) is approximately 5.5, 4.0, and 3.0, respectively. The temperature contours in each case are displayed in Fig. 5.44 to 5.46. As observed in Fig. 5.44 to 5.46, at

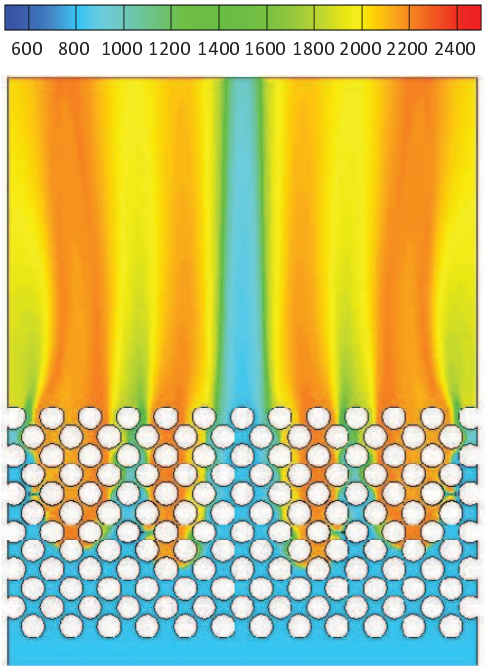

Figure 5.44: Temperature contours for Case IV, ($\dot{V}_{fm1}/\dot{V}_{fm2} = 5.5$, $v_{fm1} = 33.1m/s$, $v_{fm2} = 17.52m/s$); Legend in K

$\dot{V}_{fm1}/\dot{V}_{fm2} = 5.5$, the bed is slightly under-penetrated. When 20% of the fuel is

introduced from the second burner, the "cold core" is eliminated, while the ratio further increases to 25% the bed is over-penetrated.

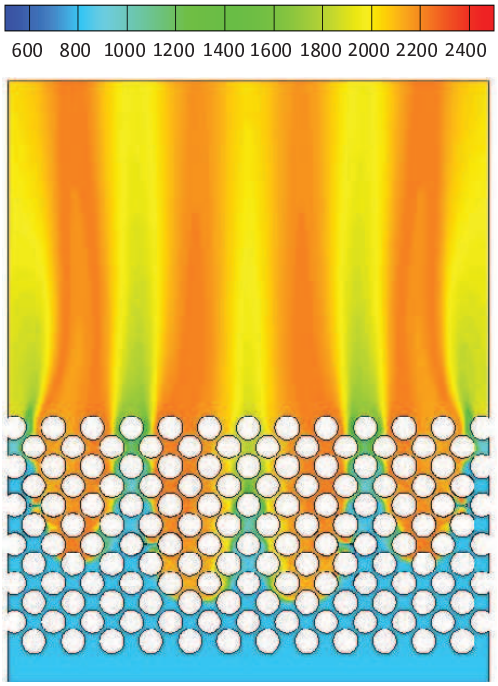

Figure 5.45: Temperature contours for Case V, $\dot{V}_{fm1}/\dot{V}_{fm2} = 4.0$, $v_{fm1} = 31.92m/s$, $v_{fm2} = 21.02m/s$); Legend in K

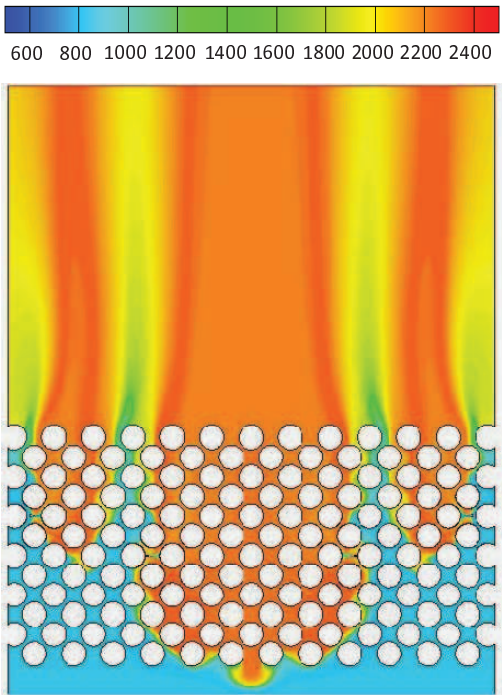

Figure 5.46: Temperature contours for Case VI, $\dot{V}_{fm1}/\dot{V}_{fm2} = 3.0$,$v_{fm1} = 29.2m/s$, $v_{fm2} = 29.2m/s$); Legend in K

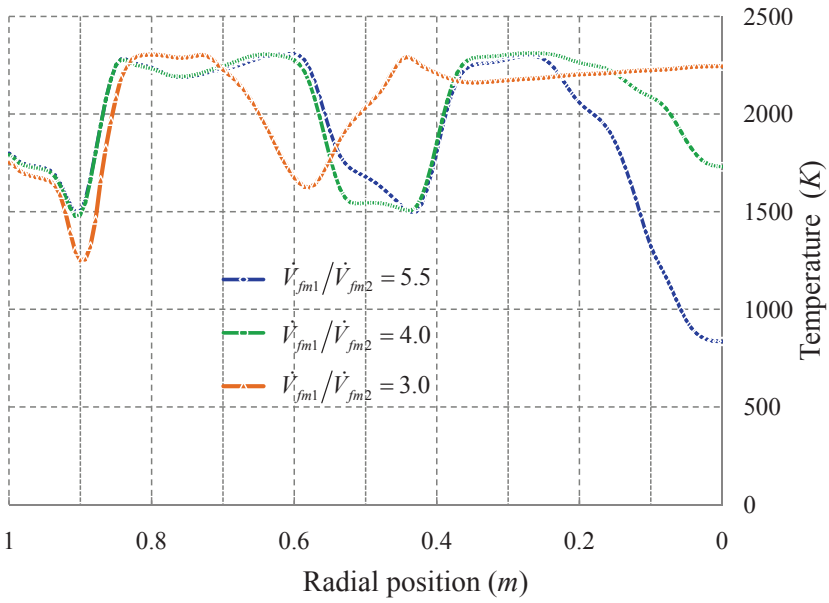

Figure 5.47: Comparison of radial temperature distribution along $x = 1.15m$

Compared with one burner case (results see Fig. 5.43), Fig. 5.47 shows a much better radial temperature distribution, particularly in the case $\dot{V}_{fm1}/\dot{V}_{fm2}$ = 4.0. As can be seen, nearly 100% of the cross-sectional area is covered by hot temperature gas (above 1500 K).

However, as the influence of the third dimension is not clear, it might be not sufficient enough to optimize any existing system by performing 2-D simulations. Therefore, the main purpose of this case study is to demonstrate the viability of the CFD modeling while without intention to provide specific optimal operation parameters. Regarding to this point, the data obtained above may or may not have any referential value for design.

5.4 Summary

2-D flow modeling is performed in this chapter. Simulations are firstly carried out as "cold flow" to study the general jet behavior in cross flow in packed beds. Results show that the flow structures in the jet region are independent of the bed height and, jet velocity has profound impact on jet penetration due to the jet-induced gas mixing. Then combustion is introduced to investigate the modeling of reactive flows. Unlike the behavior in the cold flow, jet-induced gas mixing does not occur owning to combustion, which results in poor gas mixing between the combustion gas and the cooling air. Meanwhile, the influence of the transient heat transfer from gas to solid on the flow structures is studied. As expected, the heat transfer impacts the gas temperature strongly while only has slight effect on the distribution of flow fields. According to these results, the flow modeling of shaft kilns can be simplified significantly. Some case studies are conducted in the final section of this chapter. Results reveal that good radial temperature distribution can be achieved when the burner lances are situated at different lance depths. The

viability of CFD modeling is tested with different 2-D geometries and boundary conditions.

Chapter 6

3-D flow Simulations of Shaft Kilns

This chapter is devoted to present 3-D simulations. In contrast with 2-D simulations, 3-D geometric models are more realistic on modeling the spheric particles and tube shaped burners. However, as discussed in Chapter 4, one of the biggest challenge is that the computational grids are large and thereby great computational efforts are required. To save computational time and make the results comparable with 2-D modeling, the diameter of the kiln and the particle is restricted to 2 m and 0.1 m respectively in this work. In the case that much bigger industrial kilns are being modeled, parallel processing is available in FLUENT. Therefore, the simulations performed in this chapter mainly present a general study on the behavior of the burning jets and the cooling air in lime shaft kilns and attempt to testify the viability of the 3-D model, while have no intention of finding an optimal firing arrangement for a specific case.

Additionally, "porous media model" is used in the last section of this chapter. The advantages and disadvantages of this model are demonstrated by comparing with the simulations based on "discrete particle model".

6.1 Description of the geometry and the grid

As mentioned in Chapter 3, in which the development of the geometry has been discussed in detail, the 3-D geometric model is a reduced segment model. The bed height is kept as short as possible thanks to the independence of the jet (flow) behavior on the packing height, and further only a bed segment with a certain angle is modeled by taking advantage of the flow symmetry. As shown in Fig. 6.1, the overall height of the geometry is only 1 m and the packing height is around 0.8 m. One thing to be mentioned is that the geometry is divided into three subdomains by two interior faces. The outlet domain is very short comparing with 2-D geometry in order to save computational time. However, this will lead to reversed flow on outlet and influence the flow structures in the packing area. To solve this problem, the outlet domain must be defined as a porous zone. The

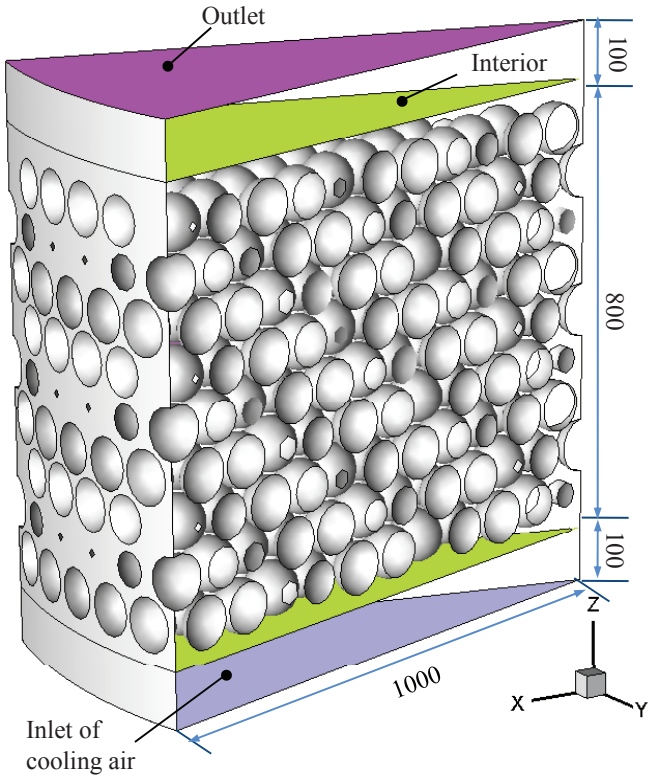

Figure 6.1: Isometric view of the 3-D geometric model

porosity, viscous and inertial resistance can be specified as any values as long as reversed flow can be avoided. In this study, the viscous and inertial resistance are defined as 168000 $1/m^2$ and 326 $1/m$ respectively, and the porosity is set as 0.4.

The firing system of the RCE lime kiln consists of 12 burner lances which are horizontally situated in 1 or 2 levels and divide the kiln into 12 identical sections; therefore, a 30^o segment is assumed to be sufficient. In Fig. 6.2, lines 1 to 4 indicate the symmetry faces of the geometries. The location of the burner(s) is shown in Fig. 6.3 and 6.4.

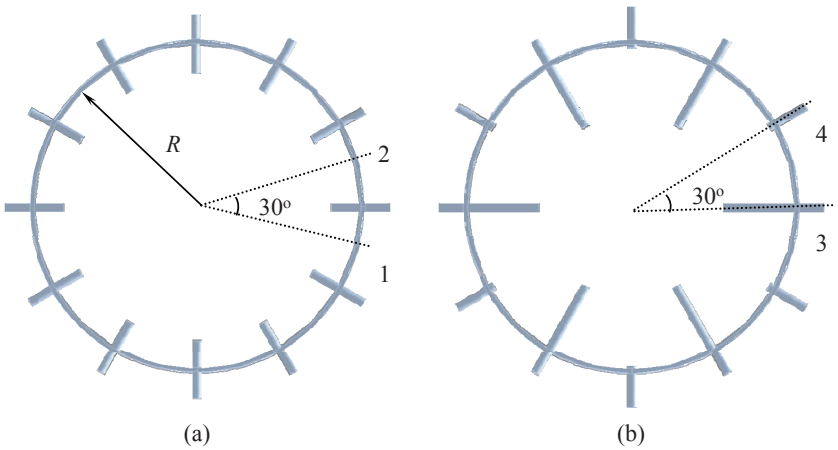

Figure 6.2: Top view of burner lances: (a) one-level arrangement, and (b) two-level arrangement (lance depth differing between levels)

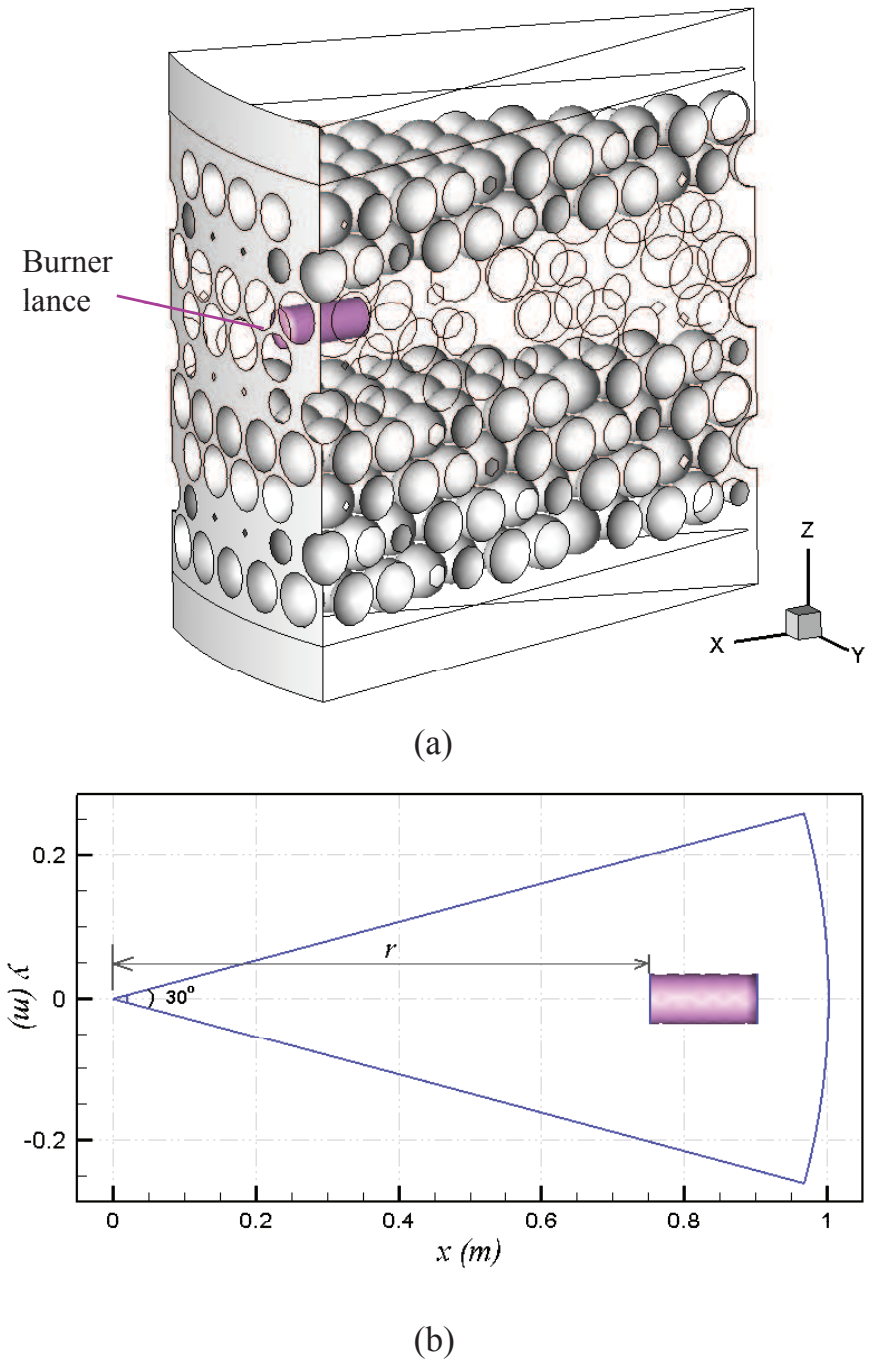

Figure 6.3: (a) Transparent view and (b) top view of the burner in the case of one-level arrangement

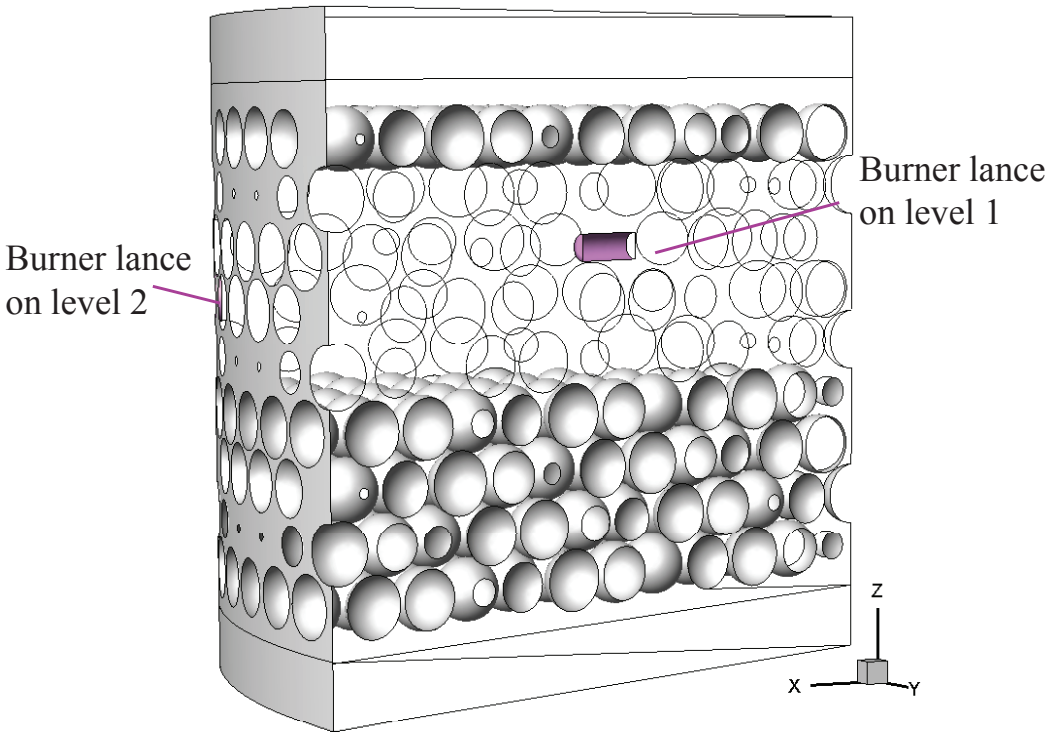

(a)

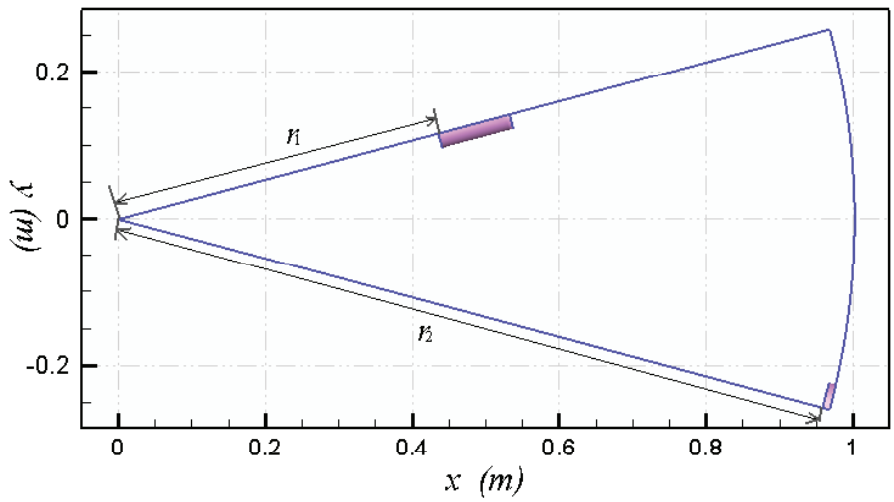

(b)

Figure 6.4: (a) Transparent view and (b) top view of the burners in the case of two-level arrangement

According to the grid convergence study in Chapter 4, and particularly considering the interests of this work, a relatively coarse grid is selected for computation. To decrease the computational efforts as much as possible, structured element is used for the inlet and outlet domain, and the normal mesh instead of the graded mesh is generated related to the packing domain as the gap between particles is pretty large for a void fraction of 0.4. Meshing is firstly performed to the packing domain with interval size of 0.6 mm and then, the mesh node patterns are projected through the inlet and outlet domain by means of cooper meshing scheme. Consequently, two types of grids are used, prism for the inlet and outlet domain and tetrahedron for the packing body. Fig. 6.5 and 6.6 depict the grid patterns on the face of outlet domain and the particles. The 3-D computational grid consists of about 2 million cells in all. The mesh file is around 220 MB.

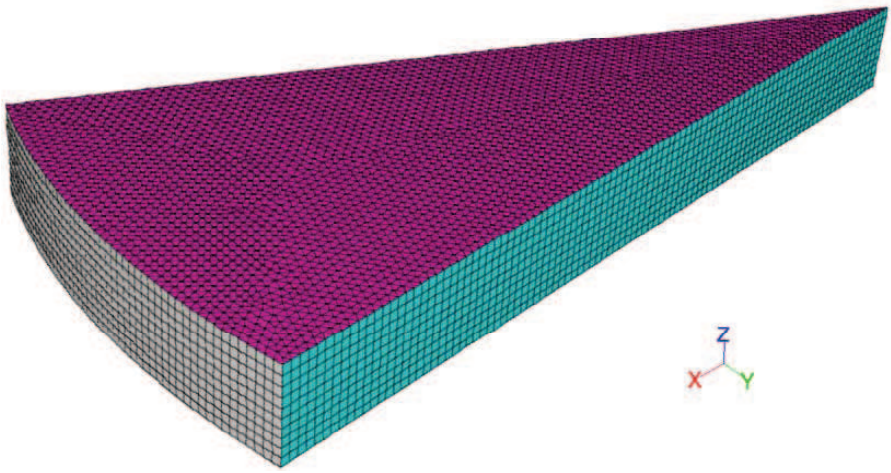

Figure 6.5: Prism grid for inlet and outlet domain

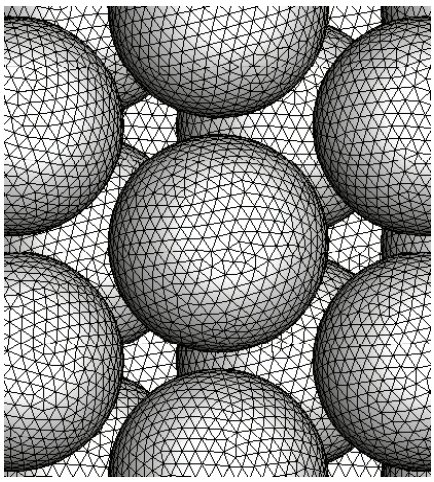

Figure 6.6: Unstructured grid pattern on the face of particles

6.2 Definition of the simulation models and materials

Turbulence flow is assumed in the calculations and the standard κ-ϵ model with standard wall function is applied. As the fuel and combustion air are premixed in the burner lance and the cooling air is supposed to be the secondary combustion air, *partial premixed model* is used to calculate combustion. Given that the grid is relatively coarse, the first order upwind schemes are selected to compute the field variables. The SIMPLE is used for the pressure-velocity coupling algorithm. To increase stability, relaxation factors of some transport variables are reduced, as shown in Table 6.1. The relaxation factors of the other variables are set as the default values. The fuel is natural gas L which is presented in Table 5.6. The fuel

Table 6.1: Under-relaxation factors for the computing variables

Density	Momentum	Temperature	Progress variable	Mixture fraction variance
0.5	0.5	0.7	0.7	0.7

demand, air demand, and the mass flow ratio of cooling air to lime are as the same as the calculation in Chapter 5 Table 5.7.

6.3 Simulations and results

In this section, simulations are performed to investigate how to improve the radial temperature distribution in a lime kiln. Studies mainly focus on some important factors, such as the lance depth, the dimension of the burner lance, the arrangement of the burners, and the preheating of the fuel mixture etc.

6.3.1 Influence of lance depth

The boundary conditions, listed in Table 6.2, are calculate from the fuel and air demand obtained in the case study in Chapter 5. One may notice that the hydraulic diameter of the outlet and the inlet of cooling air is not the diameter of the kiln, i.e. 2 m, but 1.02 m. This is the result of the symmetric structure. The vertical cross sections are defined as symmetry while not periodicity due to irregular structure. Therefore the 30^o segment model represents a 120^o entity in FLUENT and accordingly the hydraulic diameter should be computed from the definition

$$D_h = 4A/P \tag{6.1}$$

where A is the cross sectional area and P is the wetted perimeter.

Table 6.2: Inlet and outlet boundary conditions

		D_h (m)	I (%)	Velocity (m/s)	Temperature (K)
Inlet	fuel mixture	0.07	10	29.2	400
	Cooling air	1.02	10	0.415	800
Outlet		1.02	10	-	300

Simulations are performed in two cases with different lance depths while keeping the other operating conditions being the same. In Case I, r is 900 mm, i.e. the lance depth, defined as $R - r$, is 100 mm. In Case II, the lance depth is 200mm. For both cases, the diameter of the burner lance is 70 mm.

Compared to 2-D calculation, the computational time of the 3-D simulations increases drastically. Each computation takes around 2000 iterations and more than 50 hours to reach the converged solution. The computational time includes the data transfer time from the server to the local workstation.

Fig. 6.8 compares the temperature distribution between the two cases. As we can see, the kiln is under-penetrated with a lance depth of 100 mm. In this case, the cooling air is divided into two streams by the combustion gas and consequently, a "cold core" and a low temperature region along the wall are formed. With the burners put 100 mm further into the loading, the combustion gas reaches the center. As a result, the "cold core" is no longer the problem. However, the low temperature region near the wall is enlarged as most of the cooling air flowing to the wall. This is more clearly displayed by comparing the top views of the temperature contours , as shown in Fig. 6.9.

To calculate and compare the area percentage of the combustion gas in the two cases, the mean temperature on the plane of $z = 0.9m$ in radial direction is plotted accordingly in Fig. 6.10. As can be approximately calculated , the area of the temperature above 1000 K takes up 90% of the cross-sectional total in both cases. Like the conclusion drawn in 2-D simulations, the overall radial temperature distribution is independent on the lance depth. Compared with the 2-D simulations,however, the percentage of the area is about 10% bigger. This difference indicates that mixing between the fuel and the cooling air happens to some degree.

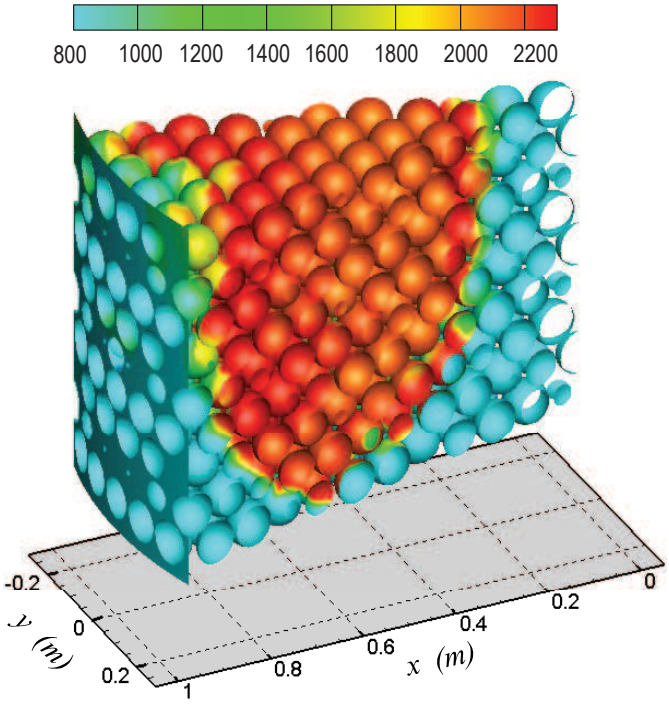

Figure 6.7: Temperature contours on the surface of particles of Case I (Lance depth = 100 mm); Legend shows temperature in K

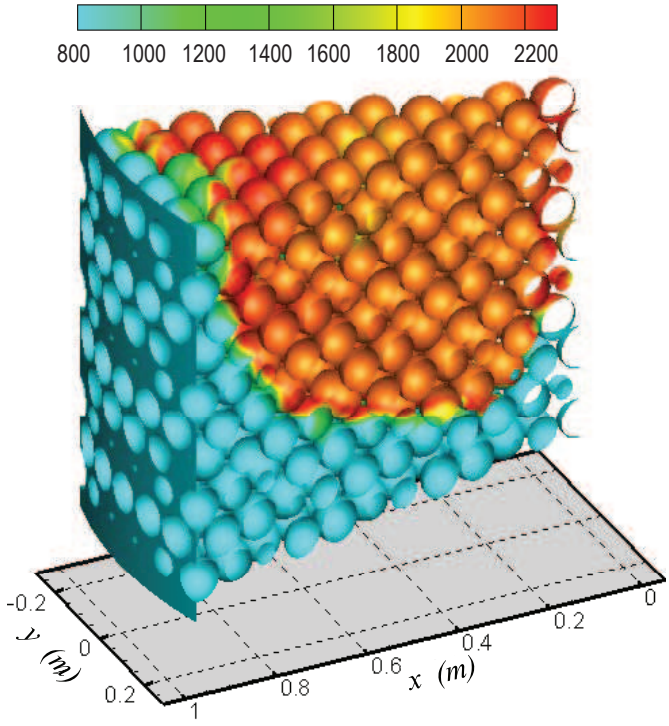

Figure 6.8: Temperature contours on the surface of particles of Case II (Lance depth = 200 mm); Legend shows temperature in K

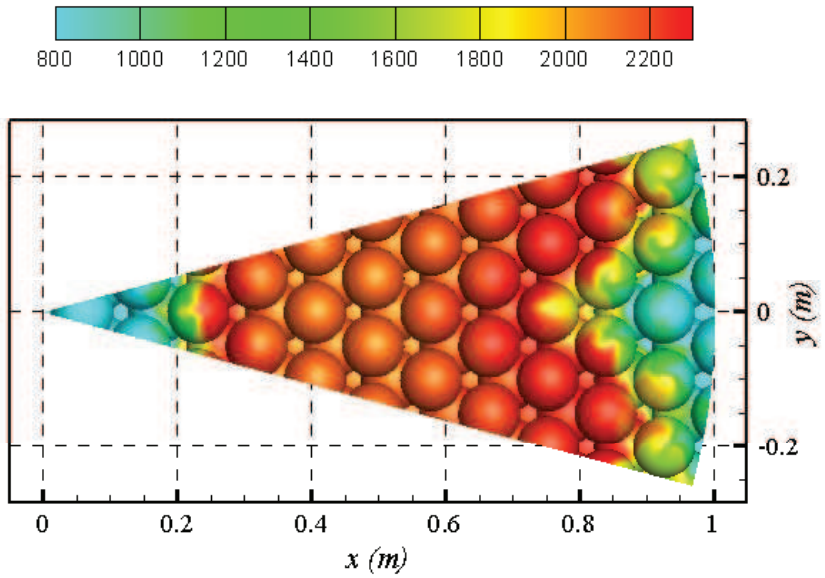

Lance depth = 100 *mm* (Case I)

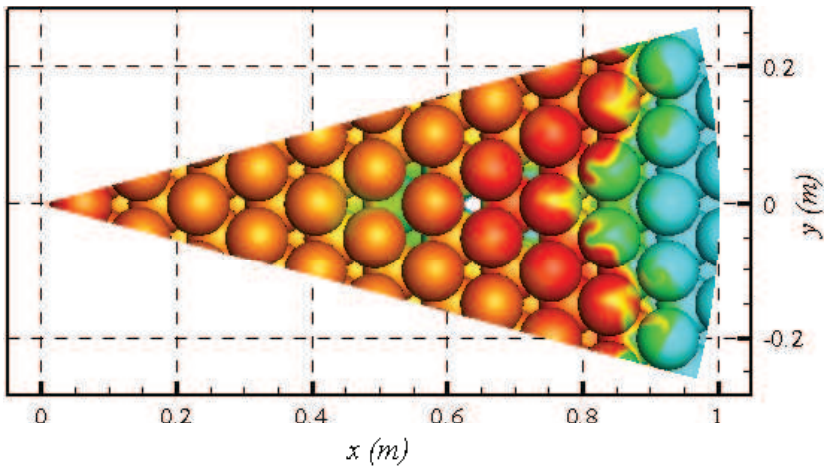

Lance depth = 200 *mm* (Case II)

Figure 6.9: Top views of the temperature contours with different lance depths; Legend shows temperature in K

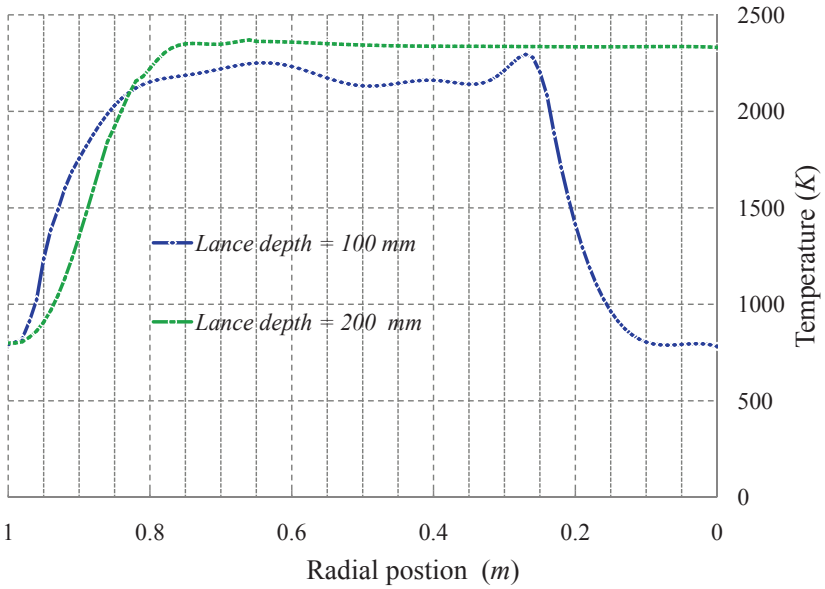

Figure 6.10: Profiles of the mean temperature on the plane of $z = 0.9m$ in x-direction

It is plain to observe that some cooling air is pulled into the fuel jet. That is why the area ratio increases around 10% in comparing to the 2-D simulations. And, correspondingly, the 3-D jet penetration is relative deeper, see Fig. 5.40 and Fig. **??** for comparison. Therefore, the effect of the third dimension can not be ignored especially when the radial penetration depth is considered.

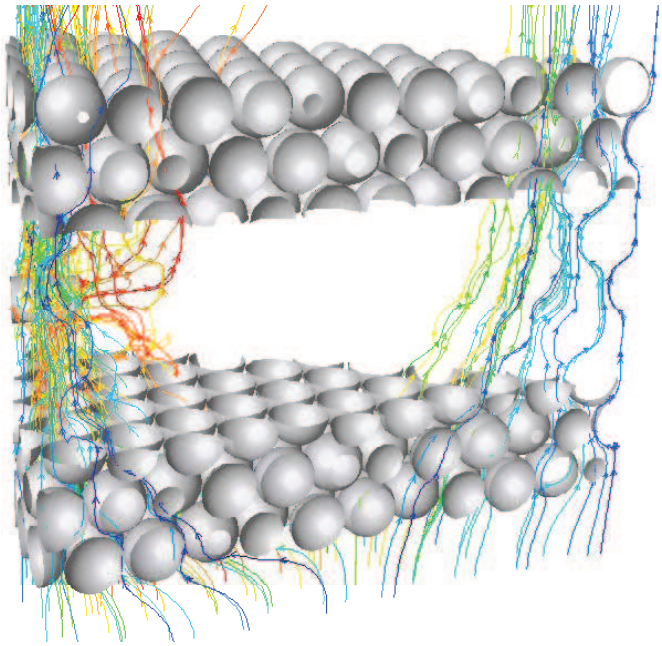

Figure 6.11: Pathlines released from the inlet of the cooling air for Lance depth = 0.1 m and $v_{fm} = 29.2m/s$

6.3.2 Influence of burner diameter

Based on the research presented above, we know that to improve the overall radial temperature, mixing between the fuel (mixture) and the cooling air which serves as the secondary combustion air is the key issue. One way to improve the mixing efficiently is by taking advantage of the jet-induced circulation. By this way, of course, high jet velocity is required. As observed in the previous subsection, the jet-induced mixing plays a very weak role even in the case with a jet velocity of 29.2 m/s. In 2-D modeling, it is hard to further increase the jet velocity by reducing the dimension of the burner as it is already extremely small. For instance, to reach the normal velocity of 29.2 m/s the width of the burner inlet is 0.0082 m with lance depth of 0.1 m. With 3-D geometric model, this is no longer the challenge. The diameter of the burner is reduced from 0.07 m to 0.05 m for investigation.

This case (Case III) is supposed to compare with Case I, thus the geometry is exactly the same as that deployed in Case I except the reduction of the burner diameter. The boundary conditions at the inlets and outlet are shown in Table 6.3.

Table 6.3: Inlet and outlet boundary conditions for Case III

		D_h (m)	I (%)	Velocity (m/s)	Temperature (K)
Inlet	fuel mixture	0.05	10	57.2	400
	Cooling air	1.02	10	0.415	800
Outlet		1.02	10	-	300

Simulation results are displayed by means of the temperature contours. As observed in Fig. 6.12, when the velocity of the fuel mixture is increased from 29.2 m/s to 57.2 m/s, the effect is obvious. The bed is penetrated and furthermore, comparing to the top view of the temperature contours shown in Fig. 6.9 we can find that the temperature profile near the wall is very like that of Case I. That is to say, the radial gas mixing is improved.

The path of the cooling air is visualized to illustrate the the jet-induced mixing. Fig. 6.13 displays the pathlines released from the inlet of the cooling air. It can be seen that, the amount of cooling air being sucked into the fuel stream increases significantly in comparing with Case I (see Fig. 6.11). The improvement in the gas mixing leads to a better radial temperature distribution in the bed. As far as burner design is concerned, however, it must be mentioned that higher jet velocity means higher pressure loss, i.e. higher pressure is required for the blower system. Thus the design becomes an economic balance between the extra cost required by high pressure transport and introduction of more burner lances. Additionally, the stability of the flame should be taken into considered as well in the cases of premixed combustion.

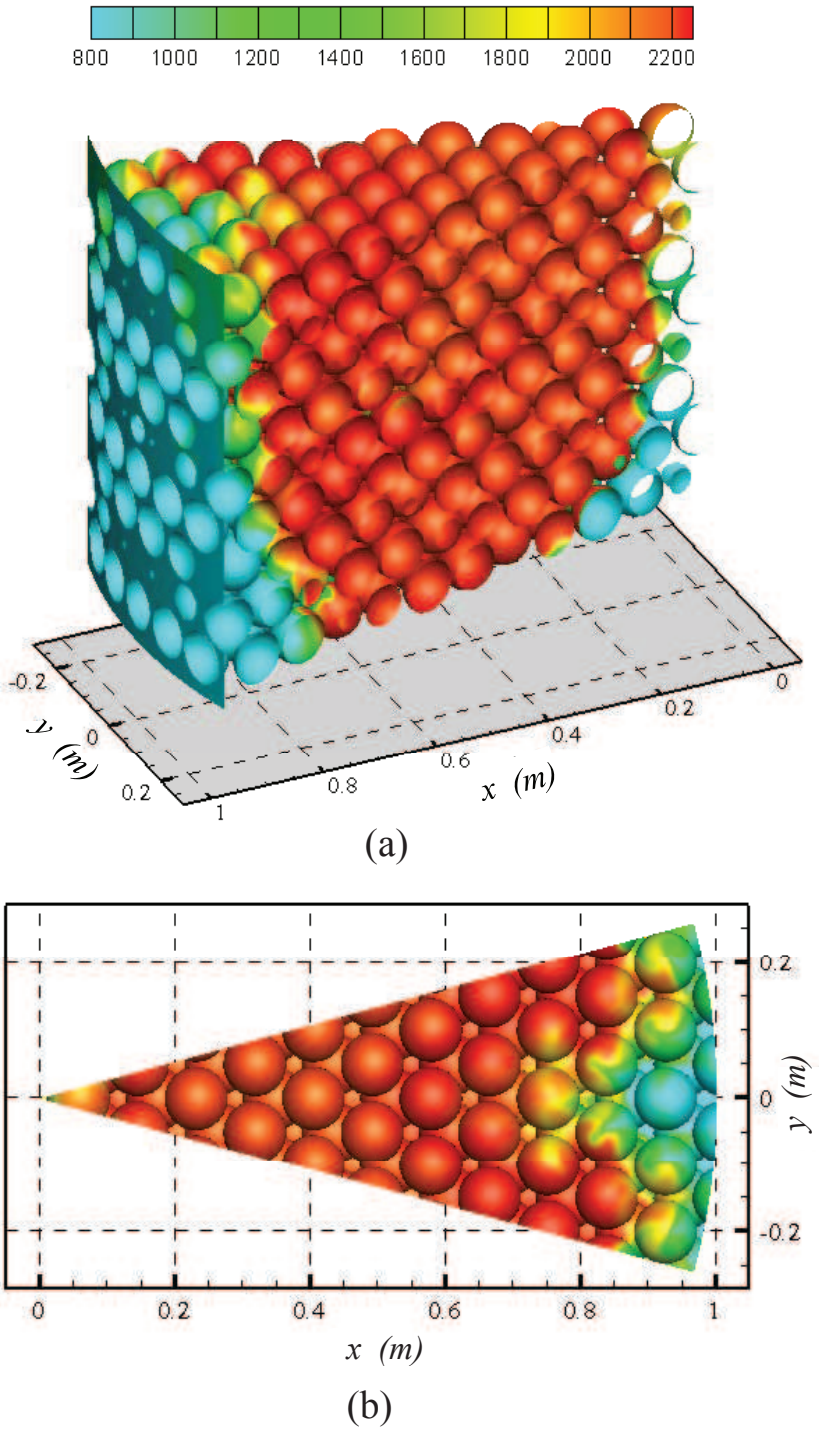

Figure 6.12: Temperature contours for Lance depth = 0.1 m and $v_{fm} = 57.2m/s$: (a) Overall view, and (b) top view; legend shows temperature in K

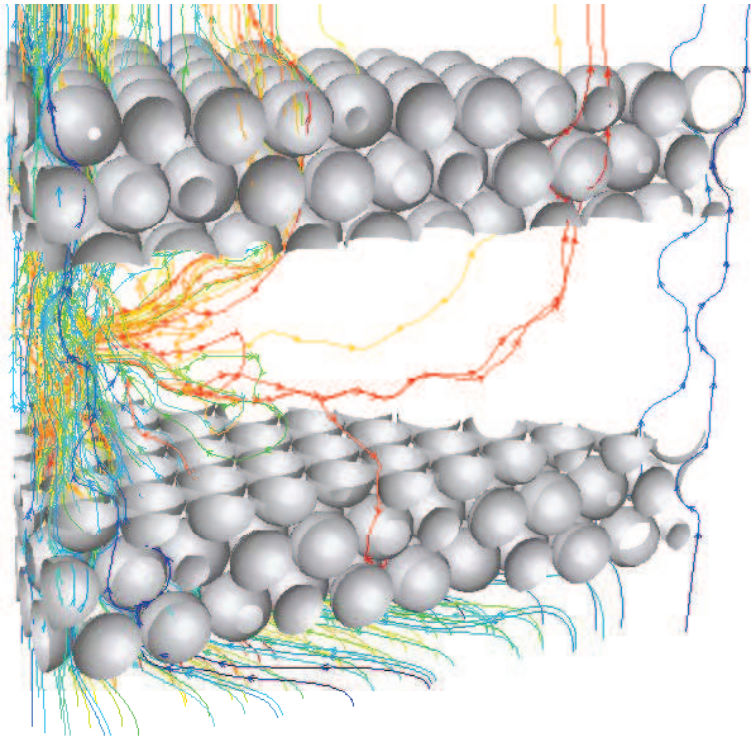

Figure 6.13: Pathlines released from the inlet of the cooling air for Lance depth = 0.1 m and $v_{fm} = 57.2m/s$

6.3.3 Influence of preheating combustion air

To increase the outlet velocity with constant volumetric flow rate, there are two approaches. One is by reducing the lance diameter, as described in the previous subsection, and the other is by preheating the combustion air.

For fuel-fired industrial heating processes, one of the most potent ways to improve efficiency and productivity is to preheat the combustion air prior its going to the burners. The source of this heat energy is the exhaust gas, which leaves the process at elevated temperature. A heat exchanger, normally a recuperator or regenerator, can extract a large portion of the thermal energy in the flue gases and transfer it to the incoming combustion air. Of course, the purpose of recycling heat this way is to reduce the amount of the purchased fuel needed by the furnace. In this work, however, we consider to use this heat to achieve a high exit velocity of the fuel jet. That is to say, the fuel demand or the volume flow rate of the fuel and combustion air is as the same as the non-preheated case, and therefore the jet velocity is increased with the preheating of the combustion air.

In this case, the geometric model is the same one applied for in Case I. The difference is that the combustion air is preheated to 600 K. As the volumetric ratio of the fuel to the combustion air is very small, the fuel mixture is assumed to be 600 K. Accordingly, the exit velocity of the fuel mixture is increased from 29.2 m/s to 43.8 m/s. Table 6.4 shows the inlet and outlet boundary conditions.

Table 6.4: Inlet and outlet boundary conditions for Case IV

		D_h (m)	I (%)	Velocity (m/s)	Temperature (K)
Inlet	fuel mixture	0.07	10	43.8	600
	Cooling air	1.02	10	0.415	800
Outlet		1.02	10	-	300

The temperature contours are illustrated in Fig. 6.14. As expected, it can be seen that the penetration of the combustion gas is relatively deeper in comparing to Case I but less than Case III. Apparently, the influence depends on the preheated temperature which determines the outlet velocity. However, the air preheating is cost effective or not must be evaluated on case-by-case basis. Generally speaking, the lime production process is not a good candidate as the exhaust gas is dirty and has relatively lower temperature. As far as this is concerned, the gas-fired shaft kiln has advantage compared with the more traditional methods using coal or woods as a mixed feed with the limestone. There is normally no soot and less ash in the flue gas.

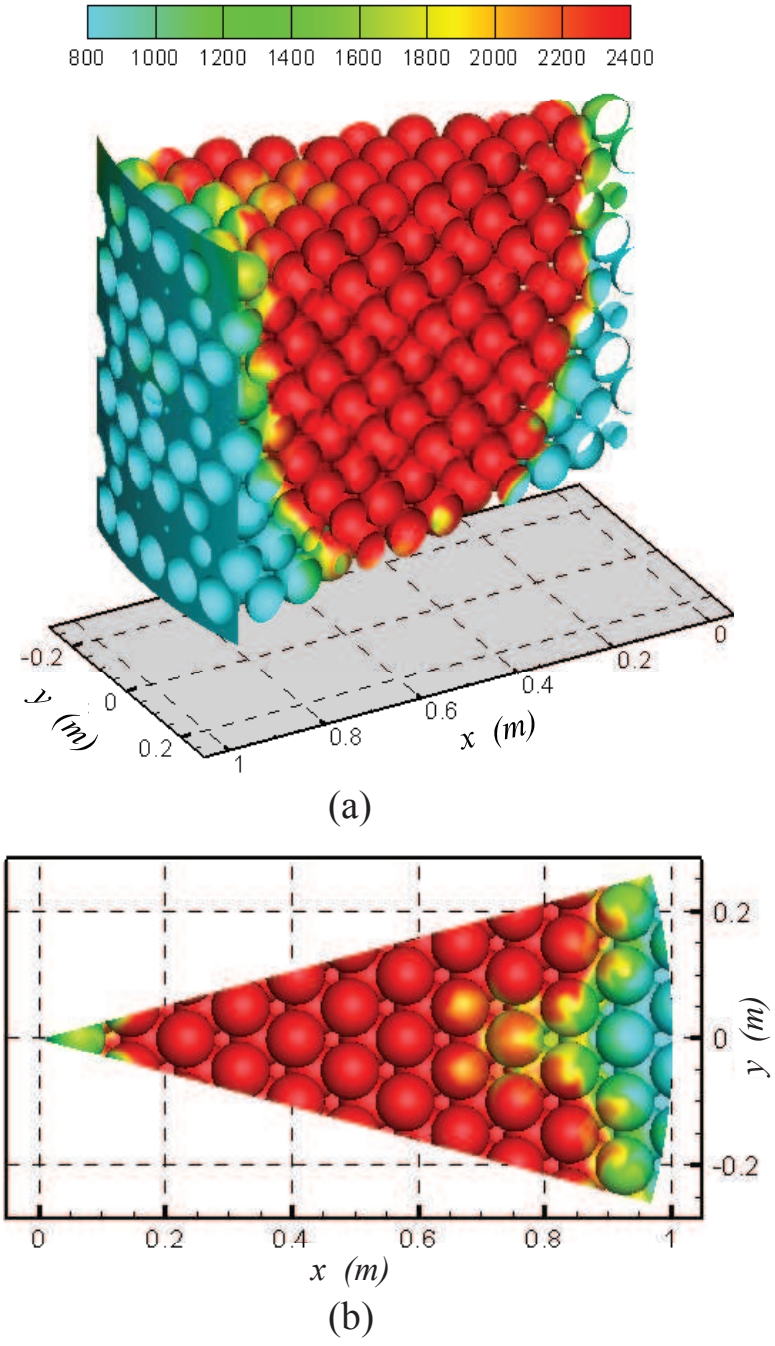

Figure 6.14: Temperature contours for Lance depth = 0.1 m and $v_{fm} = 43.8m/s$: (a) Overall view, and (b) top view; legend shows temperature in K

6.3.4 Influence of burner arrangements

To distribute the fuel and combustion air evenly throughout the kiln, many burners are normally required. These burners can be equipped in the kiln in a horizontal arrangement or a vertical arrangement, or a combination. Being arranged horizontally, the burner lances may protrude into the hot bed of material at different depths to enable an optimum fuel distribution over the whole cross section of a kiln. This arrangement is particularly practical when the kiln has a big diameter.

In this section, one simulation is conducted to show the flow patterns in kilns with a 2-level burner arrangement. The structure of the geometry is shown in Fig. 6.4. Six burner lances on the first level protrude 500 mm into the bed (r_1 = 500 mm), and the others are situated close to the wall (Lance depth = 2 mm; r_2 = 998mm). 40% of the fuel and combustion air is allocated to the burners on Level-1 whereas the remaining is introduced by the burners on Level-2. Those parameters are only for this situation, and this work makes no attempt to prove they are the optimum data.

The inlet and outlet boundary conditions in this case are listed in Table 6.5.

Table 6.5: Inlet and outlet boundary conditions for Case V

			D_h (m)	I (%)	Velocity (m/s)	Temperature (K)
Inlet	fuel mixture	Level-1	0.07	10	23.36	400
		Level-2	0.07	10	35.04	400
	Cooling air		1.02	10	0.415	800
Outlet			1.02	10	-	300

The calculation is less stable comparing with previous cases. Great fluctuation of residuals like the turbulence kinetic energy (κ) and turbulent dissipation rate (ϵ) is obvious in the residual history window. The problem can be solved by reducing the mesh size near the inlets of the burners, but which will lead to an increase in the number of grid cells.

The temperature distribution over the cross section of the kiln is shown in Fig. 6.15. As the combustion gas reaches the center line of the kiln, it is easy to understand that the cooling air flows through in between the burners of Level-2. Even though the cooling region can not be completely removed with this arrangement, the temperature distribution is better than Case I. The results are quantitatively compared in Fig. 6.16.

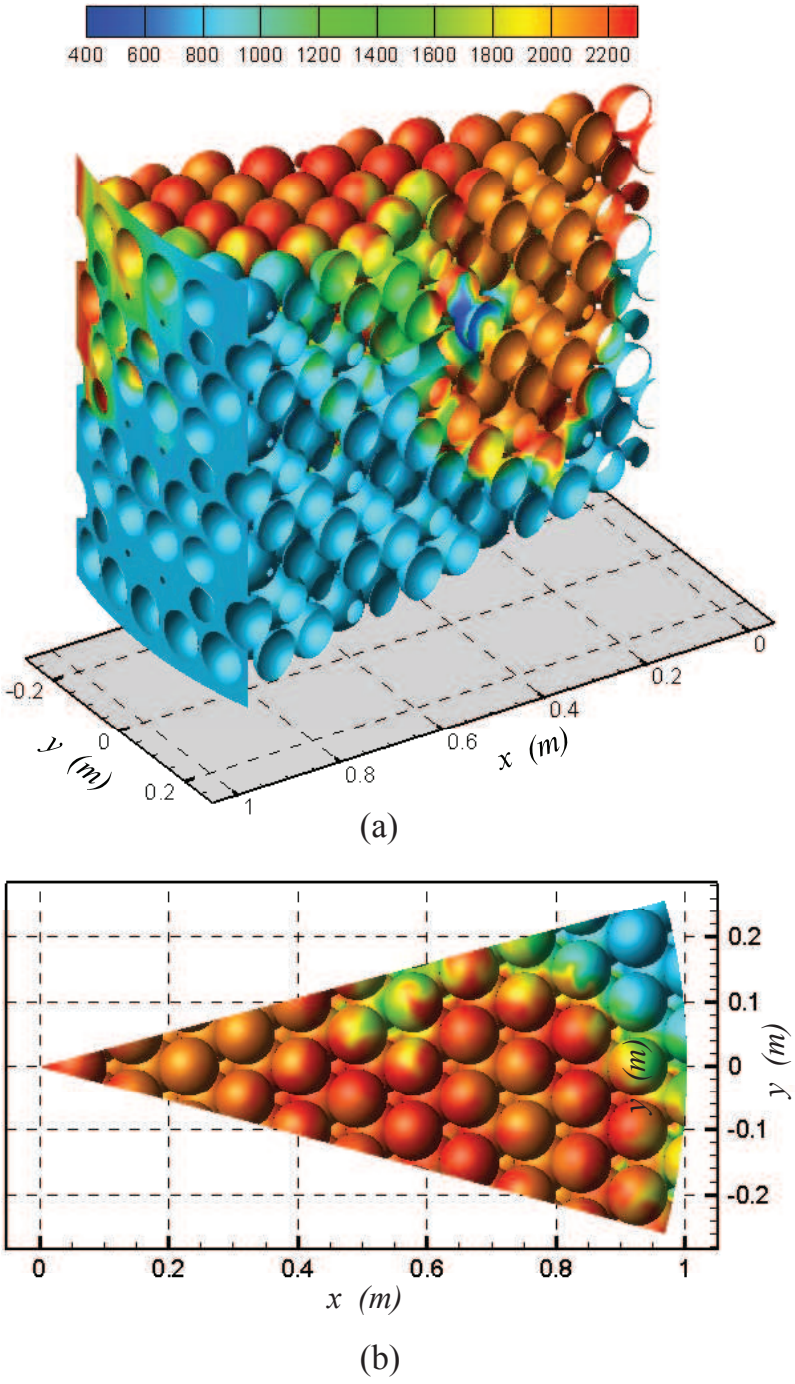

Figure 6.15: Temperature contours on the surface of particles for two-level burners ($v_{fm1} = 23.36m/s$, $v_{fm1} = 23.36m/s$): (a) Side view, and (b) top view; legend shows temperature in K

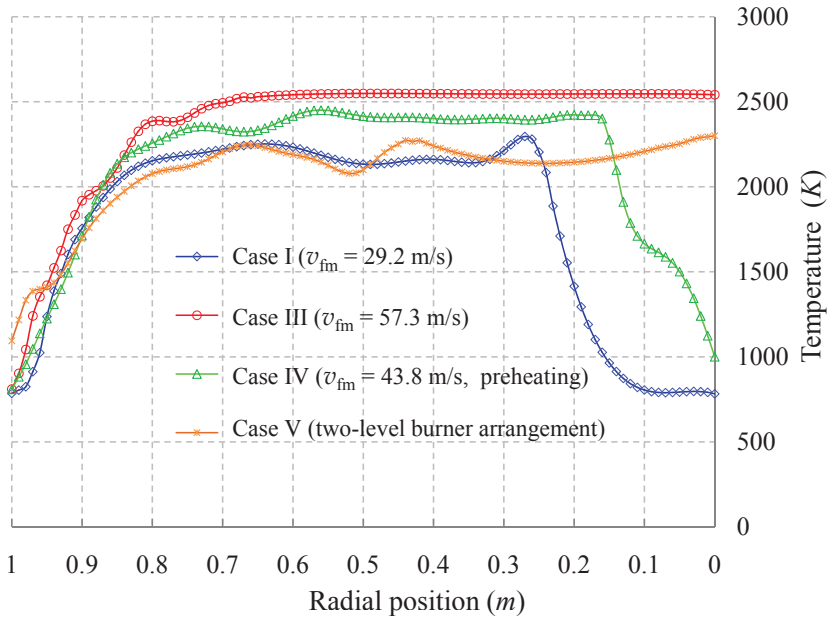

Figure 6.16: Comparison of the mean temperature on the plane of $z = 0.9m$ in x-direction (Lance depth = 0.1 m for each case)

So far, we′ve carried out five simulations to investigate some factors of interest in designing. It turns out that all factors have impact on the radial temperature distribution except the lance depth. As one can see from Fig. 6.16, the radial temperature distribution can be improved by reducing the lance diameter, preheating the combustion air, and a two-level arranged burner system. Even though the rate that the jet entrains and mixes with the surrounding air in a packed bed is not as high as in an open environment, jet-induced mixing still can be a critical factor when designing burner systems. As mentioned, it is only a matter of economic balance between the extra cost required by high pressure transport and introduction of more burner lances. While for kilns with big diameter, a two-level burner arrangement with each level at different lance depths is quite necessary to achieve optimal operation. However, the optimum lance depth for each level or the optimum distance between levels and so on is beyond this work.

6.4 Modeling the kilns with diffusion burner

All simulations carried out in the previous section are based on premixed firing system. Generally, however, diffusion burner is more widely applied in the lime production. Compared with premixed burner, diffusion burner has many advantages. Technically, a diffusion burner has longer flame and the flame temperature is lower, which can prevent local overheating near the burner. The diffusion flame is more stable and consequently more suitable for high outlet velocity cases. What′s more, the diffusion burner is suited for a wide variety of fuels, which can be gaseous and liquid, as well as solid. Thus, one simulation based on diffusion burner is performed in this section to demonstrate the non-premixed model.

6.4.1 Geometry and mesh of the diffusion burner

The diffusion burner going to be modeled has a very simple configuration. As depicted in Fig. 6.17, it is a tube-in-tube structure. The inner tube is for introducing the natural gas, while the outer is used to convey the primary combustion air. As there is no original system to refer to, the dimensions of the burner may or may not follow any existing burner.

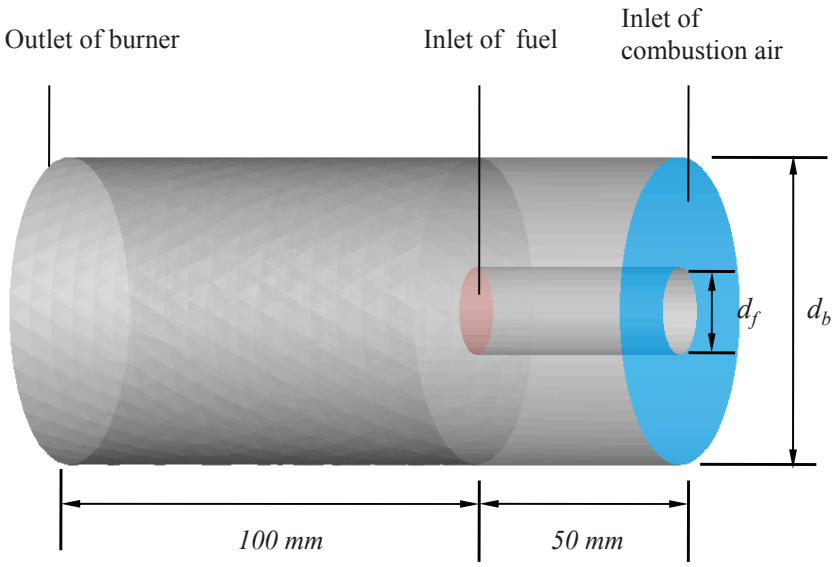

Figure 6.17: The geometry and the dimensions of the diffusion burner

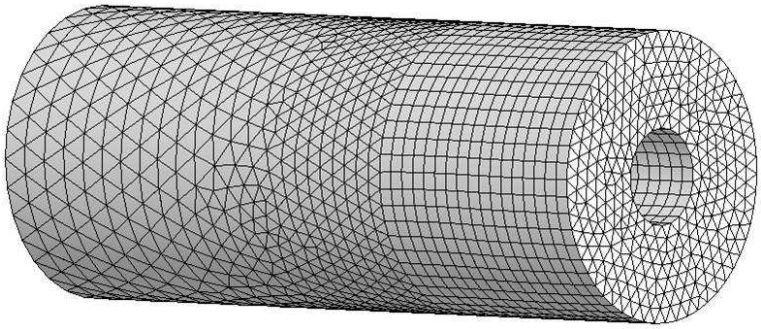

Figure 6.18: The hybrid mesh of the diffusion burner

The geometry is divided into two volume for meshing. For the dual tube part, triangle grids are firstly mapped on the source face (face defined as the inlet of cooling air) with interval size of 3 mm, and then the *Cooper* meshing is applied to project the source-face mesh node patterns through the volume with the same interval size. Subsequently, triangle grids with interval size of 2 mm are mapped on the fuel inlet. Considering that the grid size of the packing domain is 6 mm, a *meshed size function* is defined with the fuel inlet face as the source and 1.04 as the growth rate. When the single tube volume is meshed, the size function attached creates a graded mesh. Fig. 6.18 shows the computational mesh which consists of two types of grid, tetrahedron and triangle prism.

6.4.2 Definition of the models and solution controls

To simulate a system with diffusion burner, FLUENT provides two models to model combustion. One is *species transport* with volumetric reaction, the other is *non-premixed combustion*. When species transport is used, the properties of the mixture material should be defined. However, the number of volumetric species is limited to 3, and the mixture of nature gas L and air is not available in FLUENT database. Furthermore, the non-premixed modeling approach offers many benefits over the eddy-dissipation formulation [5], and allows intermediate (radical) species prediction, dissociation effects etc. Therefore, non-premixed combustion model is chosen. The PDF (the Probability Density Function) table is the same one created in modeling the partial premixed cases.

The other settings, such as the turbulence model and the under-relaxation factors, as well as the discretization method, are no different from previous simulations.

6.4.3 Boundary conditions

The diameters of the inner and outer tube are $d_f = 20mm$ and $d_b = 60mm$, respectively. The amounts of the combustion air and the natural gas are in keeping with the previous simulations in this chapter. Accordingly, the velocities at the inlet of the fuel and combustion air are calculated and listed in the Table 6.6 All

Table 6.6: Inlet and outlet boundary conditions

		D_h (m)	I $(\%)$	Velocity (m/s)	Temperature (K)
Inlet	fuel	0.02	10	47.3	400
	Combustion air	0.04	10	38.7	400
	Cooling air	1.02	10	0.415	800
Outlet		1.02	10	-	300

walls are specified as stationary.

6.4.4 Simulation and results

Comparing to the simulations with premixed model, modeling of non-premixed combustion takes much shorter computational time. Converged solution is obtained within 1000 iterations. This is because under certain assumptions the thermochemistry is reduced to a single parameter: the mixture fraction. In other words, combustion is simplified to a mixing problem, and the difficulties associated with closing non-linear mean reaction rates are avoided. Once mixed, the chemistry can be modeled as being in chemical equilibrium with the Equilibrium Model, being near chemical equilibrium with the Steady Laminar Flamelet Model.

Likewise, the results are illustrated by plotting the temperature profiles. Fig. 6.19 and Fig. 6.20 show the side view and the top view of the temperature contours on the particles′ surface. In contrast to the premixed cases, it is plain to see that

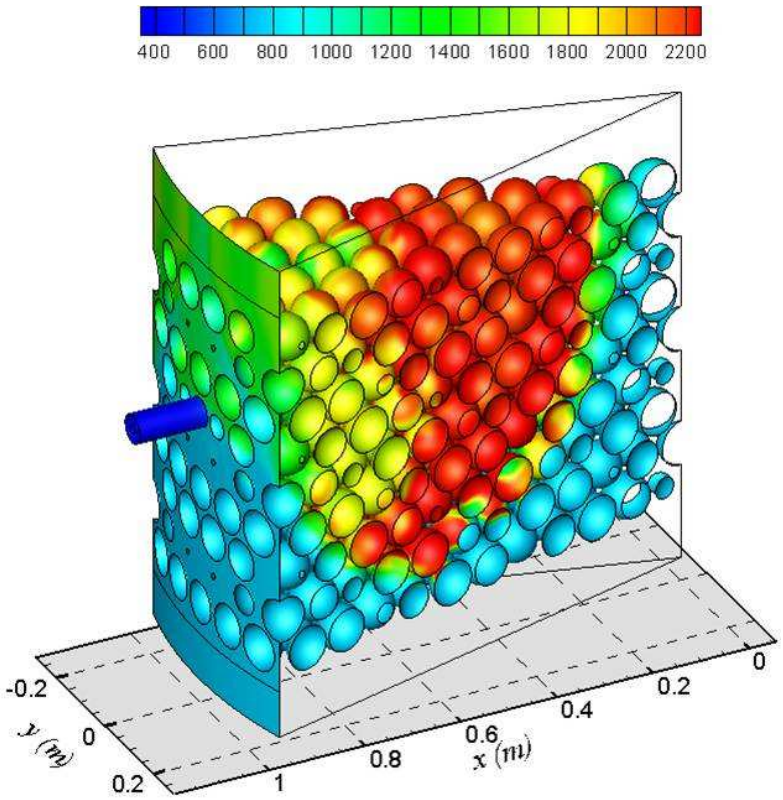

Figure 6.19: Temperature contours in the case with diffusion burner; Legend shows temperature in K

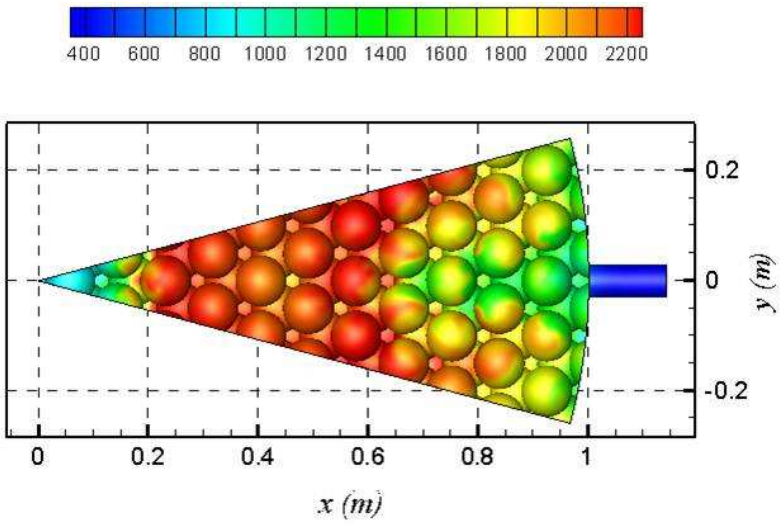

Figure 6.20: Temperature contours in the case with diffusion burner (top view); Legend shows temperature in K

the non-premixed combustion has a longer flame length and the penetration of the combustion gas is deeper (in this case the lance depth is 2 mm). It also

can be observed that the uniformity of the radial temperature distribution is much better. We can well imagine a good mixing between the cooling air and combustion gas. Fig. 6.21 and Fig. 6.22 depict the pathlines released from the inlet of the combustion air and the cooling air, respectively. Apparently, most of the cooling air is mixed up with the jet flow due to the recirculation generated by the combustion air. And due to these advantages, non-premixed (diffusion) burners are wildly used in furnaces.

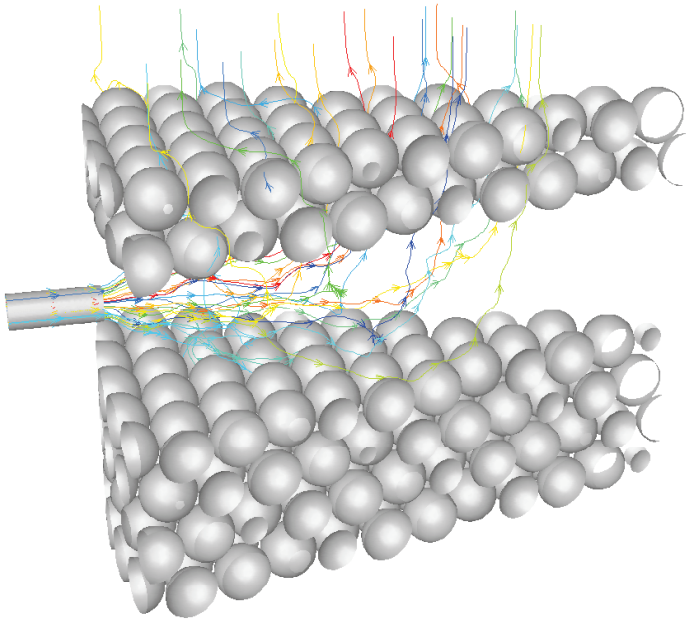

Figure 6.21: Pathlines released from the inlet of combustion air

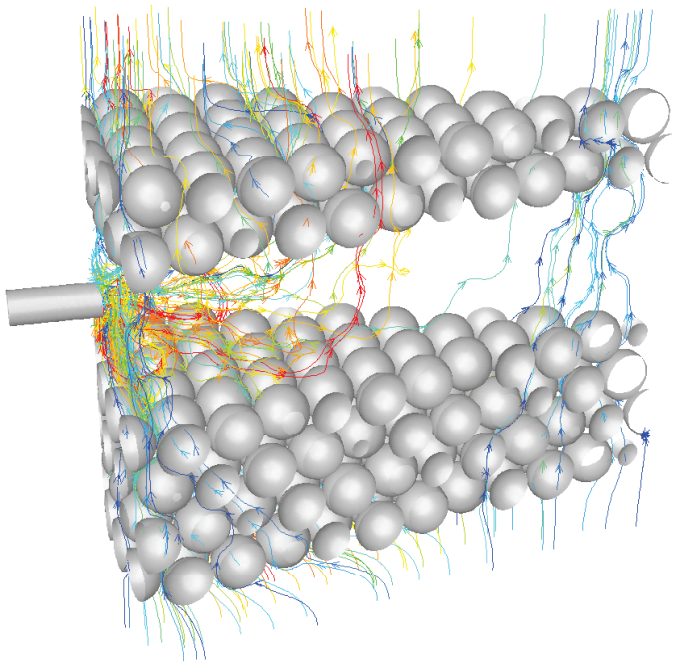

Figure 6.22: Pathlines released from the inlet of cooling air

6.5 Porous medium model

The porous media model is used widely for many problems, including flows through packed beds, filter papers, perforated plates, and tube banks. As mentioned in Chapter 2, however, the model itself is nothing more than an added momentum sink in the governing momentum equations and hence has great limitations in application. Besides, there are some restrictions placed upon the geometry of the porous media [63]:

(P1) The void space of the porous media is interconnected.

(P2) The dimensions of the void space must be large compared to the mean free path length of the fluid molecules.

(P3) The dimensions of the void space must be small enough so that the fluid flow is controlled by adhesive forces at fluid-solid interfaces and cohesive forces at fluid-fluid interfaces (multiphase systems).

The first assumption (P1) is obvious since no flow can take place in a disconnected void space. The second property (P2) will enable us to replace the fluid molecules in the void space by a hypothetical continuum. While property (P3) excludes many cases from the definition of a porous medium. For example, beach sand, sandstone, rye bread, wood, and the human lung are defined as natural porous media. 0.5-cm-diameter Liapor spheres and 1-cm-size crushed limestones can be regarded as granular porous materials [64]. However, the dimensions of the void space in the packed bed with 10-cm-diameter limestones might be oversized.

As the last part of this work, porous media model is used and compared with discrete particle model to show whether it is suitable for modeling lime shaft kiln.

6.5.1 Defining the viscous and inertial resistance

As we know, porous media are modeled by the addition of a momentum source term to the standard fluid flow equations. The source term is composed of two parts: a viscous loss term (Darcy, the first term on the right-hand side of Eq. 6.2), and an inertial loss term (the second term on the right-hand side of Eq. 6.2) [5]

$$S_i = -\left(\sum_{j=1}^{3} D_{ij}\mu v_j + \sum_{j=1}^{3} C_{ij}\frac{1}{2}\rho\,|v|\,v_j\right) \tag{6.2}$$

where S_i is the source term for the ith (x, y, or z) momentum equation, $|v|$ is the magnitude of the velocity and D and C are prescribed matrices. This momentum sink contributes to the pressure gradient in the porous cell, creating a pressure drop that is proportional to the fluid velocity (or velocity squared) in the cell.In the case of simple homogeneous porous media (isotropic media), it can be written as

$$S_i = -\left(\frac{\mu}{\alpha}v_i + C_2\frac{1}{2}\rho\,|v|\,v_i\right) \tag{6.3}$$

or written as the pressure drop per unit length

$$\frac{\Delta P}{L} = -\left(\frac{\mu}{\alpha} v_i + C_2 \frac{1}{2} \rho \left|v\right| v_i\right) \tag{6.4}$$

where α is the permeability and C_2 is the inertial resistance factor.

To model a porous region without considering heat transfer, the main additional inputs for the problem setup are defining the porous zone and specifying the porosity of the porous medium, and setting the viscous resistance coefficient $1/\alpha$ and the inertial resistance coefficient C_2. As the porosity is known, to find the resistance coefficients is hence the first task. Methods for determining the permeability and the inertial resistance factor are presented below.

Based on superficial velocity, using a known pressure loss

The porous media model assumes that the porous cells in FLUENT are 100% open, and the values specified for $1/\alpha_{ij}$ and $C_{2_{ij}}$ must be based on this assumption. However, if how the pressure varies with the velocity through the actual device, which is only partially open to flow, is known, a value for C_2 can be computed by the following relations for the FLUENT model [5]

$$K'_L = K_L \frac{v_{open}^2}{U^2} \tag{6.5}$$

where K'_L is the adjusted loss factor, K_L is the loss factor which is known from experiment, v_{open} is the velocity through the real open area, and U is the superficial velocity or the velocity through 100% open area.

And then, the inertial loss factor can be calculated by converting the adjusted loss factor into a loss coefficient per unit thickness of the device

$$C_2 = \frac{K'_L}{thickness} \tag{6.6}$$

Note that, for anisotropic media, this value must be computed for each of the 2 (or 3) coordinate directions.

The permeability α is independent of the nature of the fluid while is determined by the geometry of the medium, and hence can be calculated in terms of the geometry parameters. In the case of beds of particles, the hydraulic radius theory of Carman-Kozeny leads to the relationship [64]

$$\alpha = \frac{D_p^2 \varphi^3}{180 \left(1 - \varphi\right)^2} \tag{6.7}$$

where D_p is the effective average particle diameter and can be obtained from

$$D_p = \int_0^\infty D_p^3 h\left(D_p\right) dD_p \Big/ \int_0^\infty D_p^2 h\left(D_p\right) dD_p \tag{6.8}$$

where $h(D_p)$ is the density function for the distribution of diameters D_p.

Using the Ergun equation for a packed bed

Considering the modeling of a packed bed, the appropriate constants can be derived by using the Ergun equation, a semi-empirical correlation applicable for many types of packing:

$$\frac{\Delta P}{L} = 150 \cdot \frac{(1-\varphi)^2}{\varphi^3} \cdot \frac{\mu \cdot U}{\overline{d_p}^2} + 1.75 \cdot \frac{1-\varphi}{\varphi^3} \cdot \frac{\rho \cdot U^2}{\overline{d_p}} \tag{6.9}$$

where d_p is the mean diameter.

Comparing Eq. 6.3 with 6.9, the permeability and inertial loss coefficient in each component direction can be identified as

$$\alpha = \frac{d_p^2 \varphi^3}{150\,(1-\varphi)^2} \tag{6.10}$$

and

$$C_2 = \frac{3.5\,(1-\varphi)}{d_p \varphi^3} \tag{6.11}$$

As can be observed in Eq. 6.10 and 6.11, both coefficients are determined by the geometry parameters.

Of course, the porous coefficients can be also derived based on experimental pressure and velocity data. As we don′t have experimental data so far, Ergun equation is used in the present work.

6.5.2 Model definition and Boundary conditions

The standard κ-ϵ model with standard wall function is applied to model the turbulence and, partial premixed model is used to calculate combustion. Given that the grid is relatively coarse, the first order upwind schemes are selected to compute the field variables. The relaxation factors are set to the FLUENT default values.

$CaCO_3$ is used as the medium and its properties are defined in FLUENT database. The resistance coefficients are computed based on three different porosities for particle diameter of 100 mm, as shown in Table 6.7.

Table 6.7: Values for the viscous and inertial resistance coefficients

Porosity	Viscous resistance (m^{-2})	Inertial resistance (m^{-1})
0.4	84375	328
0.6	11111.1	64.8
0.8	1171.9	13.7

The fuel is still natural gas L and the fuel demand, air demand, and the mass flow ratio of cooling air to lime are as the same as that used for the calculations based on discrete particle model in the previous section. Gas inlets are set as velocity inlet and gas outlet is defined as pressure outlet. Table 6.8 shows the boundary settings.

Table 6.8: Inlet and outlet boundary conditions

		D_h (m)	I $(\%)$	Velocity (m/s)	Temperature (K)
Inlet	fuel mixture	0.07	10	29.2	400
	Cooling air	2.0	10	0.415	800
Outlet		2.0	10	-	300

6.5.3 Geometry and computational mesh

The segment model strategy is deployed again in order to reduce the computational effort. The 30^o segment geometry consists of a cooling air inlet, a inlet for fuel mixture indicated by the burner, a gas outlet, and two periodic faces.

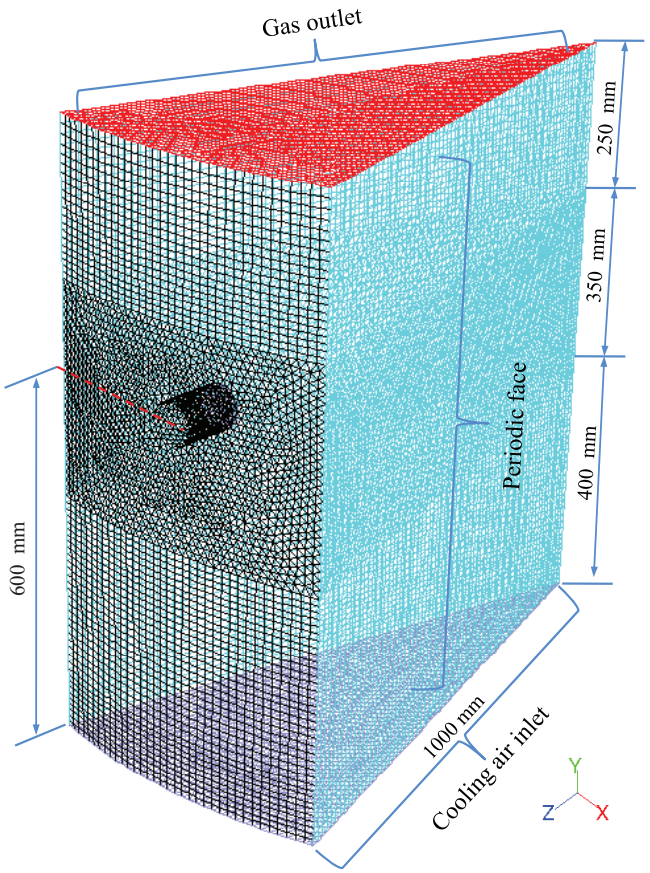

Figure 6.23: Geometry and computational mesh for the simulation

As depicted in Fig. 6.23, both the height and diameter of the geometry are 1.0 m, the same as the dimensions of the geometry used for previous simulations. The burner lance has a diameter of 0.07 m and is located 0.6 m high from the cooling air inlet with the lance depth of 0.1 m. The computational mesh is divided into 3 parts. Two parts are composed of prism cells and the one close to the burner consists of pyramids due to the irregular shape. Mesh independence of the simulation results are obtained by variation of the number of mesh elements. The mesh has 503,151 cells in all.

6.5.4 Simulation results

Simulations are performed for porosity of 0.4, 0.6, and 0.8, respectively. As always, convergence of the solution is assumed at a residual value of 10^{-6} for energy and a value of 10^{-3} for the rest variables. Solution initialization is computed from all zones. Solution is converged over around 500 iterations and, computational time for each run is about 3 hours which is much less in comparing to discrete particle modeling.

The temperature contours in the gas outlet and the y-plane ($y = 0$) for each case are displayed in Fig. 6.24, and compared with the result obtained based on discrete particle geometry.

As expected, the penetration of the combustion gas is under-predicted significantly by application of the porous media model. To achieve a deeper penetration, porosity must be bigger. It is worthwhile to note that the penetration changes slightly with the porosity increasing from 0.4 to 0.6, even though the values of the resistance coefficients decrease dramatically. As calculated in Table 6.7, viscous resistance decreases from 84375.0 m^{-2} to 11111.1 m^{-2} while inertial resistance drops to 64.8 m^{-1} from 328 m^{-1}. Till the porosity increases to 0.8, the penetration predicted in the porous body is nearly the same as that calculated upon the geometry with the presence of particles and from a microscopic perspective, the flow patterns closely resemble (see Fig. 6.25). In such a case, however, the resistance is already very small. This results indicate that porous media model is more suitable for the cases in which the flow is dominated by adhesive forces, i.e. the void space in the media should be small enough, or flow at low Reynold number so that inertial terms in the Navier-Stokes equation are relatively unimportant, like creeping flow. For high velocity flow, high jet flow in particular, the momentum loss is obviously over-predicted with porous media model. Fig. 6.26 presents the x-velocity contours in the plane at the burner level ($z = 0.6$ m for porous media modeling and $z = 0.49$ m for discrete particle modeling). The negative velocity means nothing but the flow is in $-x$ direction. Velocity is low than 1 m/s is cut off from the contours for the sake of convenient comparison. As it can be seen that, the radial velocity is decelerated sharply for porosity of 0.4 and 0.6 by porous media model.

Based on this analysis, a conclusion could be drawn that shaft kilns processing around 100-mm-diameter limestone might not be treated as porous body. However, there is also positive information, e.g., a good agreement with the results predicted by discrete particle model when the porosity is increased to 0.8. If the validity

could be proved in a certain range of particle sizes, it might be helpful in the design.

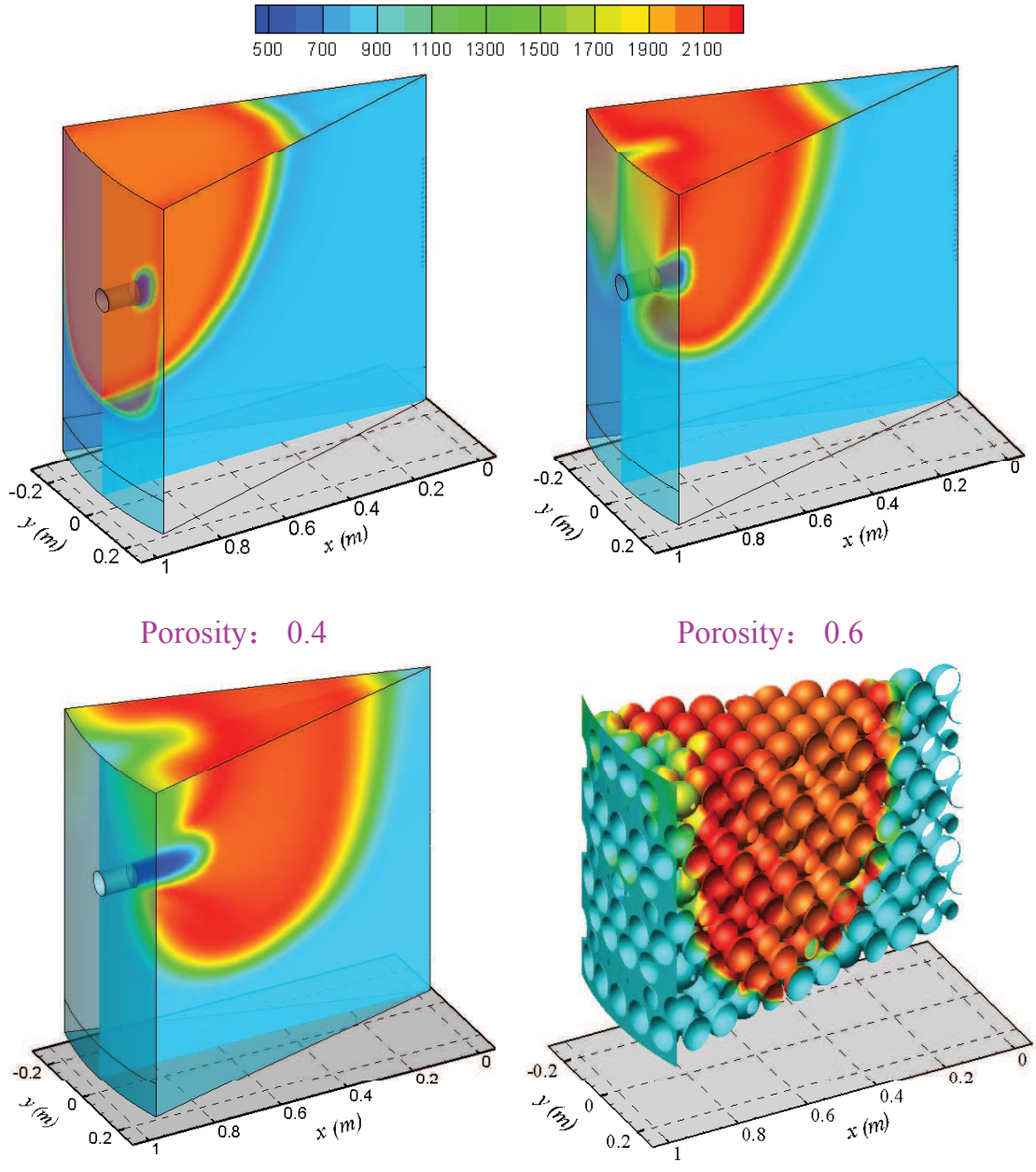

Figure 6.24: Comparison of the temperature contours by using porous media model and discrete particle model; Legend shows temperature in K

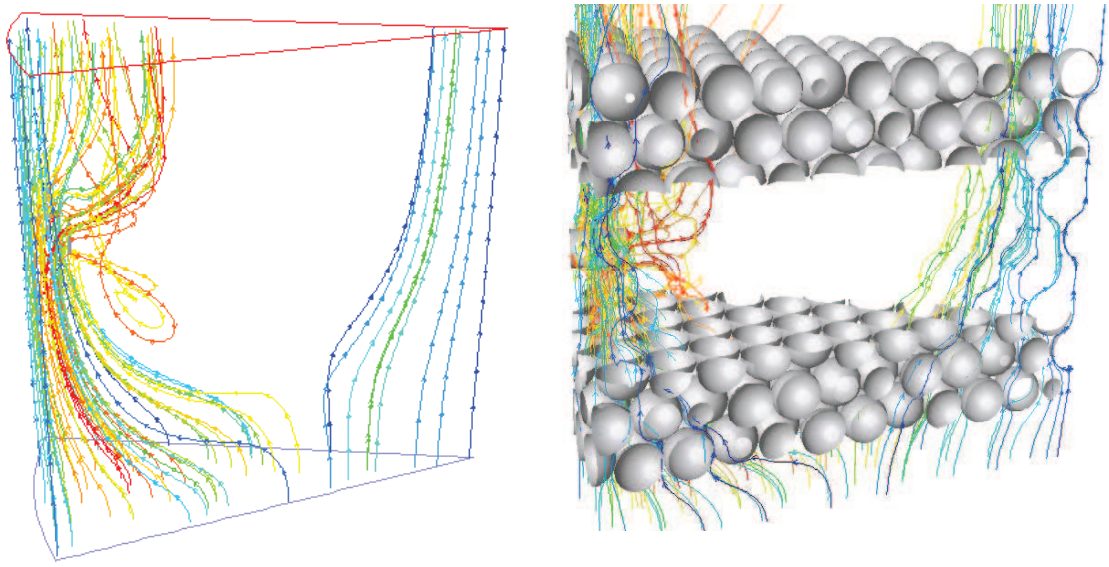

Porosity： 0.8
（Porous media model）

Porosity： 0.4
(Discrete particle model)

Figure 6.25: Comparison of the pathlines released from the cooling air inlet for porosity of 0.8 by porous media model and 0.4 by discrete particle model

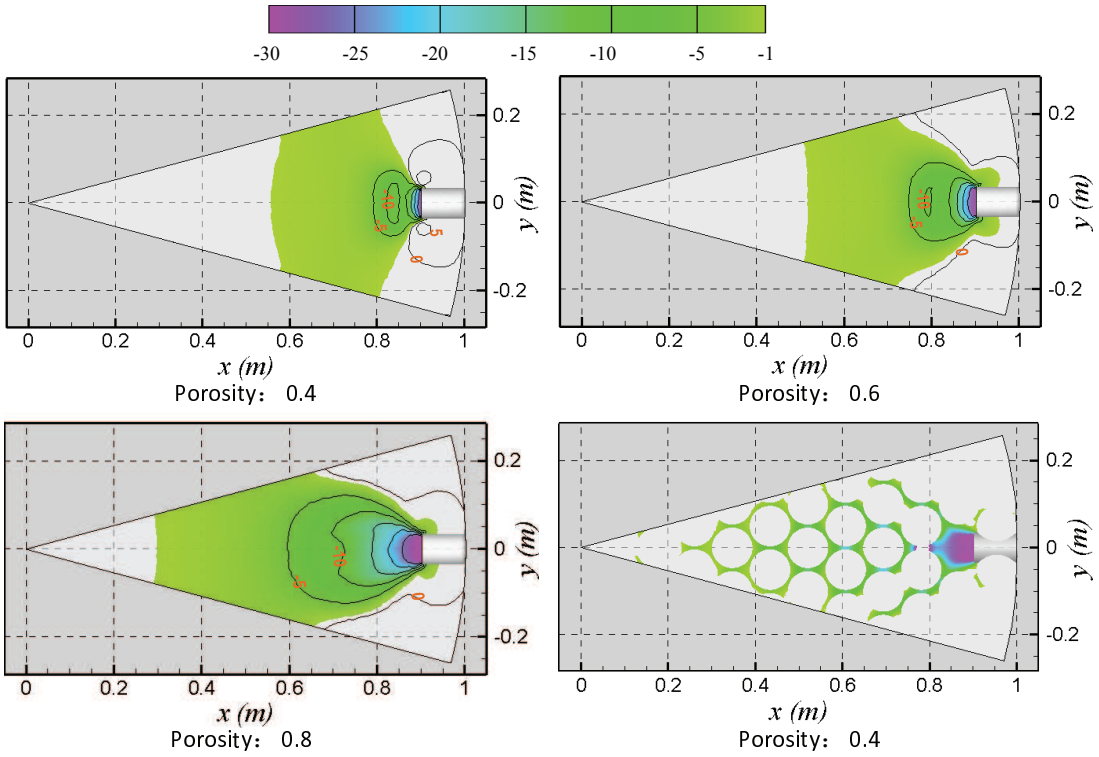

Figure 6.26: Comparison of the x-velocity contours by using porous media model and discrete particle model; Legend shows velocity in m/s

6.6 Summary and Conclusions

This chapter attempts to demonstrate the viability of 3-D geometric model by means of performing CFD simulation. The flow pattern occurring in lime shaft kilns is visualized and studied in detail. The main factors considered in this project are lance depth, burner diameter, preheating of combustion air, burner arrangement and so forth. The results show that the increase of the lance depth may be helpful to protect the refractory wall being overheated but has slight effect on the overall radial temperature distribution, which is in agreement with 2-D simulations. Mixing between the combustion gas and the cooling air can be improved by reduce the burner diameter or by preheating the combustion air, both of which accelerate the jet speed and provide energy aspirating the cooling air. Simulation is also carried out on the case with diffusion burner. It appears that the flame length is much longer and deeper penetration is achieved. That′s why diffusion burner is always preferred in shaft kilns. Additionally, the application of porous media model in lime shaft kiln is tested. The results illustrate that the radial penetration depth of the combusting jet flow is much less for the same porosity. It is most due to the over-prediction of the momentum loss caused by the inertial terms. More effort is worth to be spent in the future work.

6.7 Recommendations

Till this chapter, 2-D and 3-D simulations have been carried out, the in-kiln flow structures are visualized by distinctive images. To be applied to industry, however, there is still a long way to go. The geometry needs to be further developed and evaluated, and some uncertainties also need to be resolved. First of all, experimental work should be conducted to validate the CFD modeling. Second, in its present state the model deals only with spheres of the same size. In the future work, the model might be extended to different particle size. Third, more efforts are worth to be spent on *porous media model*. Foremost, the model has great advantage in building the geometry and mesh. The simple geometric model and relatively small computational mesh size are more practical once heat transfer and reactions, for instance the decomposition of limestone, are involved. An immediate extension of the research presented about the porous media model could be performing simulations based on physical velocity. The last, more information on the shaft kiln operation is required for the further development of the CFD model.

Bibliography

[1] Graymont Ltd. What is lime: Lime cycle. URL http://www.graymont.com, 2006.

[2] C.E. Baukal. *Industrial burners handbook*. CRC Press, 2003.

[3] C.E. Baukal. *Heat Transfer in Industrial Combustion*. CRC Press,Boca Raton, 2000.

[4] RHI AG. The maerz parallel flow regenerative lime kiln. URL http://www.rhi-ag.com, 2005.

[5] ANSYS. *FLUENT Documentation*. Fluent Inc, 2006.

[6] M.E. Taskin, A.G. Dixon, and E.H. Stitt. CFD simulation of flow in fixed beds of cylindrical particles. *International Journal of Chemical Reactor Engineering*, 5:A21, 2007.

[7] J.P. Hartnett and T.F. Irvine. *Advances in Heat Transfer*. Academic Press, Inc, New York, v. 18 edition, 1987.

[8] J.A.H. Oates. *Lime and Limestone: Chemistry and Technology, Production and Uses*. Wiley-VCH, 1 edition, 1998.

[9] A. Bes. *Dynamic Process Simulation of Limestone Calcination in Normal Shaft Kilns*. PhD thesis, Otto-von-Guericke-Universitaet, Magdeburg, Germany, 2006.

[10] Wikipedia. Lime kiln. URL http://www.en.wikipedia.org/wiki/Limekiln, 2007.

[11] B. Jenkins. *What Are Shaft Kilns for Lime Manufacture*. IFRF, 1 edition, 2003.

[12] D. Daniele. Fercalx & beckenbach technologies for soft and hard burnt lime. In *ILA conference in Prague*, pages 1–15, Prague, 2006.

[13] V.Y. Baukal, C.E.and Gershtein and X. Li. *Computational fluid dynamics in industrial combustion*. CRC Press, Boca Raton, 2000.

[14] A.F. Reshetnyak, V.A. Konev, A.N. Mamaev, and N.I. Seryakov. Improvement of shaft furnace construction for roasting limestone. *Refractories and Industrial Ceramics*, 49(3).

[15] B.A. Unaspekov and L.V. Strekalova. A model study of the performance of a kazogneupor shaft kiln. *Refractories and Industrial Ceramics*, 43:275–276, 2002.

[16] Z. Yi and H. Chen. Numerical simulation of thermal process and energy saving of lime furnace. *Journal of Central South University of Technology*, 12:295–299, 2005.

[17] C.L. Verma. Simulation of lime shaft kilns using mathematical modeling. *Zement-Kalk-Gips*, 12:576–582, 1990.

[18] C. Cheng. *Thermal Process Simulation of Reactive Particles on Moving Grates*. PhD thesis, Otto-von-Guericke-Universitaet, Magdeburg, Germany, 2007.

[19] A.F. Utenkov and L.V. Strekalova. Model of operation of a firing system for shaft kilns for firing of refractory raw material. *Refractories and Industrial Ceramics*, 27:114–118, 1986.

[20] Y.M. Gordon, M.E. Blank, V.V Madison, and P.R. Abovian. New technology and shaft furnace for high quality metallurgical lime production. In *Proceedings of Asia Steel International Conference*, pages 1–6, Jamshedpur, India, 2003.

[21] D.C. Wilcox. *Turbulence Modeling for CFD*. DCW Industries, Inc., La Canada, California, 1998.

[22] V.R. Kuznetsov and V.A Sabelnikov. *Turbulence and Combustion*. McGraw-Hill, New York, 1990.

[23] S.A. Unhale. *Application and Analysis of RANS Based Turbulence Models for Bluff Body Aerodynamics*. PhD thesis, Texas Tech Univerisy, Lubbock, USA, 2004.

[24] M. Nijemeisland. *Computational Fluid Dynamics in Fixed Bed Heat Transfer*. PhD thesis, Worcester Polytechnic Institute, Worcester, England, 2000.

[25] H.P.A. Calis, J. Nijenhuis, B.C. Paikert, and F.M. Dautzenberg. CFD modelling and experimental validation of pressure drop and flow profile in a novel structured catalytic reactor packing. *Chemical Engineering Science*, 56:1713–1720, 2001.

[26] B.E. Launder and D.B. Spalding. *Lectures in Mathematical Models of Turbulence*. Academic Press, London, 1972.

[27] E.S. Oran and J.P. Boris. *Numerical Simulation of Reactive Flow*. Cambridge University Press, 2 edition, 2001.

[28] G.D. Smith. *Numerical Solution of Partial Differential Equations: Finite Difference Methods*. Oxford University Press, Oxford, 3 edition, 1985.

[29] J.N. Reddy. *An Introduction to the Finite Element Method*. McGraw-Hill, New York, 1984.

[30] S.V. Patankar. *Numerical Heat Transfer and Fluid Flow.* Hemispher (McGraw-Hill), New York, 1980.

[31] H. Nillson. *A Numerical Investigation of the Turbulent Flow in a Kaplan Water Turbine Runner.* PhD thesis, Chalmers University of Technology, Gothenburg, Sweden, 1999.

[32] M. Nijemeisland and A.G. Dixon. CFD study of fluid flow and wall heat transfer in a fixed bed of spheres. *AIChE Journal*, 50:906–921, 2004.

[33] M.G. Rasul and D. Saotayannan. Modeling and simulation of thermodynamic processes of vertical shaft kiln used for producing deadburned magnesia. *International Journal of Energy and Enrironment*, 1:37–44, 2007.

[34] M. Nijemeisland and A.G. Dixon. Comparison of CFD simulations to experiment for convective heat transfer in a gas-solid fixed bed. *Chemical Engineering Journal*, 82:231–246, 2001.

[35] B. Lloyd and R. Boehm. Flow and heat transfer around a linear array of spheres. *Heat Transfer*, 26:237–246, 1994.

[36] A.G. Dixon and M. Nijemeisland. CFD as a design tool for fixed-bed reactors. *Industrial and Engineering Chemisty Research*, 40:5246–5254, 2001.

[37] M. Nijemeisland, A.G. Dixon, and E.H. Stitt. Catalyst design by CFD for heat transfer and reaction in steam reforming. *Chemical Engineering Science*, 59:5185–5191, 2004.

[38] A. Guardo and M. Coussirat. CFD flow and heat transfer in nonregular packings for fixed bed equipment design. *Ind. Eng. Chem. Res.*, 43:7049–7056, 2004.

[39] R.C. Hendricks, M.M. Athavale, and M.J. Braun. Virtual and experimental visualization of flows in packed beds of spheres simulating porous media flow. *NASA*, TM-207926, 1998.

[40] A.G. Dixon, M.E Taskin, and M. Nijemeisland. 3d CFD simulations of steam reforming with resolved intraparticle reaction and gradients. *Chemical Engineering Science*, 62:4963–4966, 2007.

[41] A. Guardo, M. Coussirat, and X. Escaler. CFD study on particle-to-fluid heat transfer in fixed bed reactors: Convective heat transfer at low and high pressure. *Chemical Engineering Science*, 61:4341–4353, 2006.

[42] D. Salari, A. Niaei, and S.R. Nabavi. CFD flow and heat transfer simulation for empty and packed fixed bed reactor in catalytic cracking of naphtha. In *Proceedings of World Academy of Science, Engineering and Technology*, pages 67–70, Waset, 2007.

[43] C.O. Castillo-Araiza, H. Jimenez-Islas, and F. Lopez-Isunza. Heat transfer studies in packed-bed catalytic reactors of low tube/particle diameter ratio. *Ind. Eng. Chem. Res.*, 46:7426–7435, 2007.

[44] A.R. Balakrishnan and D.T. Pei. Heat transfer in gas-solid packed bed system. *Ind. Tng. Chem. Process Des. Dev.*, 1:40–46, 1979.

[45] A. Liu, S. Liu, and Z. Pan. Numerical simulation of heat transfer in a gas solid crossflow moving packed bed heat exchanger. *J. of Thermal Sciencee*, 10:No.3, 2007.

[46] R. Yusuf, Melaaen M.C., and Mathiesen V. CFD modeling of heat transfer in gas fluidized beds. In *Fourth International Conference on CFD in the Oil and Gas, Metallurgical & Process Industries*, Jamshedpur, India, 2005.

[47] M. Casey and T. Wintergerste. *Best Practice Guidelines*. ERCOFRAC, 1 edition, 2000.

[48] J. Blazek. *Computational Fluid Dynamics: Principles and Applications*. ELSEVIER, 2 edition, 2005.

[49] P.J. Roache. *Verification and Validation in Computational Science and Engineering*. Hermosa Publisher, Albuquerque, New Mexico, 1998.

[50] P.J. Roache. Perspective: A method for uniform reporting of grid refinement studies. *Journal of Fluid Engineering*, 116:405–413, 1994.

[51] P.J. Roache. Quantification of uncertainty in computational fluid dynamics. *Annu. Rev. Fluid Mech.*, 29:123–160, 1997.

[52] S. Ergun. Fluid flow through packed columns. *Chem. Eng. Prog.*, 48:89–94, 1952.

[53] M. Brauer. *Grundlagen der Einphasen-und Mehrphasenstroemungen*. Sauerlaender Verlag, Frankfurt, 1 edition, 1971.

[54] B. Jones. *Viscous Grid Spacing Calculator*. Geolab, NASA, 1997.

[55] V.Y. Cengel. *Heat Transfer: A Practical Approach*. McGraw Hill Professional, 2 edition, 2003.

[56] S.Y. Yoo, H.K. Kwon, and J.H Kim. A study on heat transfer characteristics for staggered tube banks in cross-flow. *Journal of Mechanical Science and Technology*, 21:505–512, 2007.

[57] S. Natarajan, C. Zhang, and C. Briens. A parametric study of the oxygen elimination process in a packed bed. *International Journal of Reactor Engineering*, 2:Article A17, 2004.

[58] N. Wakao and S. Kaguel. *Heat and Mass Transfer in Packed Beds*. Gordon and Breach, 1 edition, 1982.

[59] V.V. Chukin and R.F. Kuznetsov. Gas distribution in a packed bed. *Journal of Engineering Physics*, 13(1):74–78, 1967.

[60] F.B. Tehrani, A. Shahmir, and A.H. Kashani. Numerical analysis of a single row of coolant jets injected into a heated crossflow. *Journal of Computational and Applied Mathematics*, 168:53–63, 2004.

[61] M.T. Kandakure, V.C. Patkar, A.W. Patwardhan, and J.A. Patwardhan. Mixing with jets in cross-flow. *Ind. Eng. Chem. Res.*, 48(0):6820–6829, 2009.

[62] A. Nirmolo, H. Woche, and E. Specht. Mixing of jets in cross flow after double rows of radial injections. *Chemical Engineering and Technology*, 31(2):294–300, 2008.

[63] A. Corey. *Mechanics of Immiscible Fluids in Porous Media*. Water Resources Publications, 3 edition, 1994.

[64] D.A. Nield and A. Bejan. *Convection in Porous Media*. Springer, 3 edition, 2005.

List of Publications

1. **Zhiguo Xu**, Hermann Woche, Eckehard Specht, "CFD Flow Simulation of Structured Packed Bed Reactors with Jet Injections", Proceedings of the Conference on Modeling Fluid Flow 2009: 536 544.

2. **Z. Xu**, H. Woche, E. Specht, "Development of a Scalable Geometric Model for CFD Flow Simulation of Shaft Kilns", Proceedings of the 7th Word Conference on Experimental Heat Transfer, Fluid Mechanics and Thermodynamics 2009: 655 662.

Curriculum Vitae

Personal data

Name:	Zhiguo Xu
Date of Birth:	04.Feb.1978
Place of Birth:	Shandong, China
Marital status:	Committed
Nationality:	China

School Education

1985–1990	Primary School, Xiduan Primary School, Heze
1990–1993	Middle School, Heze No. 8 Middle School, Heze
1993–1996	High School, Heze No. 2 High School, Heze

University Education

1996–2000	Bachelor in Chemical Engineering and Technology, East China University of Science and Technology, Shanghai
2000–2003	M.Sc. in Chemical Engineering, East China University of Science and Technology, Shanghai
2007–2010	Ph.D. in Fluid Mechanics and Thermodynamics Otto von Guericke University, Magdeburg

Professional Occupation

2003–2005	Process Engineer Shanghai Institute of Organic Chemistry, Chinese Academy of Sciences, Shanghai
2005–2007	Supervisor of Engineering Dept. Anji Microelectronics (Shanghai) Co. Ltd.

Awards

1997	"Hanmei" Scholarship
1998–1999	Third-class Scholarship
1999-2000	Second-class Scholarship
2000	Excellent Undergraduate′s Thesis
2002	"BASF" Scholarship
2003	Excellent Thesis, Outstanding graduate of Shanghai